Recent advances of metal phosphates-based electrodes for high-performance metal ion batteries

Qihui Cheng [a], Xun Zhao [a], Guiyuan Yang [a], Lei Mao [a], Fangfang Liao [a], Lingyun Chen [a,*], Pingge He [b], Dingjie Pan [b], Shaowei Chen [b,*]

[a] School of Chemistry and Chemical Engineering, Chongqing University, Chongqing 400044, China
[b] Department of Chemistry and Biochemistry, University of California, Santa Cruz, 1156 High Street, CA 95060, United States

ARTICLE INFO

ABSTRACT

Metal phosphates, such as $LiFePO_4$ (LFP), have been attracting extensive attention as electrode materials for next-generation rechargeable metal-ion batteries (MIBs), due to their high theoretical capacity, good chemical stability, long lifespan, and natural abundance. In this review, the recent progress of the design and engineering of metal phosphate-based electrode materials for MIBs is summarized. Specifically, the survey will focus on three types of phosphates, monometallic phosphates, bimetallic phosphates, and multi-metal phosphates, within the context of their intrinsic structure and corresponding electrochemical performance. A range of experimental variables will be carefully analyzed, such as sample synthesis, crystal structure, and electrochemical reaction mechanism, in conjunction with theoretical calculations. The applications of these materials as MIB electrodes are then featured for diverse MIBs, such as lithium-ion battery, sodium-ion batteries, potassium-ion batteries, calcium-ion batteries, and magnesium-ion batteries. We conclude the review with a perspective where the promises and challenges of phosphate-based electrodes for MIBs are highlighted, along with future research directions.

1. Introduction

There is an urgent need of effective technologies for the generation of renewable and clean energy, due to the rapid depletion of non-renewable energy resources and rampant emergence of environmental issues [1–3]. Development of advanced energy storage technologies with both high power and high energy density represents a critical part of this drive [4,5]. Among these, rechargeable metal-ion batteries (MIBs) are considered as the most effective solution to the increasing need for high-energy electrochemical power sources, and have become an ideal power source for electric vehicles and portable electronic devices [6,7]. Since 1991 when lithium-ion batteries (LIBs) were commercialized by Sony [8], LIBs have become a common power source in today's electronic market. Nevertheless, LIBs may not meet all the performance, cost and diversiform energy storage goals required, in particular, in large-scale applications such as electrified transportation and power grids [9]. The demands for a further reduced cost and increased energy density, as well as the growing concern about lithium consumption have accelerated the development of other "alternatives", such as sodium-ion batteries (SIBs), potassium-ion batteries (KIBs), magnesium-ion batteries, and calcium-ion batteries (CIBs).

As rechargeable LIBs have become a mainstay of the digital age, many studies have aimed to optimize and innovate this technology. It has been found that electrode materials play a most direct and fundamental role in dictating the battery performance, such as energy and power densities, lifespan and safety (Fig. 1a) [10]. To obtain high-performance LIBs, electrode materials with suitable chemical properties (*i.e.*, crystallinity composition and stability) and physical structures (*i.e.*, surface area, porosity, and pore size) are therefore inevitably required that can enable reversible faradic reactions and efficient mass transfer during charging/discharging [10,11]. Within this context, low-cost, earth-abundant, and environmentally friendly materials are of particular interest. Before 1900s, transition metal oxides occupied the main market of electrode materials of LIBs, including two-dimensional (2D) layered oxides like $Li_{1-x}MO_2$ (M = Co, Ni, Fe, and Mn) and three-dimensional (3D) spinel oxides like $LiMn_2O_4$ [12,13]. These two classes of materials exhibit close-packed oxygen stacking showing a bidimensional and tridimensional crystal structure, respectively, from which lithium ions can be easily intercalated or extracted in a reversible manner. However, when the number (x) of extracted lithium is high (end of charge), irreversible migration of transition metals within the lithium layers may occur and lead to important capacity loss on cycling [6,14]. In 1997, $LiFePO_4$ (LFP) in the olivine structure was demonstrated as a viable cathode material, with a capacity approaching 170 Ah kg^{-1}, which was higher than that of $LiCoO_2$ and comparable to that of stabilized $LiNiO_2$ [6,7]. Since then, phosphates, especially MPO_4- and $LiMPO_4$-based transition metal phosphates have been attracting a great deal of
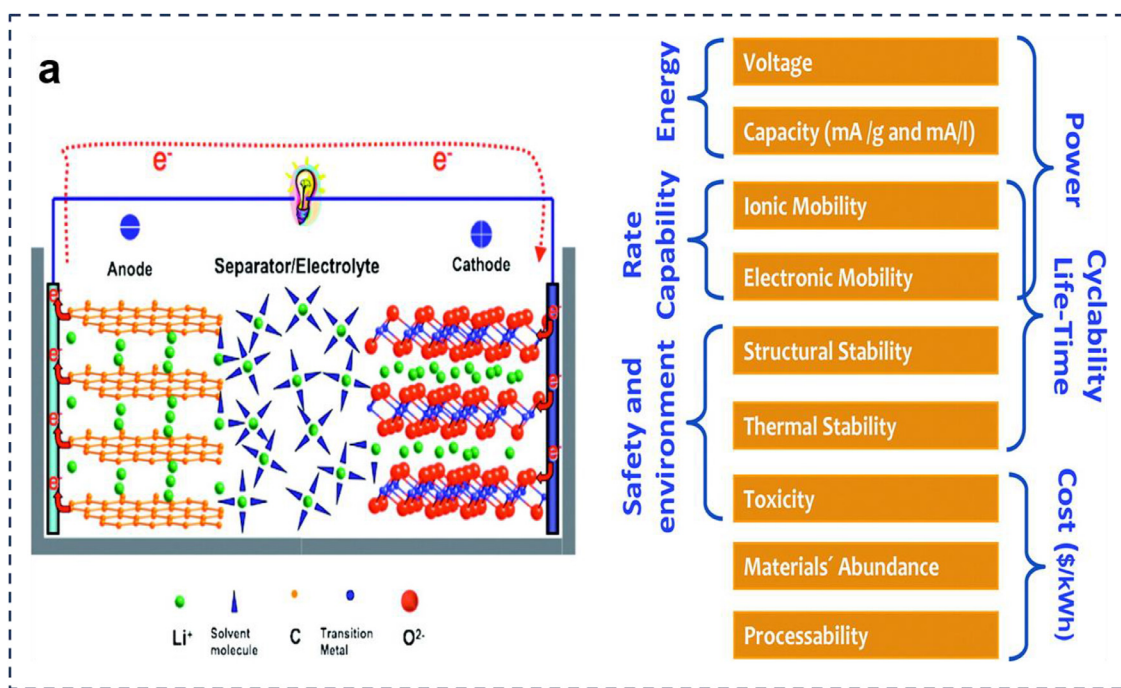
Fig. 1. (a) Schematics of a lithium ion electrochemical cell and the relevant parameters of Li battery electrode materials in relation to battery characteristics. (a) Reproduced with permission [10]. Copyright 2013, American Chemical Society.

interest [15,16]. Fig. 2a depicts some key developments of phosphate materials.

Metal phosphates possess the advantages of high natural abundance, environmental friendliness, low cost, high safety, and low toxicity [17,18]. Open-framework structures with large channels and interstitial space endow them with good ion conductivity, facile ion and electrolyte mass transport, ready access to active sites for ion intercalation, and good charge storage capacity. In addition, strong P-O covalent bonds afford high structural stability and can stabilize the lattice oxygen even at high charged state, thus ensuring long-term cycling and safety in batteries [19,20]. For instance, Hautier et al. [7] computed oxygen chemical potential for oxides and phosphates, and results showed that most of the phosphates do actually have a similar thermodynamic thermal stability than oxides, which showed the inherently safety of phosphate. Despite a low theoretical gravimetric capacity and poor intrinsic electrical conductivity, phosphates generally exhibit long-term structural stability, versatile atomic arrangements and crystal structures, and structural elasticity for accommodation of local compositional changes, which all contribute to a good energy storage performance as electrode materials [14,21]. Moreover, the phosphate group (PO_4^{3-}) can be bonded with a large number of cations to assemble polyanionic compounds with an improved lithium intercalation voltage that directly influences the specific energy and energy density, in comparison to that in the oxide form [7,10,22]. The higher voltage for the $M^{(n-1)+}/M^{n+}$ couple (compared to that in metal oxide) which results from the inductive effect of the M-O-P linkage where electronegative phosphorus ion attracts electrons from oxygen, leading to a weakened metal to oxygen bond, makes them also promising for the protection of cathode materials in (LIBs) [23,24]. However, this effect can be detrimental for certain couples, where the voltage may be too high to be accessible with the current electrolytes [25–27]. For the one-electron delithiation process, low-valence redox couples will result in a high capacity when redox active element and (poly) anion (PO_4^{3-}) are all the same. As the average voltage for a redox couple increases with the oxidation state (e.g., the average voltage for Co^{3+}/Co^{4+} is higher than for Co^{2+}/Co^{3+}) [7], the electrochemical performance of a target phosphate can be manipulated by tuning the bonding cations.

Notably, transition metal oxides/hydroxides and conducting polymers have been used extensively for the fabrication of hybrid electrode materials due to improved intrinsic electrical conductivity [28–31]. Phosphates, such as NASICON phosphates [32,33] and fluorophosphates [34], have also been extensively investigated as high-voltage cathodes for sodium-ion batteries (SIBs) [19,35] and potassium-ion batteries (KIBs) [9,36] owing to the high natural abundance of Na and K (Na, 2.36 wt.% in earth and K, 2.09 wt.%), low cost, and identical "rocking chair" operating principles [37].

In this review, we will first introduce the representative crystal structures of phosphates (i.e., Olivine $AMPO_4$, NASICON-type $A_xMM'(PO_4)_3$, and oxy- and fluoro-phosphates) and their electrochemical reaction mechanisms. We will then discuss the various preparation protocols, including hydrothermal/solvothermal, chemical precipitation, and ball milling methods, and the applications of phosphates as LIB electrode materials, with a focus on the relationship between their structures and electrochemical performance. The discussion will then be extended to other MIBs, such as SIBs, KIBs, magnesium-ion battery, and calcium-ion batteries (CIBs), in terms of the intrinsic structure of the phosphate electrode materials and electrochemical performance, as evaluated by advanced characterization technologies and theoretical calculation methods. We conclude the review with a perspective highlighting the critical challenges and possible future research directions.

2. Crystal structures and electrochemical reactions of polyanionic phosphates

Despite the low electrical conductivity and small theoretical gravimetric capacity, polyanions, such as PO_4^{3-}, SiO_4^{4-}, and SO_4^{2-}, exhibit unique features such as stable open-framework, tunable redox couple $M^{n+}/M^{(n-1)+}$, versatile atomic arrangements, and crystal structures. Thus, metal phosphates have been used rather extensively as battery electrode materials studied [32]. In this review, polyanion phosphates are mainly classified into three categories, olivine $AMPO_4$, NASICON $A_xM_2(PO_4)_3$, and tavorite $AM(PO_4)Y$ (Fig. 3a), which have been the focus of a substantial amount of research, e.g., olivine-type LFP, amorphous or crystalline $FePO_4$, NASICON $Na_2VTi(PO_4)_3$ [32,38] and $Na_3MnZr(PO_4)_3$ [39].

Discovery of NASICON structure	**1976** / **1980** — NASICON structure as hosts for reversible insertion/extraction of alkali cations (electrodes)
First preparation of B-Na₂TiM(PO₄)₃ by Perret	**1988** / **1992** — Firstly reported the existence of mixed-valence NASICON structures
FePO₄/Olivine LiFePO₄ being demonstrated as cathode for LIBs	**1997** / **1999** — Carbon coating at the surface of triphylite LiFePO₄ for full electrochemical utilization
Olivine LiCoPO₄ as 4.8 V electrode material for LIBs	**2000**
LiNiPO₄/LiMnPO₄ as cathodic materials in rechargeable LIB	**2001** — LiFeₓCo₁₋ₓPO₄ solid solutions as cathode materials for LIBs
LiFePO₄-type electrodes were firstly commercialized	**2002** — FePO₄ possibly being adopted as anode material for LIBs
First report of a NASICON framework hosting five alkali cations	Supervalent cations doping in LiFePO₄ for enhanced electrical conductivity
FLUORO-phosphates as electrode materials for LIBs/SIBs	**2003** — First report of Li⁺ extraction from Li₃V₂(PO₄)₃
AVPO₄F materials being firstly proposed as positive electrodes	**2005** — Li₂CoPO₄F as high voltage positive electrode materials / **2009**
Vanadium phosphates as cathode materials for mg-ion batteries	**2011** / **2015** — A detailed evaluation based on high-throughput ab initio calculations for phosphates as LIBs cathodes
	2016 — First report of NaVPO₄F for KIBs
First report of the charge/discharge behaviors of vanadium phosphate electrodes in 4 V-class K cells	**2017** — Sodium-iron-phosphate-fluoride for CIBs
	2018 — 3D-printed LiFePO₄ microelectrodes for full microbatteries
Ultrathick (108 mg cm⁻²) fire-resistant LiFePO₄ with ultrahigh-capacity and thermal stability (structural integrity up to 1000 °C/electrochemical activity up to 750 °C) for LIBs	**2019** — NaVPO₄F used as cathode for aqueous SIBs
	2020 — LFP used for lithium ion micro-batteries with extraordinary flexibility and high-temperature performance

Fig. 2. Timeline depicting some key developments of phosphate materials.

2.1. Olivine AMPO₄ (M = Fe, Mn, Co, and Ni)

The olivine structure, of the general formula of $AMPO_4$, is built on a distorted hexagonal close-packed (hcp) array of oxygen atoms of PO_4 tetrahedra sharing one edge and all vertices with MO_6 octahedra. They can be described as a *Pnma* space group with A or M atoms in half of the octahedral sites and P atoms in one-eighth of the tetrahedral sites [12]. Alkali metals occupy the M(1) site, forming linear chains of edge-shared octahedra running parallel to the *c*-axis in the alternate *a-c* planes. Transition metals occupy the M(2) sites, forming zigzag planes of corner-shared octahedra running parallel to the *c*-axis in the other *a-c* planes [12,40]. Taking LFP as an example, the structure can be described as a distorted hcp oxygen sub-array, in which Li, Fe and P atoms occupy interstitial sites to form (i) corner-sharing FeO_6 octahedra that are nearly coplanar to form a distorted 2D square lattice perpendicular to the *a* axis, and electronic delocalization is hence difficult; (ii) edge-sharing LiO_6 octahedra aligned in parallel chains along the *b* axis; and (iii) tetrahedral PO_4 groups connecting neighboring planes or arrays. Fig. 3b shows possible Li diffusion pathways in LFP along the [010] direction through face-shared vacant tetrahedral sites, and along the [001] direction through face-shared octahedral sites. Note that Li diffusion proceeds mostly along [010]ₚₙₘₐ [14]. Morgan et al. carried out *ab initio* studies by using the nudged elastic band method and found that although Li⁺ mobility is high in the tunnels along the [010] direction,

Li⁺ hopping between tunnels is very unlikely [41]. The unit-cell adopts an orthorhombic symmetry described either in the *Pmnb* or *Pnma* (equivalent) space groups (a = 10.338(1) Å, b = 6.011(1) Å, c = 4.695(1) Å in *Pnma* description). The peculiar distribution of Li⁺ and Fe²⁺ within the octahedral sites generates layers that have a direct impact on both electronic and ionic conductivities [14].

2.2. NASICON-type AₓMM'(PO₄)₃ (M = V and Ti, 1 ≤ x ≤ 3)

NASICON-type phosphates exhibit a 3D framework where MO_6 octahedra and PO_4 tetrahedra sharing their corners and vice versa with each other and commonly described with rhombohedral ($R\bar{3}$ for instance) or monoclinic ($C2/c$ for instance) space groups (Fig. 3c) [14]. Generally, compounds in rhombohedral phase show less thermal stability than the counterparts in the monoclinic phase. The repeating unit $MM'(XO_4)_3$ in NASICON usually is called "lantern" where three tetrahedra ([PO_4]) are connected with two octahedra ([MO_6]/[$M'O_6$]). Each lantern is connected to six other lanterns, for which a large interstitial space is generated. These lantern units are stacked parallel to the [001] direction of the hexagonal unit cell [32]. In this 3D interconnected space of $Na_2VTi(PO_4)_3$, there are two types of interstitial positions, M(1) and M(2), where Na ions are distributed (Fig. 3d) [19]. Taking $Na_2VTi(PO_4)_3$ as an example, it has a 3D framework of VO_6 octahedra sharing all of its corners with PO_4 tetrahedra and one Na⁺
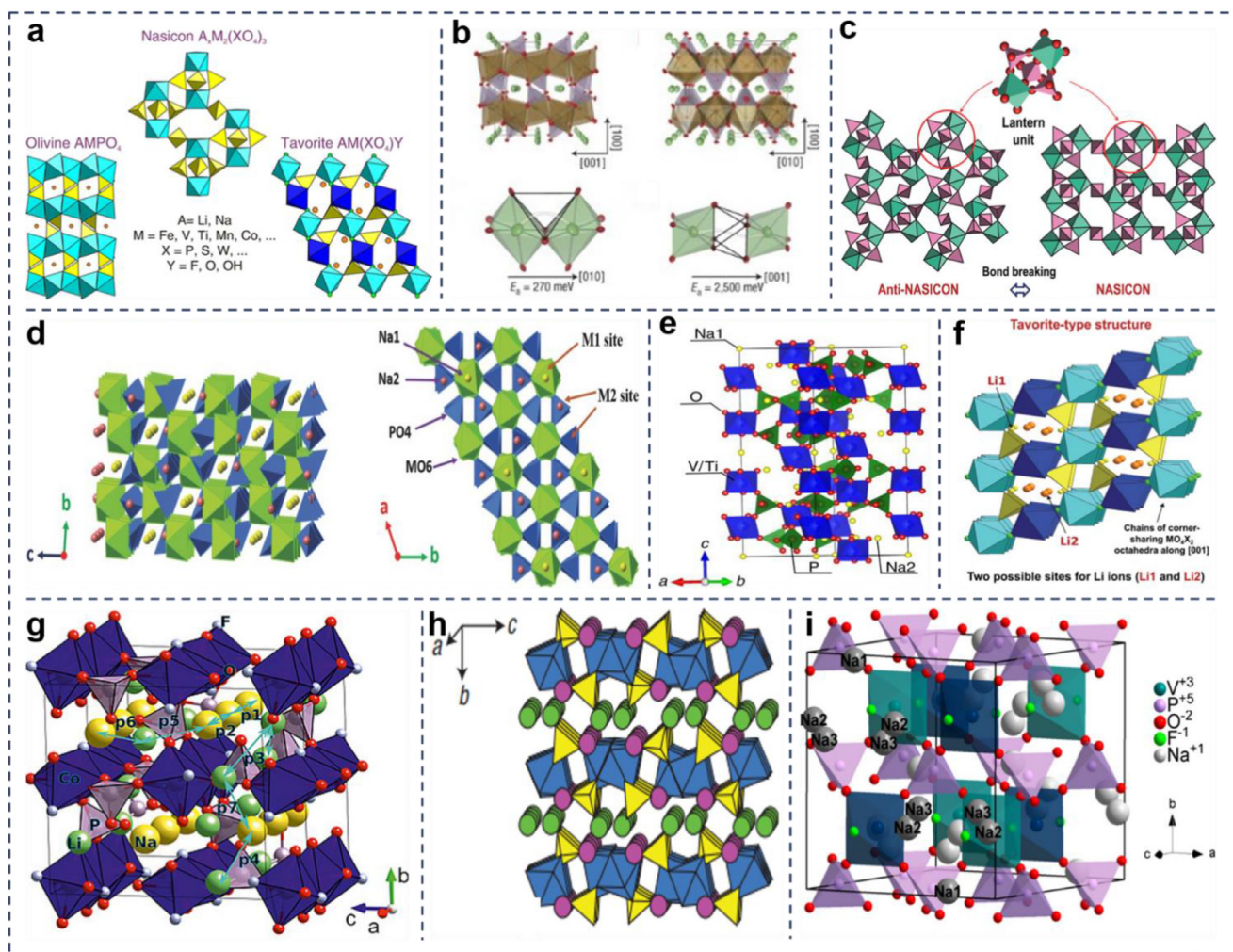
Fig. 3. (a) Crystal structure of olivine AMPO$_4$, NASICON A$_x$M$_2$(PO$_4$)$_3$ and tavorite AM(PO$_4$)Y. (a, c, and f) Reproduced with permission [14]. Copyright 2013, American Chemical Society. (b) Crystal structure of LiFePO$_4$ and possible lithium pathways. (b) Reproduced with permission [123]. Copyright 2008, Springer Nature. (c) NASICON (generally rhombohedral) and anti-NASICON (generally monoclinic) frameworks of general formula AxMM′(XO$_4$)$_3$. (d) A view of the Na$_x$M$_2$(PO$_4$)$_3$ NASICON structure along the *a* (a) and *c* (b) axis, respectively. (d) Reproduced with permission [19]. Copyright 2017, Wiley-VCH. (e) Schematic crystal structure of Na$_2$VTi(PO$_4$)$_3$, and *a-c* represent different axes. (e) Reproduced with permission [32]. Copyright 2017, Springer Nature. (f) Representation of the tavorite structural arrangement. (g) Crystal structure of A$_2$CoPO$_4$F (A = Li and Na). (g) Reproduced with permission [48]. Copyright 2019, Wiley-VCH. (h) Crystal structures of Na$_2$FePO$_4$F. (h) Reproduced with permission [49]. Copyright 2007, Springer Nature. (i) Crystal structures of Na$_3$V$_2$(PO$_4$)$_2$F$_3$. (i) Reproduced with permission [52]. Copyright 2020, American Chemical Society.

occupies the M(1) sites with sixfold coordination and the other two Na$^+$ occupy the M(2) sites forming eight-fold coordination. Only Na ions residing at M(2) sites can be extracted for electrochemical reaction due to the weak bonding to surrounding oxygen atoms (Fig. 3e), producing a theoretical capacity of 117 mA h g^{-1}.

2.3. Oxy-and fluoro-phosphates A$_x$M(PO$_4$)Y (Y = F, O, OH)

For fluoro-phosphates, four structural families of lithium transition-metal fluoro-phosphates have been reported before, AMPO$_4$F, A$_3$M$_2$(PO$_4$)$_2$F$_3$, A$_2$MPO$_4$F and A$_5$M(PO$_4$)$_2$F$_2$. The crystal structure is built on (i) PO$_4$ tetrahedra, (ii) MO$_n$Y$_y$ (M = Fe, V, Nb, Ti, Co, and Mn; Y = O, F, and OH) octahedra (sometimes very distorted) generating a 3-D framework, and (iii) A$^+$ cations located in the interstitial space (A$^+$ = Li$^+$, Na$^+$, and H$^+$) [14]. Among these four types of fluoro-phosphates, AMPO$_4$F owns a tavorite-type structure (*e.g.*, LiVPO$_4$F [42] and LiFePO$_4$F [43]). AMPO$_4$F consists of corner-sharing one-dimensional (1D) chains of MO$_4$F$_2$ octahedra, and two octahedra being bridged by fluorine atoms along the chains. These chains are interconnected by corner-sharing PO$_4$ tetrahedra, and the resulting 3D

framework delimitate different types of tunnels with two possible crystallographic sites for lithium ions (Fig. 3f) [14]. Hydroxyl-containing AMPO$_4$F analogues show similar structures (*e.g.*, LFP(OH) [44]).

For A$_2$MPO$_4$F, three structures are adopted that differ in the connectivity of the MO$_4$F$_2$ octahedra and can be specifically described as follows: (i) corner-sharing MnO$_4$F$_2$ octahedra, like Na$_2$MnPO$_4$F, which adopt a monoclinic unit cell (P2/n space group), where two types of Mn$_2$O$_8$F$_2$ chains run along the *b* axis, the corner-sharing MnO$_4$F$_2$ octahedra are connected by fluorine atoms, and these chains are connected by PO$_4$ tetrahedra, thus forming a 3D framework with the Na$^+$ cations located in the channels [45]; (ii) edge-sharing NiO$_4$F$_2$ octahedra, like Li$_2$NiPO$_4$F [46] and Li$_2$CoPO$_4$F [47,48], which also own a 3D framework built by infinite chains of edge-sharing NiO$_4$F$_2$ octahedra linked by sharing corners with isolated PO$_4$ tetrahedra (Fig. 3g), with lithium ions sitting in channels along the [010] direction; and (iii) two face-sharing MO$_4$F$_2$ octahedra, like Na$_2$CoPO$_4$F [49,50], which exhibit a layered framework and adopt an orthorhombic space group *Pbcn* (Fig. 3h). Infinite chains of M$_2$O$_7$F$_2$ units, built by two face-sharing MO$_4$F$_2$ octahedra and connected via bridging fluorine atoms, are interconnected

through PO_4 tetrahedra forming layers between which sodium cations are located.

$A_3M_2(PO_4)_2F_3$ possesses a 3D framework structure, as exemplified with $[V_2O_8F_3]$ bioctahedra where two vanadium octahedra are bridged by fluorine atoms and $[PO_4]$ tetrahedral units through which the oxygen atoms are all interconnected. This arrangement leads to the formation of channels along the a and b directions with the sodium located in the larger tunnel sites (Fig. 3i) [51–53]. By contrast, $A_5M(PO_4)_2F_2$ shows a 2D structure, with sheets made of VO_4F_2 octahedra and PO_4 tetrahedra [14].

Oxy-phosphates $VOPO_4$ exhibit two structures, α-$VOPO_4$ and β-$VOPO_4$. The former is tetragonal, space group $P4/n$, and is built of $[VO_5]\infty$ chains of VO_6 octahedra sharing corners along the quaternary axis [001] [13,54]. The four remaining oxygen corners of the VO_6 octahedra each belong to a different XO_4 tetrahedron. The latter is orthorhombic ($Pnma$ space group) into which the VO_6 octahedra are strongly distorted, forming chains along.
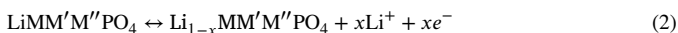
2.4. Electrochemical reactions of polyanionic phosphates

Phosphates are mainly used as the cathode materials of batteries [7,14], and few (mostly monometallic phosphates) have been studied as anode materials, such as tin phosphate [55], vanadium phosphate (VPO_4) [56], and lithium phosphate Li_3PO_4 [57]. For bimetallic olivine phosphates ($AMPO_4$), the reversible electrochemical redox reactions occurring in the battery system are about the same, as summarized below,

$$AMPO_4 \leftrightarrow A_{1-x}MPO_4 + xA^+ + xe^- (0 \leq x \leq 1) \tag{1}$$
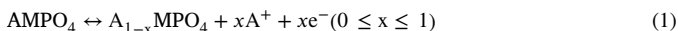
As shown in Fig. 4a [58], during the charging process, phosphate delithiates partly to form $Li_{1-x}FePO_4$ with lithium ions intercalating into the anode from the electrolyte, while in the discharging process, lithium ions deintercalate from the anode and intercalate into the cathode Li_xFePO_4. It has been found that lithium extraction from LFP results in phase separation with $FePO_4$ that limits the power characteristics. In order to improve the electrochemical performance, various strategies have been reported to suppress the phase transformation, such as using a solid solution [59], increasing the interfacial resistance at the active surface [37], and adjusting overpotential and particle size [60].
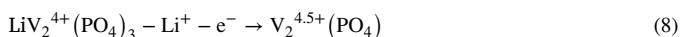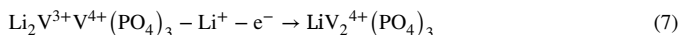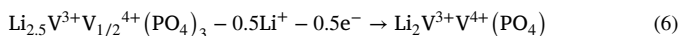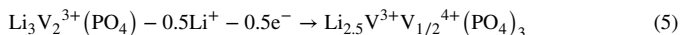
For multi-metal phosphates, like $LiMM'PO_4$, their electrochemical behaviors are accompanied by the two redox couples of different metals, exhibiting two pairs of redox peaks in cyclic voltammograms (CV) and two voltage plateaus in galvanostatic charge–discharge (GCD) plots [61,62]. (Fig. 4b-c). Similarly, with an increase of the active metal elements ($LiMM'PO_4 \rightarrow LiMM'M''PO_4$), redox couples as well as the number of corresponding redox peaks and voltage plateaus also increase [63](Fig. 4d-e). Similar to bimetallic phosphates ($AMPO_4$), the charging and discharging processes are accompanied by the insertion and extraction of lithium ions between cathode and anode. The relevant electrochemical redox reactions are summarized as follows,
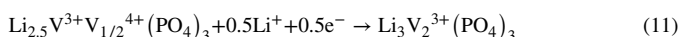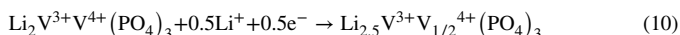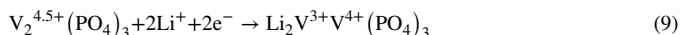
$$LiMM'M''PO_4 \leftrightarrow Li_{1-x}MM'M''PO_4 + xLi^+ + xe^- \tag{2}$$

$$Li_{1-x}MM'M''PO_4 \leftrightarrow Li_{1-x-y}MM'M''PO_4 + yLi^+ + ye^- \tag{3}$$

$$Li_{1-x-y-z}MM'M'PO_4 \leftrightarrow Li_{1-x-y-z}MM'M'PO_4 + zLi^+ + ze^- \tag{4}$$
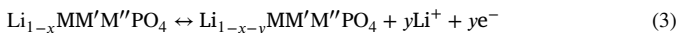
For $Li_3V_2(PO_4$ (LVP) phosphates which include rhombohedral LVP phase and monoclinic phase, their electrochemical reactions are much more complex. Rhombohedral LVP displays one voltage plateau at around 3.7 V $vs.$ Li/Li$^+$ based on the V^{3+}/V^{4+} redox couple. For monoclinic phase, under different voltage range, the number of delithiation and charging voltage plateaus fluctuate correspondingly [64,65]. As shown in Fig. 4f-g [64], within the voltage range of 3.0 to 4.8 V $vs.$ Li/Li$^+$, four voltage plateaus are observed during charging/oxidizing process at ca. 3.6, 3.7, 4.1, and 4.6 V $vs.$ Li/Li$^+$, respectively. These four

plateaus correspond to a series of phase transformation between the single phases of $Li_xV_2(PO_4)$ (x = 3.0, 2.5, 2.0, 1.0 and 0). Similarly, in the voltage range of 3.0 to 4.3 V $vs.$ Li/Li$^+$, three oxidizations at 3.6, 3.7, and 4.1 V occur in the same way, and the oxidization of vanadium at ca. 4.6 V does not happen [60]. Overall electrochemical redox reactions of LVP can be summarized as follows:

Charge:

$$Li_3V_2{}^{3+}(PO_4) - 0.5Li^+ - 0.5e^- \rightarrow Li_{2.5}V^{3+}V_{1/2}{}^{4+}(PO_4)_3 \tag{5}$$

$$Li_{2.5}V^{3+}V_{1/2}{}^{4+}(PO_4)_3 - 0.5Li^+ - 0.5e^- \rightarrow Li_2V^{3+}V^{4+}(PO_4) \tag{6}$$

$$Li_2V^{3+}V^{4+}(PO_4)_3 - Li^+ - e^- \rightarrow LiV_2{}^{4+}(PO_4)_3 \tag{7}$$

$$LiV_2{}^{4+}(PO_4)_3 - Li^+ - e^- \rightarrow V_2{}^{4.5+}(PO_4) \tag{8}$$

Discharge:

$$V_2{}^{4.5+}(PO_4)_3 + 2Li^+ + 2e^- \rightarrow Li_2V^{3+}V^{4+}(PO_4)_3 \tag{9}$$

$$Li_2V^{3+}V^{4+}(PO_4)_3 + 0.5Li^+ + 0.5e^- \rightarrow Li_{2.5}V^{3+}V_{1/2}{}^{4+}(PO_4)_3 \tag{10}$$

$$Li_{2.5}V^{3+}V_{1/2}{}^{4+}(PO_4)_3 + 0.5Li^+ + 0.5e^- \rightarrow Li_3V_2{}^{3+}(PO_4)_3 \tag{11}$$

When $Li_3V_2(PO_4)$ is charged, the first lithium is extracted at 3.6, and 3.7 V $vs.$ Li/Li$^+$ and the vanadium atoms in the crystal exist in the +3/+4 state. As the potential is increased to 4.1 V $vs.$ Li/Li$^+$, a second Li is removed via a two-phase process of $Li_2V_2(PO_4)_3 \rightarrow LiV_2(PO_4)_3$ and all the vanadium atoms in the crystal exist in the +4 oxidation state. At the voltage of 4.6 V $vs.$ Li/Li$^+$, the last lithium is extracted and part of the vanadium atoms are in the +5 state. However, the transformation of $LiV_2(PO_4)_3 \rightarrow V_2(PO_4)_3$ is kinetically difficult.

3. Synthesis methods

Phosphates can be coordinated with different cations to form monometallic, bimetallic, and multiple-metal compounds, which can be synthesized via a range of methods, such as hydrothermal/solvothermal treatment, chemical precipitation, and ball milling. The comparisons of different synthesis methods are listed in Table 1.

3.1. Chemical precipitation

Chemical precipitation is a widely used and generally well-understood synthetic method, due to the following advantages: (i) low energy consumption, where the reaction can be conducted even at room temperature; (ii) non-toxic reagents; and (iii) time-saving procedure [66]. By adjusting the reaction conditions, materials with versatile morphologies can be obtained by the precipitation method (Fig. 5a). For example, amorphous $FePO_4$ [67,68], $Ca_3(PO_4)_2$ [69], Li_3PO_4 [70], and Ni_3PO_4 [71] have been obtained through a straightforward precipitation process. Hierarchically structured nanoflakes $Co_3(PO_4)_2$ [72], micro-flowers $Co_3(PO_4)_2$ $8H_2O$ [73] and NH_4CoPO_4 H_2O [74] which show a high specific area and large nanoscale pore channels for ion transport have also been synthesized via a facile precipitate process. NASICON-type Nb^{5+} doping $NaNb_xTi_{2-x}(PO_4)_3$ was prepared by Voronina via a co-precipitation method [33] where $NbCl_5$ was added to a mixture containing $Ti(OC_2H_5)_4$ in ethanol and $NH_4H_2PO_4$ and $NaNO_3$ (molar ratio of Na:Ti:Nb:P = 1:(2–x):x:3) in water. After solvent evaporation and being dried at 120°C, the obtained powders were annealed at 900°C in air for 6 h and naturally cooled down to room temperature.

Phosphates of different morphologies and crystallographic structures can be readily synthesized by the chemical precipitation process. For instance, 1D to 3D structures can be tuned during crystallization by manipulation of electrolytic dissociation (α) of the reactants and supersaturation (S) of the solutions [69]. The relationship between morphology and
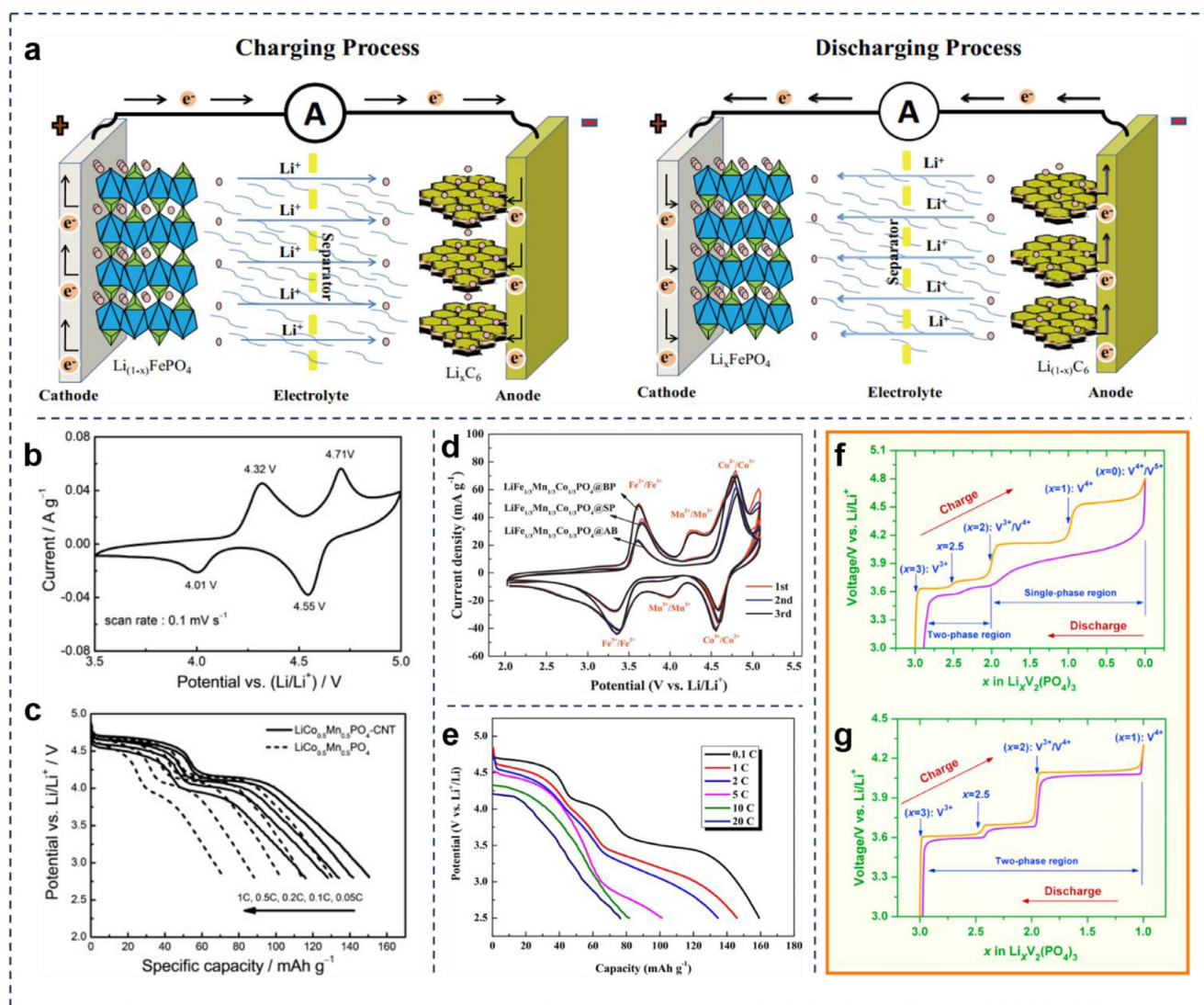
Fig. 4. (a) Charging (left) and discharging (right) processes of a typical lithium-ion battery. (b) CV profiles, and (c) rate discharge of the $LiCo_{0.5}Mn_{0.5}PO_4$-CNT and the neat $LiCo_{0.5}Mn_{0.5}PO_4$. (b, c) Reproduced with permission [61]. Copyright 2013, Elsevier. (d) CV profiles of $LiFe_{1/3}Mn_{1/3}Co_{1/3}PO_4$/AB, $LiFe_{1/3}Mn_{1/3}Co_{1/3}PO_4$/SP and $LiFe_{1/3}Mn_{1/3}Co_{1/3}PO_4$/BP at the scanning rate 0.1 mV/s in the range of 2.5-5.3 V. (e) The initial discharge curves of $LiFe_{1/3}Mn_{1/3}Co_{1/3}PO_4$/BP sample at different current rates. (d, e) Reproduced with permission [63]. Copyright 2014, Elsevier. The electrochemical voltage-composition curves of $Li_3V_2(PO_4)_3$ in the voltage ranges of 3.0-4.8 (f) and 3.0-4.3 (g) V *vs.* Li/Li+. (f, g) Reproduced with permission [64]. Copyright 2014, Elsevier.

electrolytic dissociation as well as supersaturation has been described in detail by Lai et al. [69]. Generally, anisotropic 1D or 2D materials are formed in solutions with a low α where electrolytes release reactant ions slowly, and isotropic 3D materials are formed at high α (≈ 1) with fast release of ions. For poorly dissociating reactants, the supersaturation point (S) can be controlled to have either low or high point by tuning the concentration, leading to the formation of 1D rod-like or 2D sheet-like morphologies, respectively. For highly dissociating reactants, higher S leads to fast nucleation that gives rise to the formation of irregular 3D morphologies and lower S to grow regular particles (Fig. 5b). For example, using $Bi(NO_3)_3$ and $NH_4H_2PO_4$ as precursors, the ionization equilibrium of hydrogen phosphate can be controlled by adjusting the solution pH value. Scanning electron microscopy (SEM) studies showed that particles change from an irregular coarse shape into a rod-like structure at pH = 1 to 7, and collapse into irregular aggregates at pH = 9 to 12 [75]. That is, at low pH, the ionization equilibrium of phosphoric acid leads to the formation of hydrogen phosphate, while phosphate at high pH, it tends to ionize more phosphate group. Lai et al. [69] showed that pH variation mostly induced only slight structural variations, such as crystallinity and nanoscale, but the morphologies were maintained,

especially for anisotropic materials. Moreover, in the precipitation process the mechanical driving force also influences the growth of the materials. An increased stirring speed facilitates the reaction between metal cations and reactant anions, which leads to an increased S and abundant nucleation, conducive to structural evolution and a decreased size [69]. The application of ultrasound in the reactant solution can also cause interparticle collision, which in turn induces the fusion of primary particles. This is accompanied by the oriented growth, which results in the formation of rod-shaped particles [75]. Notably, in precipitation, there is an optimum reaction time, beyond which large aggregates will form. For example, $Mn_3(PO_4)_2$ $3H_2O$/graphene nanosheets (NSs) have been prepared via the exfoliation precipitation process, whereby bulk $Mn_3(PO_4)_2$ $3H_2O$ is a prior prepared by ultrasonic-assisted precipitation [76].

3.2. Hydrothermal/solvothermal method

Hydrothermal/solvothermal chemistry is one of the principal methods for the preparation of metal phosphates [77,78], such as monometallic phosphates (*e.g.*, $Fe_5(PO_4)_4(OH)_3$ $2H_2O$ [79,80], $BiPO_4$ [57], BPO_4
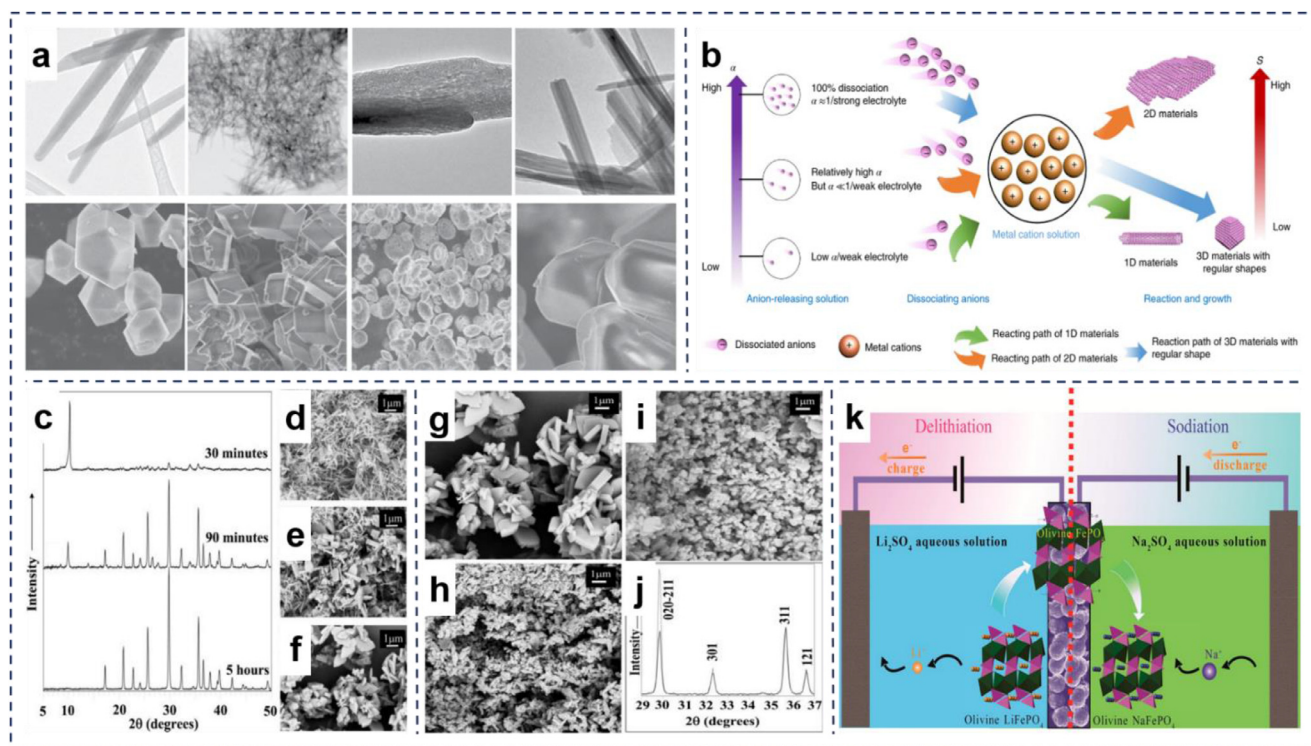
Fig. 5. (a) TEM and SEM images of various materials produced by the versatile precipitation. (b) Schematic illustrations of the formation of 1D, 2D, and 3D structures with regular shapes. (a, b) Reproduced with permission [69]. Copyright 2019, Springer Nature. (c-f) Powder XRD patterns and corresponding SEM micrographs of hydrothermal LFP after various reaction times: (d) 30 minutes, (e) 90 minutes, and (f) 5 hours. (g-j) SEM micrographs of carbon-free LFP crystallized at different concentrations and temperatures: (g) 0.25 M (Fe), 190 °C; (h) 0.75 M (Fe), 190 °C; (i) 0.25 M (Fe), 140 °C, and (j) XRD patterns of the compounds synthesized at 190 °C (0.25 M (Fe) in grey, 0.75 M (Fe) in black). (c-j) Reproduced with permission [96]. Copyright 2007, The Royal Society of Chemistry. (k) Synthetic scheme of the aqueous electrochemical displacement process from olivine LFP to isostructural NFP. (k) Reproduced with permission [110]. Copyright 2015, American Chemical Society.

[81], VPO_4 [56,82], $FePO_4$ [77]), bimetallic phosphates (*e.g.*, LFP [83,84], $Li_3V_2(PO_4)_3$ [85] $Ag_2VO_2PO_4$ [24]), and trimetallic phosphates (*e.g.*, $LiCo_{0.5}Mn_{0.5}PO_4$ [61], $Na_2Mn_{1.5}Fe_{1.5}(PO_4)_3$ [86]). The hydrothermal/solvothermal processes have also been adopted to prepare fluorophosphates [87]. When battery materials are prepared in nanoscale forms, their power density increases because of the short transport paths for ions and electrons [88]. Table 2 lists a range of phosphates that have been prepared by hydrothermal/solvothermal process, along with their corresponding morphologies.

In hydrothermal/solvothermal synthesis, distinctly different structures can be obtained by a careful manipulation of the reaction conditions. Taking LFP as an example, at excess Fe, LFP with crystallographic defects can be obtained via a simple hydrothermal route [89]. By controlling the overall concentration of the precursors and reducing agents, off-stoichiometry $Li_{1-x}Fe_{1+x}(PO_4)_{1-y}(OH)_{4y}$ has been synthesized under hydrothermal conditions [90]. Under microwave irradiations at a low power level and prolonged reaction time, pure LFP can be synthesized via a solvothermal process using ethylene glycol as the reaction medium [91]. With stoichiometric amounts of $CH_3COOLi \cdot 2H_2O$, $Fe(NO_3)_3 \cdot 6H_2O$, $NH_4H_2PO_4$, and citric acid at a molar ratio of 1:1:1:1, LFP nanoparticles have been prepared hydrothermally at 180 °C for 6 h [92]. In another study, LFP microspheres encapsulated in graphene NSs are successfully prepared hydrothermally with $FeSO_4$ and graphene oxide (GO)-Li_3PO_4 at 200 °C for 10 h [70]. Similar to the structure of microspheres, micro hollow spheres LFP has also been obtained by a solvothermal method using spherical Li_3PO_4 as the self-sacrificed template and $FeCl_2 \cdot 4H_2O$ as the Fe^{2+} source [93]. Plate-like LFP has been synthesized from the precursors of LiH_2PO_4 and $FeC_2O_4 \cdot 2H_2O$ in an ethylene glycol solution at a Li:Fe:P molar ratio of 1:1:1 via a hydrothermal treatment at 200 °C for 8 h [94]. By careful manipulation of the

temperature, reaction time and concentration of precursors during the hydrothermal process, the particle morphology and crystallite size of the resultant products can be tuned [86,95]. As shown in Fig. 5c-j, when the heating time was increased from 30 min to 5 h, the morphology of LFP gradually changed from nano-leaflets to large crystallites; and the crystallite size of LFP decreased with increasing Fe concentration and decreasing heating temperature [96].

Internal reducing agents and additives can also be added into the solution for further control and adjustment of the nanostructures. For instance, N-methyl-2-pyrrolidone (NMP) is an effective reducing agent and crystal growth inhibitor; and the addition of NMP can lead to the formation of LFP nanoparticles with a reduced size and a single-phase orthorhombic structure [97]. A reduced particle size has also been achieved with the addition of carbon black into the pre-hydrothermal solution [98].

3.3. Ball milling method

In a typical ball milling process, a mixture of selected solid precursors is placed in the mill chamber and subjected to high-energy collision from the milling media [99,100]. As a rather simple and cost-effective fabrication process, ball milling has been adopted to prepare metal phosphates. Yet, as the desired products cannot be obtained directly via only the high-energy milling process, post treatment is needed. For example, in one earlier study [101], LFP was prepared from the mixture of $LiOH \cdot H_2O$, $FePO_4 \cdot 4H_2O$, and selected organic acid by high-energy milling, followed by calcination at 700 °C for 3 h under argon. In another study [102], carbon-coated LVP/reduced graphene oxide (LVP@C/rGO) composites were synthesized from the mixture of Li_2CO_3, V_2O_5, $NH_4H_2PO_4$, and carbon sources of 5 wt.% GO and 15 wt.% sucrose by ball milling for

Table 1
Comparisons of different synthesis methods of metal phosphates.

Method	Advantages	Disadvantages
Co-precipitation	Low energy consumption, non-toxic reagents environmentally friendly, simple operation, low cost, facile synthesis, easy control of preparation conditions	High reaction rates make it difficult to control precisely the morphologies of the resulting products; difficult to control the ratio of target product; easy agglomeration
Hydrothermal	controllable morphology and nano-size, fast reaction kinetics, short processing times, phase purity, low cost	Not intuitive to the observation of reaction phenomenon; infeasible to large scale production
Ball-milling	Simple and cost-effective fabrication process Homogeneous system	Impurities and structural defects in treatment process, uneven particle size distribution
Sol-gel	Ease of uniformly doping at molecular level, fast reaction at the nanoscale diffusion layer, homogeneous mixing of reactants at the atomic or molecular level, small particle size on a nanometer scale and uniform particle distribution	Long synthesis period, contraction due to gas escaping from micropores during the drying process

two days, followed by calcination at 750°C for 10 h under a flow Ar/H_2 atmosphere. Bulk LFP has also been prepared using the same strategy. By exfoliation of bulk LFP (LFP-BL) prepared via ball-milling, ultrathin LFP NSs can be readily prepared [29].

Ball-milling processes have also been adopted to prepare multimetal phosphates. Take $LiFe_{0.3}Mn_{0.7}PO_4$ as an example. In an early study [103], Li_2CO_3, FeC_2O_4 $2H_2O$, MnC_2O_4 $2H_2O$, $NH_4H_2PO_4$, and LiF at a molar ratios of 0.5:0.3:0.7:1.02:0.1 were thoroughly mixed and ground by planetary ball milling. After a calcination treatment at 350°C for 10 h, the obtained powders were reground and pelletized. Finally, $LiFe_{0.3}Mn_{0.7}PO_4$ powders were obtained after a sintering process at 600°C for 10 h. $LiMn_{1/3}Fe_{2/3}PO_4/C$ composites were prepared similarly via ball-milled in an ethanol medium for 3 h with $MnFe_2O_4$, $NH_4H_2PO_4$, Li_2CO_3, and glucose (1:3:1.5:0.4), followed by thermal sintering at 680 °C for 5 h in an Ar atmosphere [104]. Pagot [105] prepared $LiFe_\alpha Ni_\beta Co_\gamma PO_4$ via a three-step procedure that included ball-milling, sintering and re-grinding. First, Li_2CO_3, $(NH_4)_2HPO_4$, Fe_2O_3, NiO, and $2CoCO_3$ $2Co(OH)_2$ nH_2O at different ratios were mixed in a planetary ball mill (2 h, 500 rpm). Pellets of the samples were then thermally treated in a furnace at 700°C in air for 24 h. Finally, the samples were ground again via planetary ball milling (2 h, 500 rpm).

3.4. Sol-gel method

Sol-gel synthesis usually includes mixing, aging, evaporating, and heating treatment, and favors the formation of a homogeneously dispersed phase [106,107]. It has been used to synthesize various NASICON-structured phosphates, *e.g.*, $Li_3V_2(PO_4)_3$ [108], $Na_2VTi(PO_4)_3$@C [32], $Na_3MnZr(PO_4)_3$ [39], and $Na_3V_2(PO_4)_3$ [106,109]. For instance, $Li_3V_2(PO_4)_3$ nanoparticles have been produced by high temperature sintering of gel precursors obtained via a mixing and aging process [108]. During the solution reaction step after mixing,

it is easy to achieve uniform doping at the molecular level. For example, manganese doped-$Na_3V_2(PO_4)_3$ has been synthesized via a citric-based sol-gel method using manganese (III) acetylacetonate as the doping precursor, leading to a homogeneous dispersion of the active material particles and good electrochemical performance [106].

3.5. Other methods

Other methods have also been used to synthesize metal phosphates. For $NaFePO_4$, synthesized from direct high-temperature process shows thermodynamically favored maricite phase, which has no obvious channels for fast alkali diffusion [110]. Thus, several research works have adopted electrochemical-driven ion-exchange for the preparation of olivine $NaFePO_4$ from olivine LFP precursor. Experimentally, the olivine LFP/C electrode is fully delithiated (charged) in a Li_2SO_4 aqueous solution to obtained a $FePO_4/C$. After being sodiated in a Na_2SO_4 aqueous solution, $FePO_4/C$ is transferred into the final olivine $NaFePO_4/C$ electrode (Fig. 5k) [111]. Additionally, phosphates can be synthesized by direct-growth strategies, such as atomic layer deposition (ALD), which is based on the sequential use of self-terminating gas-solid surface reactions. Because only one layer of atoms is deposited at a time, they typically require a long deposition time; yet a controlled thickness and uniform film of LFP can be obtained. For example, carbon nanotubes (CNTs) uniformly covered with LFP have been synthesized via the ALD process. The thickness of amorphous LFP is linearly dependent on the ALD cycle number [78]. Aqueous-based refluxing has also been used to prepare phosphates. For example, LFP has been produced by refluxing a mixture of precursors at a select temperature over a period of time [112]. Electrospinning is another method to prepare phosphates [113]. For example, 1D highly porous $Li_3V_2(PO_4)_3/C$ nanofibers has been fabricated by an electrospinning-assisted solid-state method from a solution containing CH_3COOLi $2H_2O$, NH_4VO_3, $NH_4H_2PO_4$, and poly(vinyl pyrrolidone) [114].
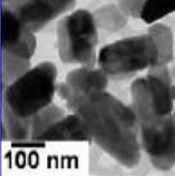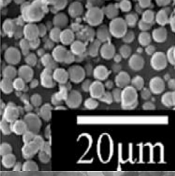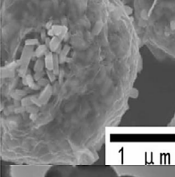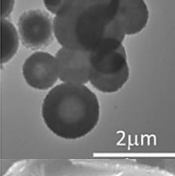
4. Li-ion batteries
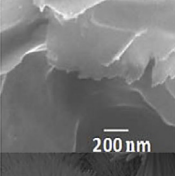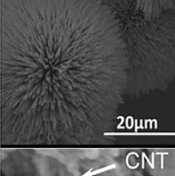
The phosphate group can react with most of the elements in the periodic table (such as transition metals like Fe, Li, Mn, Sn, V, etc.) and form diverse inorganic phosphates [66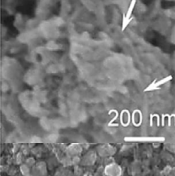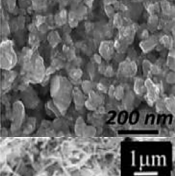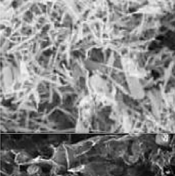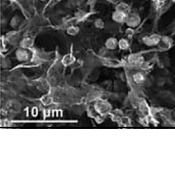], which can be used in various batteries. Based on the number of metal element, these phosphates are mainly classified into three categories: (1) monometallic phosphates, (2) bimetallic phosphates, and (3) multi-metal phosphates. In the following subsections, we will discuss the applications of these phosphates as LIB electrode materials, focusing on the structures and electrochemical performance.

4.1. Monometallic phosphates

A range of monometallic phosphates have been used for LIBs, as listed in Table 3. Among these, $FePO_4$-based phosphates have been the most commonly used materials since 1997 when Padhi and co-workers firstly reported the use of $FePO_4$ as a cathode material [115], due to their high theoretical energy-storage capacity of 178 mA h g^{-1} [7]. However, the practical application of $FePO_4$ is limited by the poor kinetics of electron and lithium ion transport, which leads to poor charge and discharge rates during prolonged cycling [68]. Experimentally the integration of a proper conducting phase, such as graphene [79], carbon, and CNT [68], into phosphates can act not only as a desired charge transfer medium but also as a buffer zone of the volume change of active materials. For instance, Han and co-workers [79] successfully synthesized graphene aerogel-supported hydroxide phosphate dihydrate ($Fe_5(PO_4)_4(OH)_3$ $2H_2O$) microspheres (GA/IHPDs, dia. 2 μm) by hydrothermal mineralization of Fe^{3+} and PO_4^{3-} ions in the presence of graphene oxide (GO) (Fig. 6a-d). The hybrid composite showed enhanced rate capability and excellent cycle stability even at an ultrahigh current density, due to the interaction between

Table 2

A summary of hydrothermal/solvothermal preparation conditions and morphologies of phosphates.

| Material	Morphology	Corresponding image	Method	Ref.
LiMPO$_4$ (M Mn, Fe, Co, and Ni)	Nano-thumb-like		Microwave irradiated solvothermal	[84]
FePO$_4$/CNT	Carbon nanotube embedded microspheres		Hydrothermal	[80]
G-LiFePO$_4$	LiFePO$_4$ microspheres wrapped by graphene nanosheets		Hydrothermal	[70]
LiFePO$_4$	Micro-hollow spheres		Solvothermal	[93]
LiFePO$_4$/C	Plate-like		Solvothermal	[94]
Na$_2$Mn$_{1.5}$Fe$_{1.5}$(PO$_4$)$_3$	Alluaudite		Hydrothermal	[86]
LiCo$_{0.5}$Mn$_{0.5}$PO$_4$-CNT	LiCo$_{0.5}$Mn$_{0.5}$PO$_4$ nanoparticles /CNT wires		Hydrothermal	[61]
N-G-Li$_3$V$_2$(PO$_4$)$_3$/C	Li$_3$V$_2$(PO$_4$)$_3$/C nanocrystals anchored on nitrogen-doped graphene nanosheets		Microwave-assisted hydrothermal	[85]
LiFePO$_4$	Nano-leaflets		Hydrothermal	[96]
GA-Fe$_5$(PO$_4$)$_4$(OH) H$_2$O	Microspheres supported by graphene aerogel		Hydrothermal	[79]

Table 3
Performances of recently reported LIBs based on monometallic phosphates with corresponding morphologies.

Materials	Morphology	Capacitance	Capacity retention [%]	Electrolytes	Voltage, V	Ref.
$Fe_5(PO_4)_4(OH)_3 \cdot 2H_2O$	Particles of the IHPDs wrapped by graphene sheets	180 mA h g^{-1} (at 50 mA g^{-1})	-	1 M LiPF$_6$ in EC-DMC	1.5–4.5 vs. Li/Li$^+$	[79]
FePO$_4$-CNT	FePO$_4$ nanoparticles embedded into CNTs.	177 mA h g^{-1} (at 0.1 C)	90@2000@5 C	1 M LiPF$_6$ in EC-DEC-DMC	2.0–4.2 vs. Li/Li$^+$	[68]
$Fe_{1.19}(PO_4)(OH)_{0.57}(H_2O)_{0.43}$-10% C	Particles dispersed in carbon black	150 mA h g^{-1} (at 0.25 C)	99@150@2 C	1 M LiPF$_6$ in EC-DEC	2.0–4.5 vs. Li/Li$^+$	[98]
VPO$_4$/rGO	Hydrangea-like microspheres	537 mA h g^{-1} (at 0.1 A g^{-1})	96@3000@2 A g^{-1}	1 M LiPF$_6$ in EC-DEC	0.01–3.0 vs. Li$^+$/Li	[56]
Li$_4$Ti$_5$O$_{12}$/TiO$_2$/Li$_3$PO$_4$	Nanoforest layer	88 μA h cm^{-2} (at 50 μA cm^{-2})	-	1 M LiPF$_6$ in EC-DEC	1.0–3.0 vs. Li$^+$/Li	[118]

Notes: a EC: ethylene carbonate; DEC: diethyl carbonate; DMC: dimethyl carbonate.
b Cycling stability is expressed as the capacity retention after some charging/discharging cycles at a specific rate.
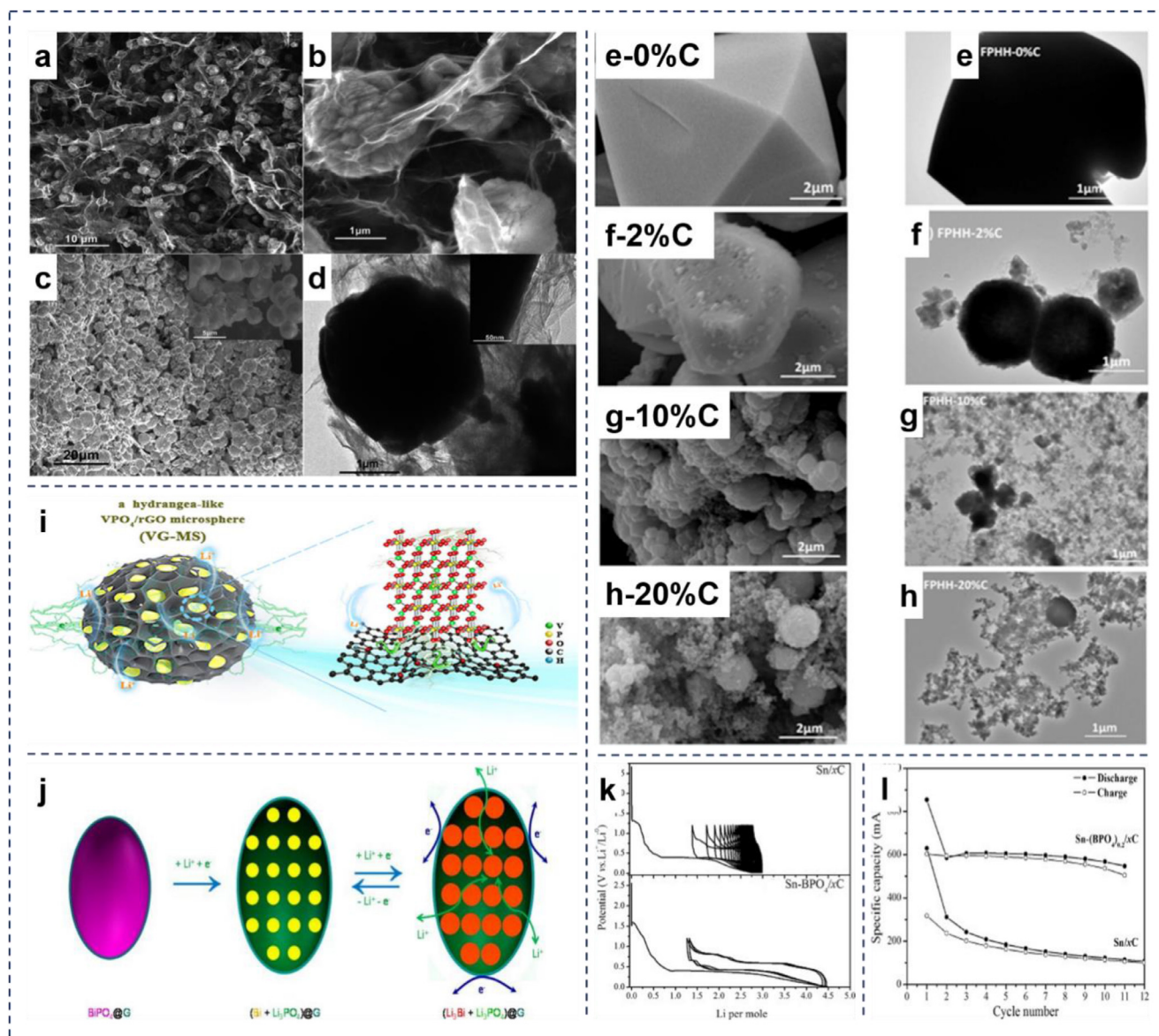
Fig. 6. (a-d) SEM and TEM images of GA/IHPDs hybrids. (a-d) Reproduced with permission [79]. Copyright 2014, The Royal Society of Chemistry. (e-h) SEM (left side) and corresponding TEM (right) micrographs of (e) FPHH-0% C, (f) FPHH-2% C, (g) FPHH-10% C, and (h) FPHH-20% C prepared by hydrothermal synthesis with carbon black added in solution. (e-h) Reproduced with permission [98]. Copyright 2017, Elsevier. (i) Illustration of high-rate and long-cycle charge storage of VG-MS architecture. (i) Reproduced with permission [56]. Copyright 2020, Elsevier. (j) Schematics illustrate Li$_3$PO$_4$ matrix enables long-cycle-life bismuth anodes. (j) Reproduced with permission [57]. Copyright 2016, American Chemical Society. (k) Galvanostatic discharge/charge curves of Sn/xC and Sn-BPO$_4$/xC against Li metal at C/5 rate, and (l) discharge/charge capacity of the Sn/xC and Sn-BPO$_4$/xC composites as function of the cycle number. (k, l) Reproduced with permission [81]. Copyright 2011, Elsevier.

IHPD and graphene aerogel as well as interconnected 3D macroporous frameworks, which not only provided a continuous pathway for the transportation of Li ion and electrons, but also reduced the damage. Similarly, Karegeya et al. [98] prepared iron hydroxyl phosphate hydrate $Fe_{1.19}(PO_4)(OH)_{0.57}(H_2O)_{0.43}$(FPHH)-based composites by a hydrothermal process in the presence of carbon black. The addition of carbon black not only effectively reduced particle size, with FPHH containing 10% C showing the highest specific surface area, but also improved electrical conductivity. As shown in Fig. 6e-h, the particle size of FPHH/carbon black was much smaller than that of FPHH alone and the conductive carbon was dispersed among the FPHH particles. In addition, Zhang et al. [68] constructed a uniformly dispersed a-FePO$_4$-CNT nanocomposite via interface interaction of surface modified a-FePO$_4$ and CNT dispersion under mild sonication. This well-dispersed structure coupled the merits of a-FePO$_4$ and CNT, which facilitated electron and ion transport. As a result, even at the current density of 5 C, the a-FePO$_4$-CNT cathode still possessed a specific capacity of 117 mA h g^{-1}; and after 2000 cycles at 5 C, nearly 90% of the initial discharge capacity was retained.

Because of the versatile framework with tunable functionalities, and the ability of being able to alleviate volume variation occurring during charge-discharge, mesoporous metal phosphates have been studied as a promising electrode material for LIBs [116]. For instance, Lee et al. [55] prepared various mesoporous tin phosphates with surfactants as templates. Compared with the non-mesoporous counterparts, the tin-phosphate anodes with 42, 82, and 100% mesopores showed a high capacity retention over 50%, reaching charge capacities of ~260, ~290, and ~325 mA h g^{-1}, respectively (after 50 cycles). Lu et al. [56] prepared 3D hydrangea-like, pseudocapacitive VPO$_4$/rGO microspheres, where VPO$_4$ microspheres were embedded in interlaced mesoporous rGO. The unique porous structure and open spaces provided abundant electron/ion transfer paths and large surface area for the contact with the electrolyte (Fig. 6i). In addition, the pseudocapacitive nature of the VPO$_4$/rGO electrode resulted in ultrafast charge storage. Thus, the self-supporting anode delivered an excellent fast-charging (537 mA h g^{-1} at 0.1 A g^{-1}) and long-life performance (318 mA h g^{-1} even after 3000 cycles at 2 A g^{-1}).

Other phosphates, such as BiPO$_4$, that are more uncommon have also been used for LIB. For example, Sun et al. [57] synthesized BiPO$_4$@G composite by a solvothermal reaction, using GO, Bi(NO$_3$)$_3$ 5H$_2$O, and NaH$_2$PO$_4$ as precursors. After an *in situ* electrochemical lithiation process, bismuth nanoparticles were homogeneously confined in the solid-state γ-Li$_3$PO$_4$ matrix producing BiPO$_4$@G (Fig. 6j), leading to a significantly improved electrochemical cycling performances, with a reversible capacity of 280 mA h g^{-1} at 100 mA g^{-1} and a capacity decay rate of merely 0.071% per cycle up to 500 cycles. Similarly, using BPO$_4$ as the matrix, Sn-based composites (Sn-BPO$_4$/xC) were obtained by carbothermal reduction of the mixtures of SnO$_2$, carbon black, and BPO$_4$. The BPO$_4$ matrix afforded an intimate dispersion of the *in situ* formed tin metal particles, which resulted in enhanced electrochemical capacity together with relatively stable cycling performances, as compared to Sn/xC without BPO$_4$ (Fig. 6k-l) [81]. Furthermore, coating amorphous Li$_3$PO$_4$ thin films on the surface of a Li metal electrode can not only suppress the growth of lithium dendrites on pure lithium metal but also improve lithium lifespan. The improved performance of the Li$_3$PO$_4$-coated Li electrode was mainly due to the high chemical stability and amorphous nature of Li$_3$PO$_4$, which led to layer-by-layer growth of the Li film rather than formation of islands and dendrites [117]. Li$_3$PO$_4$ also plays an important role in enhancing the electrical conductivity and Li$^+$ diffusion. For example, Marta et al. [118] synthesized Li$_4$Ti$_5$O$_{12}$/TiO$_2$/Li$_3$PO$_4$ composites by self-organized TiO$_2$/Li$_3$PO$_4$ nanotubes. Due to facile electron-transfer pathways, the resulting Li$_4$Ti$_5$O$_{12}$/TiO$_2$/Li$_3$PO$_4$ composites were firmly attached to the Ti current collector reaching a maximum energy density of about 260 W h kg^{-1} at C/2.

4.2. Bimetallic phosphates

Bimetallic inorganic metal phosphates (AMPO$_4$, with A denoting an alkali metal (either Li or Na) and M a transition metal) belong to a general class of 'polyanion' compounds, such as maricite AMPO$_4$, NASICON A$_3$V$_2$(PO$_4$)$_3$, olivine AMPO$_4$ [12], and tavorite A$_x$M(PO$_4$)Y. Among them, olivine and NASICON-type phosphates have been extensively studied as electrode materials for MIBs [119]. The Maricite structure is similar to the olivine one, but is generally of less interest for battery applications given that there are no obvious channels for fast alkali diffusion in these materials [12]. Inspired by the seminal work from the Goodenough group [120,121], there has been great interest in bimetallic inorganic metal phosphates as electrode materials for rechargeable LIBs, because of their high energy density, low raw materials cost, environmental friendliness, and safety [10].

4.2.1. Olivine-structured phosphates
4.2.1.1. LiFePO$_4$. Olivine phosphates (LiMPO$_4$) are well-known workhorse electrode materials for high energy density Li intercalation, where Li$^+$ are inserted into the host structure without causing significant rearrangement of the original structure [122]. Among these, olivine-LFP compounds have received most attention and found widespread applications in industry, due to their excellent electrochemical properties (high lithium intercalation voltage of ~3.5 V relative to lithium metal, high theoretical capacity of 170 mA h g^{-1}), stability, low cost, and ease of synthesis [119]. Indeed, a number of LiMPO$_4$-based materials have been synthesized. However, there are several major drawbacks of these compounds, such as their poor intrinsic electrical conductivity and 1D diffusion channels for Li$^+$ (Fig. 7a), which lead to a low electrochemical rate performance [123]. These issues may be mitigated by structural engineering (Table 4).

In these approaches, a good control over the physical and chemical properties of nanostructured LFP (such as morphology, size, and composition) is critical in achieving optimal electrochemical performance. For example, to address the issue of low electrical conductivity, Wang et al. [100] dipped an LFP electrode into a 4-[bis(4-methoxyphenyl) amino] benzylphosphonic acid (BMABP) solution, for which the resulting single molecular layer of redox-active BMABP provided the desired electron transport and permitted exchange of lithium ions to occur rapidly across the solid/electrolyte interface. As compared to conventional carbon-based conductive additives at equal loading, the rate capability was markedly enhanced.

In another study [124], Tsuda et al. successfully reported holing of LFP with an average hole diameter of 20-30 μm and hole opening rate of 1-2% by a pico-second pulsed laser. These holes greatly increased the area available in the discharge process resulting in decreased charge-transfer resistance and thus high-rate discharging performance. Anh et al. [125] prepared spherical Li$_3$Fe$_2$(PO$_4$)$_3$, and observed a capacity of 100 mA h g^{-1} at 2.5 C rate. The performance was markedly enhanced when Li$_3$Fe$_2$(PO$_4$)$_3$ particles were embedded in carbon films, at 130 and 50 mA h g^{-1} at C/2 and 16 C rates, respectively.

4.2.1.1.1. Carbon composites. Because polyanion-based materials usually exhibit lower electrical conductivity than oxides, their surface is typically modified with conducting carbon materials [28,83], as illustrated in Fig. 7b [126,127]. In an early study [128], an ultrathin and uniform carbon layer (1.9 nm) was deposited on hierarchically mesoporous LFP nano/microspheres (20-140 nm in diameter) through a liquid carbon dioxide (l-CO$_2$) based method, forming a core (LFP)-shell (carbon) structure. After calcination, this carbon coated LFP (C-LFP) allowed facile penetration of liquid electrolytes and rapid electron and Li$^+$ transport. Experimentally, the unmodified LFP showed a discharge capacity of 125 mA h g^{-1} and 98 mA h g^{-1} at current density of 0.1 and 1 C, respectively, and retained 83% of the original capacity at the end of 140 cycles. In contrast, C-LFP exhibited outstanding capacity retention with a capacity of 168 mA h g^{-1} at 0.1 C at the end of 140 cycles, virtu-
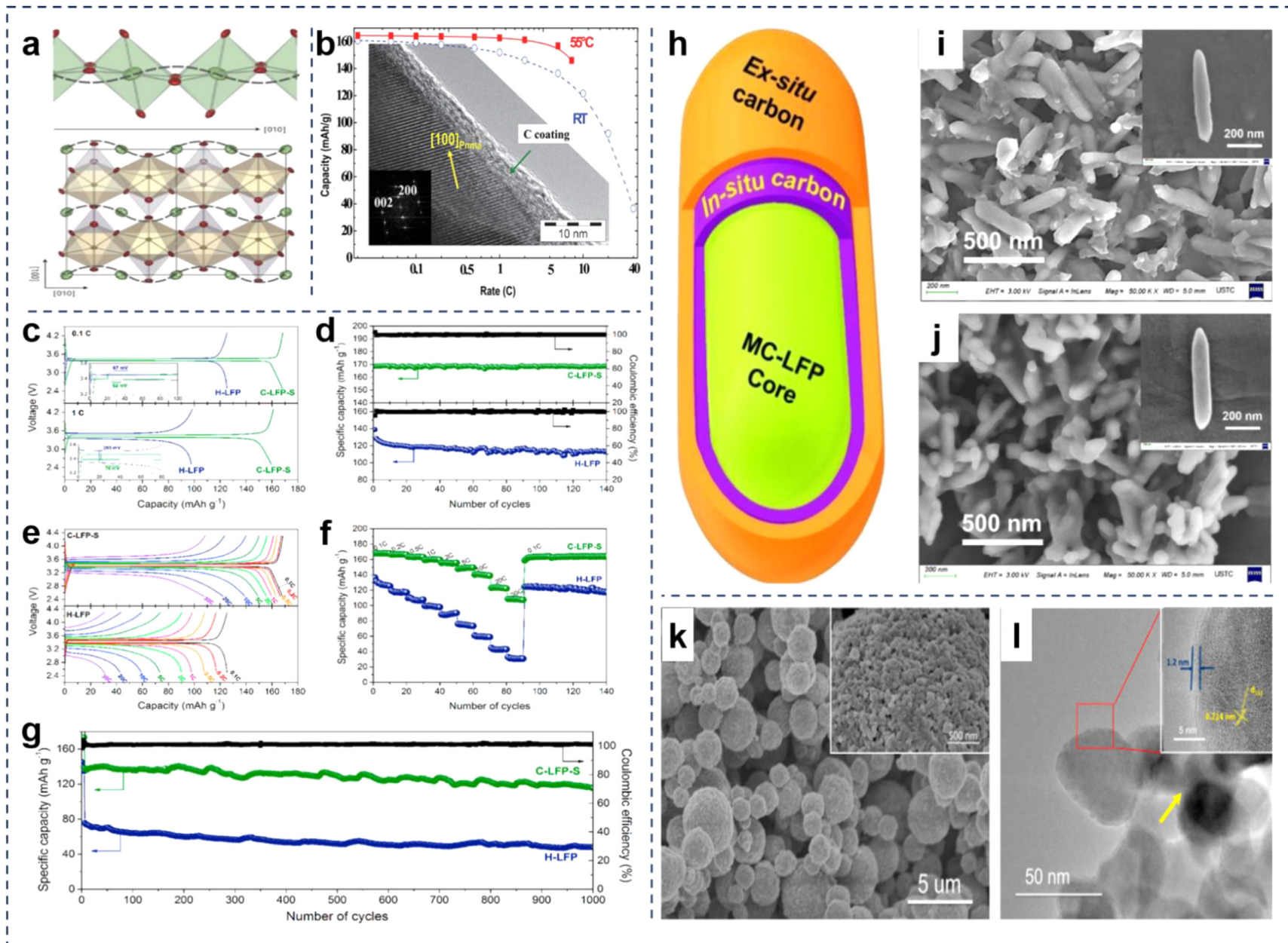
Fig. 7. (a) Anisotropic harmonic lithium vibration in LFP shown as green thermal ellipsoids and the expected diffusion path. (a) Reproduced with permission [123]. Copyright 2008, Springer Nature. (b) Thin carbon coating at the surface of highly crystalline LFP yields to high benefits for electrochemical response at high rate. (b) Reproduced with permission [14]. Copyright 2013, American Chemical Society. (c-g) Electrochemical performances of H-LFP and C-LFP-S. (c) Charge/discharge profile at 0.1 C and 1 C, (d) Cycling stability at 0.1 C, (e) Charge/discharge profile at different C rates, and (f) rate capabilities at C rates of 0.1 C (cycles 1-10), 0.2 C (11-20), 0.5 C (21-30), 1 C (31-40), 2 C (41-50), 5 C (51-60), 10 C (61-70), 20 C (71-80), 30 C (81-90), and 0.1 C (91-130), and (g) long-term cyclability at 10 C. (c-g) Reproduced with permission [128]. Copyright 2017, Elsevier. (h) Schematic illustration of MC-LFP core structure. (i) SEM micrograph of the MMC-LFP and (j) DMC-LFP after pyrolysis. (h-j) Reproduced with permission [131]. Copyright 2019, The Royal Society of Chemistry. (k) SEM and (l) HRTEM images of the LFP/C. (k-l) Reproduced with permission [133]. Copyright 2015, Elsevier.

Table 4
Performances of recently reported LIBs based on LiFePO$_4$ with corresponding morphologies.

Materials	Morphology	Capacitance	Capacity retention [%]	Electrolytes	Voltage, V	Ref.
LiFePO$_4$/C	Spherical LiFePO$_4$ particles embedded in carbon films	130 mA h g^{-1} (at C/2)	97.7@460@1 C	1 M LiPF$_6$ in EC-DMC-DEC	2.0–4.2 vs. Li/Li$^+$	[125]
LiFePO$_4$/C	Carbon-coated LiFePO$_4$ microspheres	168 mA h g^{-1} (at 0.1 C)	84@1000@10 C	1 M LiPF$_6$ in EC-DMC-EMC	2.5–4.3 vs. Li/Li$^+$	[128]
LiFePO$_4$/C	Core (LiFePO$_4$)-shell (carbon)	159 mA h g^{-1} (at 1 C)	-	1 M LiPF$_6$ in EC-DEC	2.5–4.2 vs. Li/Li$^+$	[129]
LiFePO$_4$/C	Carbon nanowire coated LiFePO$_4$ nanosheets	197 mA h g^{-1} (at 0.1 C)	91.4@100@1C	1 M LiPF$_6$ in EC-DEC-DMC	2.5–4.2 vs. Li/Li$^+$	[130]
LiFePO$_4$/C	Dually carbon coated mitochondria-like	138 mA h g^{-1} (at 10 C)	93@1000@10 C	1 M LiPF$_6$ in EC-DMC	2.0–4.3 vs. Li/Li$^+$	[131]
LiFePO$_4$/C	Carbon particles distributed on LiFePO$_4$ films	312 mA h g^{-1} (at 1.2 C)	70@20@1.2 C	1 M LiClO$_4$ in PEC	−1.6–1.0 vs Ag/Ag$^+$	[132]
LiFePO$_4$/C	Carbon-coated microspheres	163.1 mA h g^{-1} (at 0.1 C)	95.3@1000@5 C	1 M LiPF$_6$ in EC-EMC-DEC	2.3–4.3 vs. Li/Li$^+$	[133]
LiFePO$_4$-CNT	LiFePO$_4$ particles embedded in CNT network	158 mA h g^{-1} (at C/5)	-	1 M LiPF$_6$ in EC-DEC	2.8–4.2 vs. Li/Li$^+$	[134]
LiFePO$_4$/C	Carbon layer coating on sphere	150 mA h g^{-1} (at 1 C)	-	1 M LiPF$_6$ in EC-DMC	2.4–4.0 vs. Li/Li$^+$	[135]
LiFePO$_4$/CNT	CNTs covered by LiFePO$_4$ layer	167 mA h g^{-1} (at 0.1 C)	-	1 M LiPF$_6$ in EC-DEC-EMC	2.5–4.2 vs. Li/Li$^+$	[78]
LiFePO$_4$/C	Carbon-Coated LiFePO$_4$ Nanoplate Microspheres	158 mA h g^{-1} (at 0.1 C)	-	1 M LiPF$_6$ in EC-DMC-EMC	2.0–4.2 vs. Li/Li$^+$	[136]
LiFePO$_4$/C	Carbon coated LiFePO$_4$ nanoparticles embedded in cubic carbon	184.8 mA h g^{-1} (at 0.05 C)	96.7@1000@10 C	1 M LiPF$_6$ in EC-DEC	2.6–4.2 vs. Li/Li$^+$	[137]
LiFePO$_4$/C-N+B	B+N co-doped carbon coated	121.6 mA h g^{-1} (at 20 C)	79.6@50@20 C	1 M LiPF$_6$ in EC-DMC	2.0–4.2 vs. Li/Li$^+$	[138]
LiFePO$_4$/C	LiFePO$_4$ Nanoparticles embedded in Carbon	145 mA h g^{-1} (at C/9)	97@700@1.5 C	1 M LiPF$_6$ in EC-DMC-DEC	2.2–4.2 vs. Li/Li$^+$	[143]
LiFePO$_4$@C/CNT	Carbon coated nanoparticles connected by CNTs	160 mA h g^{-1} (at 0.2 C)	98.5@500@1 C	1 M LiPF$_6$ in EC-DMC-DEC	2.2–4.2 vs. Li/Li$^+$	[112]
LiFePO$_4$/C	Carbon coated nanoparticles	160.3 mA h g^{-1} (at 0.1 C)	91.4@200@5 C	1 M LiPF$_6$ in EC-DMC	2.5–4.2 vs. Li/Li$^+$	[144]
LiFePO$_4$/C	LiFePO$_4$ embedded in carbon	166 mA h g^{-1} (at 0.1 C)	91@1000@10 C	1 M LiPF$_6$ in EC-DMC	2.0–4.2 vs. Li/Li$^+$	[146]
LiFePO$_4$/rGO	Nanosheet	102 mA h g^{-1} (at 30 C)	93.4@500@20 C	1 M LiPF$_6$ in EC-DEC	2.0–4.2 vs. Li/Li$^+$	[29]
LiFePO$_4$/GO	Micro-spherical	158.1 mA h g^{-1} (at 0.1 C)	91.2@2000@10 C	1 M LiPF$_6$ in EC-PC-EMC	2.0–4.2 vs. Li/Li$^+$	[147]
LiFePO$_4$/C	Flower-like	90 mA h g^{-1} (at 10 C)	84@500@5 C	1 M LiPF$_6$ in EC-DMC	2.0–4.2 vs. Li/Li$^+$	[83]
LiFe$_{0.9}$P$_{0.95}$O$_{4-\delta}$	Nanoparticle	166 mA h g^{-1} (at 2 C)	-	1 M LiPF$_6$ in EC-DMC	2.5–4.3 vs. Li/Li$^+$	[148]
LiFe$_\alpha$Ni$_\beta$Co$_\gamma$PO$_4$	Powders	150 mA h g^{-1} (at 2 C)	-	1 M LiPF$_6$ in EC-DMC	2.8–4.2 vs. Li/Li$^+$	[119]
Li$_{1.009}$Fe$_{0.383}$Ni$_{0.081}$Co$_{0.694}$(PO$_4$)$_{1.000}$	Nanoparticles	125 mA h g^{-1} (at 0.5 C)	-	1 M LiPF$_6$ in EC-DMC	3.5–5.0 vs. Li/Li$^+$	[105]
Li$_{0.99}$La$_{0.01}$Fe$_{0.9}$Mg$_{0.1}$PO$_4$/C	Nanoparticles	160.2 mA h g^{-1} (at 0.2 C)	-	1 M LiPF$_6$ in EC-DEC	2.5–4.2 vs. Li/Li$^+$	[126]
LiFePO$_4$/CNT	Nanoparticles intertwined by CNT	112 mA h g^{-1} (at 5 C)	93.6@250@1 C	1 M LiPF$_6$ + VC in EC-EMC-DEC	2.0–4.3 vs. Li/Li$^+$	[155]
LiFePO$_4$/rGO	-	150 mA h g^{-1} (at C/4)	91@100@C/4	1.0 M LiTFSI in EC-DEC	2.0–4.3 vs. Li/Li$^+$	[156]
LiFePO$_4$/C	Carbon coated nanoparticles	148.6 mA h g^{-1} (at 0.1 C)	94.1@65@0.1 C	1 M LiPF$_6$ in EC-DEC	2.5–4.3 vs. Li/Li$^+$	[165]

Notes: a PEC: propylene carbonate; VC: vinylene carbonate.

b Cycling stability is expressed as capacity retention after charging/discharging cycles at a specific rate.

ally no capacity loss and almost 100% coulombic efficiency. In addition, the reversible capacity of C-LFP after 1000 cycles at 10 C remained at 116 mA h g^{-1} with a capacity retention of 84%, while the unmodified LFP exhibited 48 mA h g^{-1} at 10 C after 1000 cycles with 63% capacity retention under identical testing conditions (Fig. 7c-g). This confirmed the important role of carbon coating in enhancing the electrochemical performance of LFP. Liu et al. [129] used poly(vinyl alcohol) as the carbon source and prepared another core-shell structured LFP/C where a thin carbon-shell (about 1.3 nm) was coated completely on the inner LFP. The resulting LFP/C nanocomposite allowed electron transfers from all directions, and Li$^+$ could penetrate through the carbon-shell without appreciable polarization. Consequently, the rate capability of the lithium insertion reaction and electrochemical performance were improved significantly, as compared to the unmodified counterpart, even at high charge–discharge rates of 30 C reaching a discharge capacity of 107 mA h g^{-1} and almost no capacity fading after 1000 cycles.

Zhang et al. [130] prepared mesoporous biocarbon nanowire-coated LFP (MBCNW-LFP) by using ATP as the phosphorus source, nucleating agent, biocarbon source and structural template. High-energy quantum dots (HEQDs) were homogeneously formed inside the ultra-thin LFP NSs, which were coated with the mesoporous biocarbon nanowire network on the surface, leading to formation of storage sites of Li$^+$ and fast transfer kinetics of electrons/lithium ions. As a result, as compared to conventional LFP nanoparticle (10-100 nm) cathodes, the MBCNW-LFP-HEQD cathode showed a better discharge capacity and cycling stability, surpassing the theoretical capacity (170 mA h g^{-1}). Similarly, inspired by the structure of mitochondrion, Yasmin and co-workers [131] prepared a biomimetic "mitochondrion lithium iron phosphate (MC-LFP) (65 ± 8 nm diameter and 350 to 400 nm length), where two layers of carbon were uniformly coated onto the surface of LFP (Fig. 7h-j). Compared with monolayered mitochondrial LFP (MMC-LFP), the dual-layered MC-LFP (DMC-LFP) exhibited an improved battery performance with a decreased charge transfer resistance and enhanced Li$^+$/charge transfer. The discharge capacities were found to be 168 mA h g^{-1} at 0.1 C and 138 mA h g^{-1} at 10 C. Moreover, the MC-LFP showed excellent charge-discharge cycling stability, within only a 7% decay of the capacity at 10 C after 1000 cycles.

LFP/C nanocomposites have also been co-synthesized with carbon where each particle is encapsulated within a good electrical conductor, whereas the lattice electrical conductivity or the diffusion coefficient of lithium within the crystal is not affected [28]. For example, Liu et al. [132] prepared a sol-gel derived nanostructured LFP/C nanocomposite film cathodes by co-synthesizing LiOH H$_2$O, Fe(NO$_3$)$_3$ 9H$_2$O, H$_3$PO$_4$, and L-ascorbic acid C$_6$H$_8$O$_6$, which possessed a high electrochemical performance with an initial discharge capacity of 312 mA h g^{-1} and good cyclic stability (218 mA h g^{-1} after 20 cycles). Xu et al. [133] synthesized interconnected LFP/C microspheres with subtle mesoporous structures formed inside the multiple carbon conductive networks (Fig. 7k-l), leading to facile electron transfer and Li$^+$ transport and hence an excellent rate and cycling performance.

In addition to carbon coating, formation of nanocomposites with CNT is another effective strategy. For example, Varzi et al. [134] prepared a multiwalled CNT-LFP composite cathode and carbon-coated ZnFe$_2$O$_4$ anode for a battery (ZFO/LFP-CNT cells). It was found that the sub-micron LFP particles were embedded within an extensive network of multiwalled CNTs (Fig. 8a), which allowed for efficient and rapid electron transport. Additionally, the excess of CNTs afforded sufficient space between the particles and thus facilitated electrolyte permeability, resulting in high-rate performance. In fact, when the applied rate reached 10 C and 20 C, such electrodes still afforded a specific capacity of 90 and 60 mA h g^{-1}, respectively (Fig. 8b). The assembled ZFO/LFP-CNT cells retained more than 50% of the initial capacity at ≈ 20 C and 85% after 10,000 cycles. Similarly, Brutti et al. [135] reported a high-power, low-cost LIB by combining a refined carbon-coated LFP cathode and a nanostructured Sn-C anode.

The combination of structural engineering and formation of composites with other active materials is an efficient way to improve the performance. For example, Liu et al. [78] synthesized LFP/CNT composites, where the exterior surface of CNTs was uniformly covered with a LFP layer of about 33 nm in thickness via an ALD approach (Fig. 8c and e). Subsequent thermal annealing reduced the thickness of the LFP layer to 20 nm with a small portion of the underlying CNT surface exposed (Fig. 8d, f and g). This unique nanostructure led to improved electron transfer, fast ionic diffusion and rapid Li$^+$ insertion and extraction. Consequently, an exceptional battery performance was observed as a cathode material, with an excellent rate capability (retaining almost the same rate performance when cycling from 0.1 to 60 C was repeated), high power density (discharge capacity of 71 mA h g^{-1} at 60 C), and long lifetime (discharge capacity of 120 mA h g^{-1} after 2000 cycles at 1 C).

Formation of a hierarchical nanostructure is another strategy to improve the performance of LFP-based LIBs. For example, Wu et al. [136] prepared a hierarchical carbon-coated LFP nanoplate microspheres (LFP/C NMs) (Fig. 8h). CV measurements demonstrated that the hierarchical interconnected network of nanoplates in LFP/C NMs exhibited faster kinetics of lithium insertion and extraction than the nanoparticle counterpart (LFP/C NPs) (Fig. 8j). Moreover, the hierarchical structure was found to possess more surface sites for Li$^+$ to react with the LFP/C microsphere, and hence a better rate capability, cycle performance, and higher specific capacity than LFP/C NPs (Fig. 8k-l). Note that LFP/C NMs also exhibited enhanced structural stability, as manifested in X-ray diffraction (XRD) measurements.

Note that in these composite structures, the electrochemical performance is also correlated to the morphological and porosimetric characteristics of the carbon component [38]. For example, Saikia et al. [137] encapsulated LFP NPs within 3D interpenetrating mesoporous carbon via an impregnation method, and the resulting nanocomposites were further coated with carbon. The close contact between LFP NPs and supported cubic carbon matrix was found to facilitate rapid electron transfer during Li$^+$ insertion/extraction, as well as restrict particle growth and aggregation, leading to an excellent rate capability (184.8 mA h g^{-1} at 0.05 C) and long cycle stability (120 mA h g^{-1} with 96.7% capacity retention after 1000 cycles at 10 C).

Further improvement of the electrochemical performance can be achieved by coating the LFP electrode with doped carbon. In a recent study by Zhang et al. [138], the performance of N and B doped LFP/C (*i.e.*, LFP/C-N and LFP/C-B) was improved by modifying LFP/C-N with boron. The resulting LFP/C-N+B was found to possess good electrical conductivity (1.36 × 10^{-1} S cm^{-1}) and a much superior rate capacity (121.6 mA h g^{-1} at 20 C) than LFP/C (101.1 mA h g^{-1} at 20 C), due to the synergistic electrochemical activity and electron and hole-type carriers donated by nitrogen and boron dopants. Carbon, a good electronically conducting material, could be transformed into nanoporous structure to composite active materials. However, different types of porosity of nanoporous carbon function differently during the process of electrochemical charge-discharge. According to the International Union of Pure and Applied Chemistry, pore structures with a diameter of >50 nm are defined as macropores, 2−50 nm as mesopores, and <2 nm as micropores. Generally, macropores act as ion-buffering reservoirs and mesopores serve as ion highways allowing for very fast ion transport into the bulk of the electrode material, while some of the micropores significantly affect the diffusion of ions and molecular sieving due to failing to adsorb ions, thereby changing its capacity [139]. The presence of micropores provides a large surface area to accommodate ions, while both mesopores and macropores facilitate the rapid ion transport under dynamic polarization conditions [140]. However, higher specific surface area not always redound to higher electrochemical performance due to a sieving effect of the electrolyte ions, and adequate pore size is more important than a high surface area to obtain high value of capacitance [141]. Optimizing the pore size of porous carbon electrodes to match the size of a dissolved ion, maximum capacity could be attained
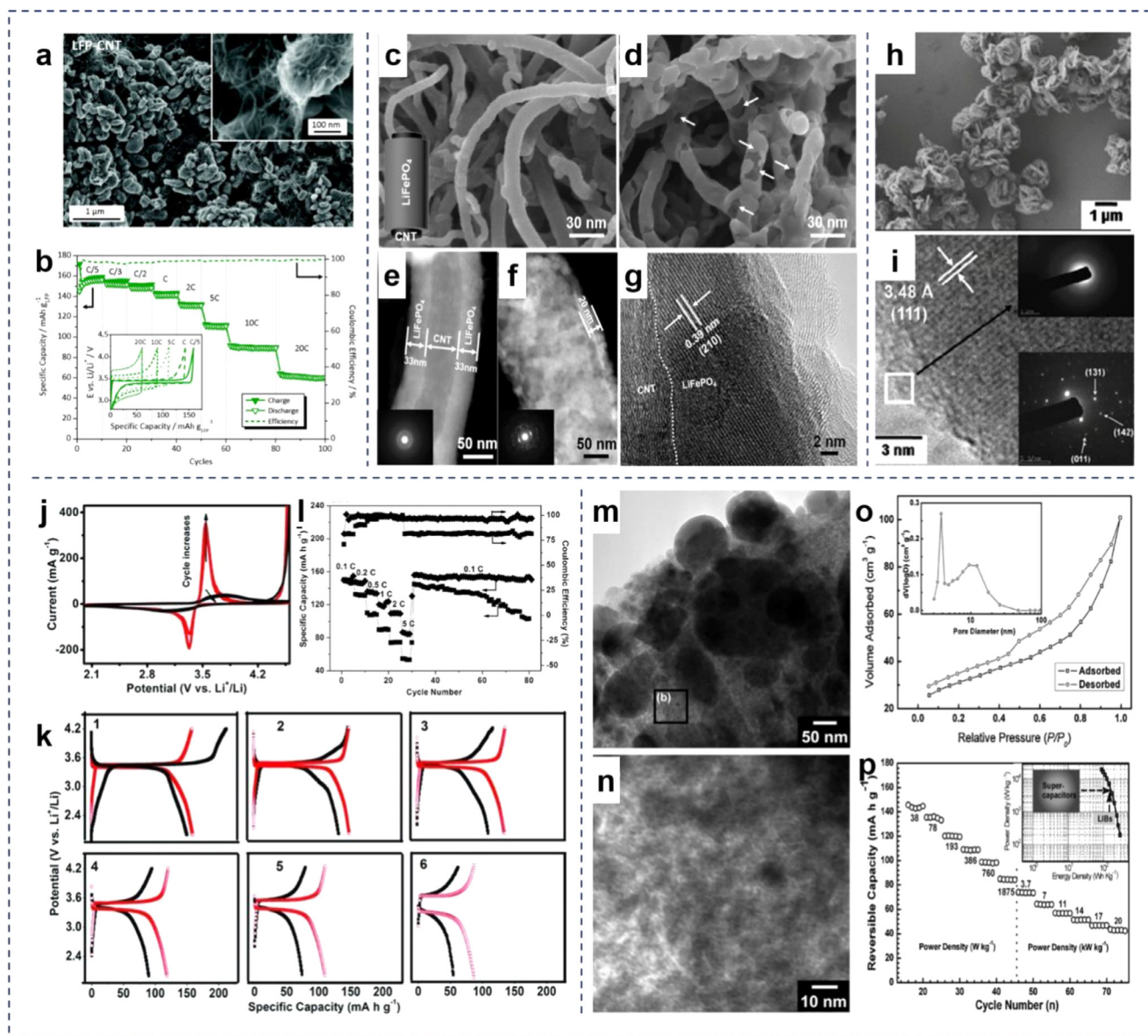
Fig. 8. (a) SEM images of LFP-CNT positive electrodes, inset: the connection network established by CNT between the LFP particles, and (b) rate capability and coulombic efficiency of LFP-CNT cathodes (in half-cell configuration *vs.* Li) at C rates ranging from C/5 to 20 C. Inset: some selected potential profiles at different current loads. (a, b) Reproduced with permission [134]. Copyright 2014, Wiley-VCH. SEM images of (c) as-deposited LFP/CNTs and (d) annealed LFP/CNTs. Scanning transmission electron microscopy (STEM) images of (e) as-deposited LFP/CNTs and (f) annealed LFP/CNTs (the insets in (e) and (f) are their corresponding selected area electron diffraction (SAED) patterns). (g) High-resolution TEM (HRTEM) image of the annealed LFP/CNTs. (c-g) Reproduced with permission [78]. Copyright 2014, American Chemical Society. (h) FESEM images of LFP/C NMs, and (i) HRTEM image and SAED pattern (inset) of LFP/C NPs; Electrochemical characterization of LFP/C NMs electrodes (red) and LFP/C NPs electrodes (black); (j) Cyclic voltammograms with the first three cycles between 2.0 to 4.6 V (*vs.* Li/Li$^+$) at a scan rate of 0.1 mV s^{-1}. (k) Charge-discharge galvanostatic curves (c) at rates of (1) 0.1 C, (2) 0.2 C, (3) 0.5 C, (4) 1 C, (5) 2 C, and (6) 5 C between 2.0 and 4.2 V (0.1 C rate corresponds to 17 mA g^{-1}), and (l) coulomb efficiency and variation in specific capacities *vs.* cycle numbers of LFP/C NMs (□) and LFP/C NPs (■) cycled from 0.1 to 5 C between voltage limits of 2.0 and 4.2 V. (h-l) Reproduced with permission [136]. Copyright 2011, Wiley-VCH. (m) TEM, and (n) HRTEM image, and (o) nitrogen adsorption/desorption isotherms of the LFP-NP@NPCM nanocomposite; (p) Rate performance at different power density, the inset showed the Ragone plots for the nanocomposite and commercially available supercapacitor electrodes. (m-p) Reproduced with permission [143]. Copyright 2009, Wiley-VCH.

[142]. Hierarchical porous carbon (HPC) structure with interconnected pores of distinct sizes providing high surface areas (with micropores) on the one hand and secondary transport pore systems built-up by larger pores on the other hand [139]. It is worth mentioning that dispersion of the pore size and operating voltage window also have effect on capacitance, which has been studied in detail by Kondrat et al. [142]. Thus, optimal micropore size, which is different for each electrolyte system and at different voltage windows, and introducing secondary pores are of particular interest to tailor pores in carbon materials. Wu et al. [143] prepared a nanoporous carbon matrix which served as an elec-

trolyte container for high-rate operation as well as an elastic buffer to relieve the strain during Li uptake/release by dispersing nanoparticles of active materials into a nanoporous carbon matrix (NP@NPCM). As shown in Fig. 8m-o, LFP nanoparticles of about 60-100 nm in diameter were embedded in a nanoporous carbon matrix forming pores of about 3-10 nm. The LFP nanoparticles decreased the Li$^+$ diffusion time in the crystal lattice resulting in a high power. The carbon matrix provided a conducting 3D network that allowed both Li$^+$ and e$^-$ to migrate and reach the LFP nanoparticles. Moreover, the carbon matrix could serve as an electrolyte container for high-rate charging/discharging. Due
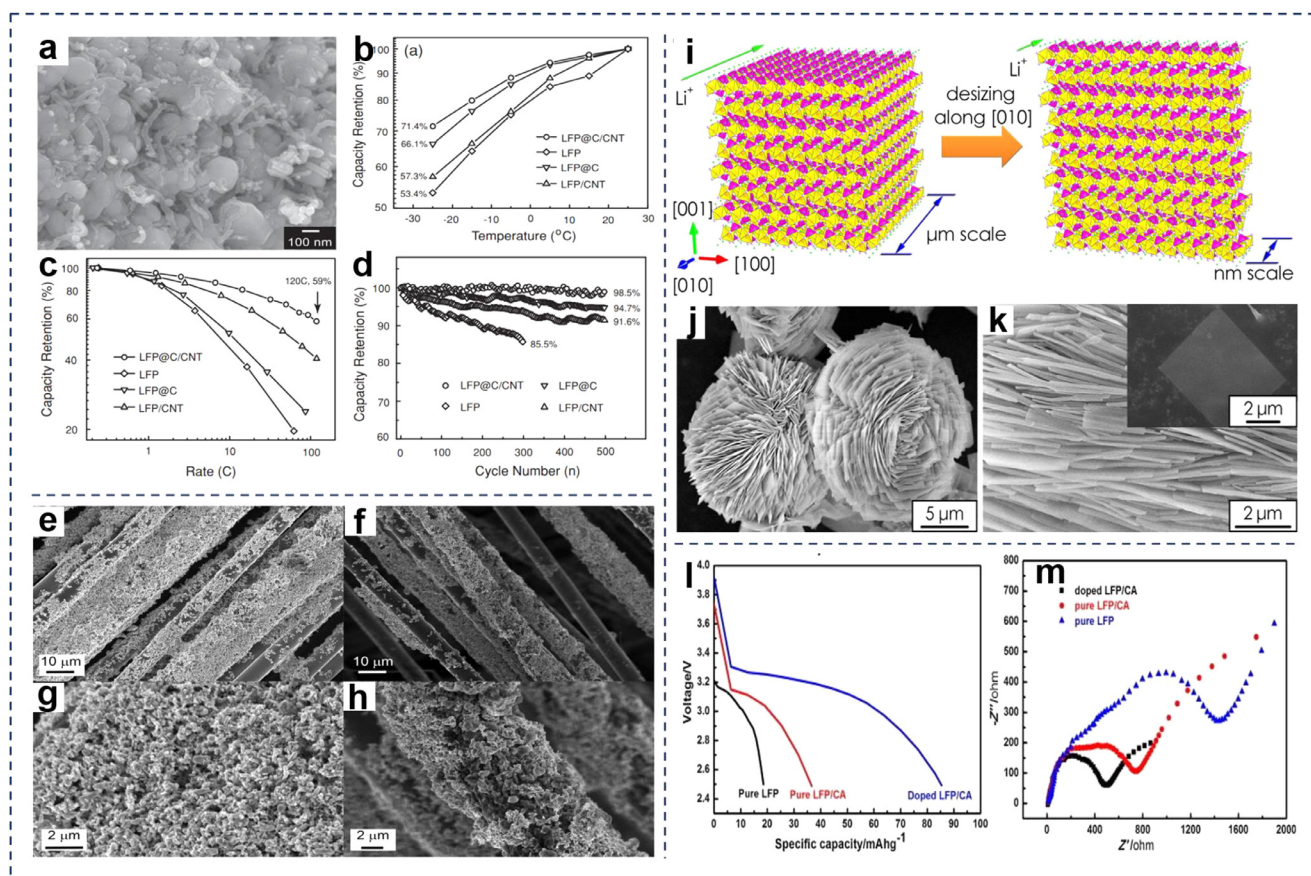
Fig. 9. (a) SEM of the prepared LFP@C/CNT nanocomposite. (b) Capacity retention on temperature in the range of −25℃ to 25℃ for LFP@C/CNT, LFP@C, LFP/CNT, and pristine LFP; The comparisons of (c) rate and (d) cycling performances of LFP@C/CNT, LFP@C, LFP/CNT, and pristine LFP. (c-d) Reproduced with permission [112]. Copyright 2013, Wiley-VCH. SEM images of carbon fibers EPD coated with the composition 88:6:6: (e, g) before cycling, and (f, h) after cycling. (e-h) Reproduced with permission [145]. Copyright 2018, Elsevier. (i) Schematic illustration of crystal structure and shortening the lithium-ion diffusion distance along the [010] of LFP crystals. (j) SEM image of the as-synthesized LFP particles, and (k) SEM image showing the latitudinally accumulated NSs. (i-k) Reproduced with permission [83]. Copyright 2014, American Chemical Society. (l) Cycle stability of doped LFP/CA at −20 ℃, and (m) impedance spectra of doped LFP/CA compared with pure LFP, pure LFP/CA under 10 C at −20 ℃. (l, m) Reproduced with permission [126]. Copyright 2012, Elsevier.

to this dual functional nanoporous carbon network and LFP nanoparticles, the LFP-NP@NPCM nanocomposite showed a high high-power density up to 20 kW kg^{-1}, rapid discharge or charge process in about 16 s (corresponding to a rate of 230 C), and discharge energy density of 87 Wh kg^{-1} (Fig. 8p). Wu et al. [112] employed two types of nanocarbons (amorphous carbon and graphitized conducting carbon) to modify LFP by forming a double nano-carbon decorated LFP nanocomposite (LFP@C/CNT). As can be seen from the SEM image (Fig. 9a), carbon-coated LFP NPs were connected electrically by CNTs forming a 3D conducting network. Compared to the pristine nano-LFP and single-carbon modified LFP (*i.e.*, LFP@C and LFP/CNT), LFP@C/CNT showed a superior performance at low temperature (about 71.4% capacity retention when discharged at −25℃, Fig. 9b), high-rate (about 59% capacity retention at rates up to 120 C, Fig. 9c), and a long cycle life (98.5% capacity retention over 500 cycles at 1 C, Fig. 9d). These properties might result from the synergistic effect between amorphous carbon coating which could promote Li$^+$ diffusion, stabilize the interface of the LFP NPs as well as the graphitized conductive CNTs, and decrease the internal resistance. Using polyoxyethylenesorbitan monooleate (Tween80) as the carbon source, Huang et al. [144] prepared a carbon-coated LFP/C composite cathode, which exhibited a higher capacity retention than the sample using glucose as the carbon source. The former electrode was found to display a lower charge transfer resistance than the latter after 100 and 200 cycles at 5 C rate. In the composite, the Tween80 surfactant molecules bonded to the surface of LFP and formed an ad-

sorption layer, leading to the formation of a homogeneous carbon layer tightly coated onto the LFP surface. Hagberg et al. [145] prepared a LFP electrode based on carbon nanofibers, where LFP particles, conductive additive and binder (polyvinylidene difluoride, PVDF) were dispersed on the surface of carbon fibers by electrophoretic deposition (EPD). As shown in Fig. 9e-h, the coating adhered strongly to the carbon fibers and was unaffected by continuous cycling. Three-point bending tests suggested that this material showed good mechanical properties for structural battery applications. Using mesoporous carbon as templates, Wang et al. [146] used a nanocasting technique to prepare high-rate mesoporous LFP/C cathodes, where electrolyte could easily penetrate into the mesopores to contact the embedded LFP particles. This mesoporous nanoarchitecture ensured not only intimate contact between liquid electrolyte and active LFP NPs, but also high electrical conductivity for both fast mass transfer and acharge transfer. Tested in a half-cell, the LFP/C mesoporous nanocomposites achieved a high capacity (166 mA h g^{-1} at 0.1 C rate) and an ultrahigh rate capacity (118 mA h g^{-1} at 10 C rate) with an excellent cycle life (91% after 1000 cycles at 10 C)

4.2.1.1.2. Graphene-based composites. GO is another interesting choice to improve the electrical conductivity of olivine LFP. For example, Yang et al. [29] successfully prepared ultrathin LFP-NSs, which were then self-assembled with GO. The resulting LFP-NSs/rGO nanocomposites were found to possess ultrashort diffusion pathways to Li$^+$ and excellent conductive networks, which were conducive to rapid diffusion of Li$^+$ and electron transfer and thus excellent rate performance (102 mA h

g^{-1} at 30 C) and discharge capacity retention (93.4% after 500 cycles). Similarly, microwave-exfoliated GO (MEGO) was adopted to forming LFP/MEGO composite. Compared with thermally exfoliated GO (TEGO), the obtained LFP/MEGO composites exhibited a better specific energy (518.1 W h kg^{-1}) and energy efficiency (89.8%). Remarkably, the rate performance is much better than LFP/TEGO delivering an excellent specific energy density of 300.3 W h kg^{-1} and 229.7 W h kg^{-1} at the high rate of 10 C and 20 C [147].

Notably, both the size and orientation control of LFP are necessary, because Li$^+$ diffusion in LFP can only occur along the a [010] direction, as shown in Fig. 9i [83]. Thus, LFP particles with a large [010] surface area can effectively improve the active area and decrease the diffusion distances for Li$^+$. Zhao et al. [83] prepared monocrystalline [010]-oriented LFP NSs by exfoliation bulk LFP which displayed a flower-liked structure assembled from latitudinally accumulated NSs (Fig. 9j-k). The exfoliated LFP NSs were found to display over 93% of the [010] facet, and a large pore density for Li$^+$ insertion/extraction. After an annealed process and coating with a thin carbon layer, LFP NSs exhibited much higher electrical conductivity (1.8 S cm^{-2}) and lower resistance (66.5 Ω cm^{-2}) than commercial LFP/C powders (0.4 S cm^{-2}) and (74.4 Ω). Moreover, the Li$^+$ diffusion coefficient of LFP NSs (6.2 × 10^{-13} cm^2 s^{-1}) was higher than that of commercial LFP/C powders (8.3 × 10^{-14} cm^2 s^{-1}). Meanwhile, the potential interval (180 mV) of LFP NSs between the anodic and cathodic scans was much lower than that (340 mV) of the commercial powders. For these reasons, the LFP NS electrode showed high specific capacity, excellent rate capability (90 mA h g^{-1} at a current rate of 10 C), and stable cyclability (70 mA h g^{-1} at current rate of 5 C over 500 cycles).

In addition, increasing diffusion across the surface towards the [010] facet can also enhance rate capability. For example, Kang et al. [148] prepared an off-stoichiometry LiFe$_{0.9}$P$_{0.95}$O$_{4-\delta}$ material, which exhibited both a high energy density and an ultrahigh discharge rate, comparable to those of supercapacitors. This material realized high lithium bulk mobility, as off-stoichiometry created a fast ion-conducting surface phase. Compared with stoichiometric LFP, LiFe$_{1-2y}$P$_{1-y}$O$_{4-d}$ possessed a higher rate capability resulting from the pyrophosphate coating. It was found that transport across the surface was facilitated by a poorly crystallized layer with high Li$^+$ mobility. The amorphous nature of the coating removed the anisotropy of the surface properties and enhanced delivery of Li$^+$ to the [010] facet of LFP where it could be inserted. The disordered coating material modified the surface potential of lithium and facilitated the adsorption of Li$^+$ from the electrolyte by providing different lithium sites with a wide range of energies that could be matched to the energy of lithium in the electrolyte. As a result, an extremely high rate could be achieved for the active material: at a 200 C rate, over 100 mA h g^{-1} could be achieved and a capacity of 60 mA h g^{-1} was still obtained at a 400 C rate.

4.2.1.1.3. Doping products. Introduction of foreign atoms into host materials could modify the physical and chemical surroundings of the host lattice and optimize the electrochemical performance. Doping technique which can increase the lattice electronic conductivity has also been extensively applied to improve electrical conductivity, reduce Li$^+$ migration barriers, and tune voltage window of battery materials. A wide range of dopants have been reported to substitute Li, Fe, or O ions in LFP to improve its electrical conductivity [18]. Charge compensation vacancies accomplished through aliovalent doping reduces the grain size and widens the Li$^+$ migration path resulting in faster Li$^+$ diffusion [149]. For instance, by heterogeneous doping, Adams [30] realized ultrafast Li$^+$ migration in the surface of modified LFP. The heterogeneous doping in LFP nanocrystals by glassy Li$_4$P$_2$O$_7$ enhanced the room temperature Li$^+$ diffusion by about three orders of magnitude along the Li$^+$ channel direction. Moreover, the supervalent dopants (namely Cr^{3+}, Ti^{4+}, and Nb^{5+}) were reported to successfully substitute in the olivine to improve the electrical and ionic conductivities. For example, by selectively doping with supervalent cations, Chung et al. [119] synthesized a series of doped LFP materials using NH$_4$H$_2$PO$_4$, FeC$_2$O$_4$ 2H$_2$O,

and Li$_2$CO$_3$ as the source of LFP and MgC$_2$O$_4$ 2H$_2$O, Al(OC$_2$H$_5$)$_3$, Ti(OCH$_3$)$_4$(CH$_3$OH)$_2$, Zr(OC$_2$H$_5$)$_4$, Nb(OC$_6$H$_5$)$_5$, and W(OC$_2$H$_5$)$_6$ as the dopant source. The electronic conductivity of doped LFP was increased by a factor of more than 10^8 relative to the pure endmember, reaching values of >10^{-2} S cm^{-1} at room temperature. As-obtained LFP exhibited a high capacity of 170 mA h g^{-1} (near the theoretical value) at low current densities, and still retained at 6000 mA g^{-1}. The effects of firing temperature in synthesized process has been investigated that the electronic conductivity dominated at high temperatures, and these doped compositions treated at 700 or 800°C were observed to be p-type. Considering the effect of dopant concentration, doping levels of 0.1, 0.5 and 1.0 atom% Nb in LFP showed room-temperature conductivities of 1.1 × 10^{-3}, 4.1 × 10^{-2}, and 2.2 × 10^{-2} S cm^{-1}, respectively. When the concentration reached up to 2 and 4 atom%, Nb-enriched impurity phases appeared, and the conductivity decreased to 2.8 × 10^{-3} and ~10^{-6} S cm^{-1}, respectively, which demonstrates that the dopant concentration is an important factor for consideration in doping. Besides unitary doping, binary doped LFP has also attracted extensive attention. The substitution of iron in LFP lead to high working potentials of batteries, and by chaning the molar ratio of the substituent metal ions, the working potential can be optimized [150]. Taking LiFe$_\alpha$Ni$_\beta$Co$_\gamma$PO$_4$ as an example, Gioele [105] synthesized five types of nickel and cobalt co-doped lithium-based cathode materials with various nickel and cobalt contents including Li$_{1.030}$Fe$_{0.380}$Ni$_{0.692}$Co$_{0.080}$(PO$_4$)$_{1.000}$, Li$_{1.062}$Fe$_{0.390}$Ni$_{0.570}$Co$_{0.201}$(PO$_4$)$_{1.000}$, Li$_{1.000}$Fe$_{0.394}$Ni$_{0.375}$Co$_{0.394}$ (PO$_4$)$_{1.000}$, Li$_{1.040}$Fe$_{0.381}$Ni$_{0.187}$Co$_{0.569}$(PO$_4$)$_{1.000}$, and Li$_{1.009}$ Fe$_{0.383}$Ni$_{0.081}$Co$_{0.694}$(PO$_4$)$_{1.000}$. With changing the molar ratio of nickel to cobalt, the working potential of the electrode can be controlled in a range of 3.5 to 4.8 V. Electrochemical characterizations showed that the material with the highest cobalt content exhibited the best performance in terms of rate capabilities, high working potentials (above 4.5 V), good capacities (125 mA h g^{-1}), and exceptional energy densities (560 mW h g^{-1}). Moreover, different ratios of cobalt to nickel did not affect the olivine structure of the compounds but significantly modulated the electrochemical properties of the materials: (1) the electronic density states of insertion/de-insertion Li$^+$ channels varied; (2) the crystal cell volume increased with increasing cobalt content. Another example was the work developed by Zhang et al. [126] who synthesized olivine-type lanthanum and magnesium doped Li$_{0.99}$La$_{0.01}$Fe$_{0.9}$Mg$_{0.1}$PO$_4$/carbon aerogel (doped LFP/CA) composite via a simple solution impregnation process. Compared with pure LFP and pure LFP/CA, doped LFP/CA composite cathode material exhibited better electrochemical performance under low temperatures (*e.g.*, −20 °C) at 10 C (Fig. 9l-m). Conductivity test results showed that the electronic conductivity was efficiently improved by co-doping and CA coating, which could be ascribed to cation defects that was beneficial to fast diffusion of Li$^+$ in solid phase and resulted from cation doping into the olivine structure.

4.2.1.1.4. Other modification strategies. Influence factors such as binder, conductive additive, electrolyte, and the structure of electrode have also showed significant impacts on the performance of commercial LIB electrodes [151]. Shi et al. [152] developed a 3D nanostructured hybrid inorganic-gel framework electrode by *in situ* polymerization of conductive polymer gel onto commercial LFP particles. In such electrodes, highly conductive and hierarchically porous network promoted both electronic and ionic transports and thus efficiently improved rate and cyclic performance. Also, because of the polymer coating, both inorganic and organic components were uniformly distributed within the electrode, which mechanically supported active materials and enhanced the long-term electrochemical stability of electrodes. Through investigating the effects of conductive carbon and polymer on the LFP particles, Vicente et al. [153] found that electrodes with both additions showed similar electrochemical performance with reduced resistances but poly(3,4-ethylenedioxythiophene) (PEDOT) was more effective to reduce the resistance that the reduced value was one order of magnitude higher than that of C-coating. When the charge/discharge current in-

creased, the specific capacity of LFP/PEDOT (blend) almost maintained (130 mA h g^{-1} at 2 C) while for C-LFP, the specific capacity decreases notably. Moreover, various polymer binders were investigated to improve the performance of LFP electrodes [100,134,148]. For example, compared to conventional PVDF binder with high molecular weights (1,000,000), a novel binder, namely spandex, with relatively low molecular weight of around 300,000 has been developed by Lee et al. [25]. The incorporation of L-spandex was demonstrated that its functional groups in the hard domains involving hydrogen bonding could enhance cohesion among electrode components and improve adhesion between electrode film and current collector. As a result, a more stable solid permeable interface (SPI) layer was formed and thus the L-spandex electrode provided superior rate capability as well as cyclability compared to conventional H-PVDF counterparts. Furthermore, the improved adhesion property of the L-spandex electrode turned out to be suitable for 3D structured electrolyte. Up to now, there have been several types of electrolytes developed based on LFP (such as solid electrolytes, liquid and polymer electrolytes). Suitable electrolyte can not only improve the electrochemical performance of the battery, but also improve its safety and practicability. Fasciani et al. [26] proposed a novel PVDF-based gel polymer electrolyte (GPE) for LIBs. The GPE electrolyte was easy to handle and suitable for roll-to-roll scaling-up fabrication without the use of controlled atmosphere, which allowed the GPE to be stored for a long period. Moreover, the lithium electrode/gel electrolyte interface showed a good stability and a high lithium transference number. And as-prepared full LFP/GPE/graphite cell based on such electrolyte exhibited long cycle life. Another polymer electrolyte based on poly (lactic acid) was also prepared by Osada et al. [27]. By combination of the ionic liquid N-butyl-N-methylpyrrolidinium bis(trifluoromethanesulfonyl) imide (Pyr14TFSI), amorphous, solvent-free, and low-volatile solid polymer electrolytes (SPEs) were obtained. This electrolyte exhibited a low charge transfer resistance and high thermal and electrochemical stability, showing great potential in matching with LFP composite electrode for lithium metal polymer batteries.

4.2.1.1.5. Application for other types of LIBs. In addition to some conventional LIBs, phosphates can be used in other LIBs such as 3D printable LIBs. For example, 3D printable electrode ink containing LFP, carbon nanofibers (CNFs), and polymer was used for synthesis of printable LIBs. By tuning the ratios of these components (*i.e.*, LFP, CNFs, and polymer), the effects on the rheological, electrochemical and mechanical properties could be investigated. And in the composite, CNFs promoted conductivity and contributed to the formation of a porous microstructure, active material increased the cell's electron storage capacity, and PVDF enhanced the mechanical properties. As a result, the resulting free-standing electrodes exhibited excellent cyclability and rate capability [154]. Zhou et al. [155] developed a freestanding 3D-printed LFP microelectrode composed of LFP, carboxymethylcellulose sodium (CMC) and CNT for microbattery. Benefiting from the structure design of electrode and the freeze-drying treatment, a 3D architected microelectrode with hierarchical pores and a continuous conductive network was achieved (Fig. 10a-b). Compared with electrodes prepared through the coating technique, the LFP microelectrodes with high areal loading (32 mg cm^{-2}) showed better rate capacity and cycle stability. Moreover, an ultrahigh areal capacity (5.05 mA h cm^{-2}) could be achieved in such LFP microelectrodes. In addition, LFP could serve as flexible cathode through hybridizing with 2D rGO and then integrating with smart conductive textiles. Because of the flexible 2D graphene template, the conductivity and flexibility of the nanosized electrodes were further enhanced. The LFP/rGO-lithium titanate oxide (LTO)/rGO based batteries achieved high areal capacities of about 1.2 mA h cm^{-2} at a current rate of C/4 while maintaining excellent flexibility [156]. Jae et al. [157] developed a rechargeable lithium ribbon-type battery where double layer LFP served as the cathode and an amorphous silicon film served as anode. In the lithium ribbon-type battery, the performance of LFP cathode was further improved by carbon coating, which shortened the diffusion length of Li$^+$ along the *b*-axis of the crystal. After a few cycles

for stabilizing the amorphous Si film, the Si/LFP ribbon-type battery showed outstanding cycling properties with high coulombic efficiency at all tested rates. Paolella et al. [158] reported a nanocrystal prepared by direct photooxidation in the presence of a dye deposited on conducting glass/F:SnO$_2$ (FTO) as a hybrid photo-cathode in a two-electrode system (Fig. 10a-d). In this hybrid photo-cathode, dye-sensitization generated electron-hole pairs with the holes aiding the chemical conversion of LFP (triphylite) nanoplatelets to FePO$_4$ (heterosite) showing possibilities in designing photo-rechargeable LIBs. LFP microspheres/graphene acting as cathode combined lithium titanate nanospheres/graphene acting as anode has been applied in micro-batteries. This all-solid-state planar lithium ion micro-battery (LIMB) delivered ultrahigh volumetric energy density (125.5 mW h cm^{-3}), and ultralong-term cyclability without capacity loss after 3300 times at room temperature. Remarkably, this LIMB showed extraordinary flexibility without capacity decaying under repeated bending and high-temperature performance up to 1000 cycles operated at 100°C [159]. Similarly, Hassoun et al. [160] also developed a solid-state LIB using LFP as cathode and nanostructured titanium oxide (TiO$_2$) as anode. This battery showed high safety and remarkable environmental compatibility.

Commercial LFP cells are expect to cycle to an end-of-life state and some work have been made to renew the cyclability of materials. Ganter et al. [161] have recovered LFP capacity through electrochemical and chemical re-lithiation techniques. Re-lithiated LFP regained the original capacity of 150-155 mA h g^{-1}. The discharge process of LFP battery was accompanied with exothermic process and endothermic process at a low rate [162]. Considering the safety of LIBs, thermophysical properties of electrical energy storage materials become an essential factor in practical applications. For this reason, Jagjit et al. [163] reported a carbonized mesophase pitch-coated LFP cathode which showed higher thermal diffusivity than conventional LFP-based electrode. Li et al. [164] successfully designed a self-supported ultrahigh-capacity and fire-resistant LFP (UCFR-LFP)-based nanocomposite through a facile electrostatic-assisted self-assembly approach using ultralong hydroxyapatite nanowires (HAP NWs), Ketjen black NPs (KB NPs), carbon fibers (CFs), and LFP powder as starting materials. After the self-assembly and suction filtration processes, the LFP NPs were uniformly embedded in the highly conductive but porous HAP/KB/CF matrix, forming a freestanding, hierarchically-nanostructured UCFR-LFP electrode. Benefiting from the structural and chemical uniqueness, the UCFR-LFP electrode exhibited improved electrochemical performance, high active material loading, outstanding structural stability, and high battery safety compared with the conventional LFP electrode. Notably, the 1D inorganic binder-like ultralong HAP NWs endowed the UCFR-LFP electrode with excellent thermal stability (structural stability up to 1000°C and electrochemical activity up to 750°C), high fire-resistance, and wide-temperature operability. Zhou et al. [165] developed a waste-to-resource strategy to prepare LMP (M = Fe, Mn). They converted bacteria waste used for removing phosphorus contamination from waste water into a LMP NPs. The obtained LMP NPs were enveloped in a carbon layer resulting from the decomposition of the organic matter from the bacterial cell cytoplasm. The bacteria-derived LFP exhibited a high discharge capacity (140 mA h g^{-1}) at 0.1 C with a flat plateau locating at around 3.5 V and showed excellent stability and rate capabilities with a stable discharge capacity (75.4 mA h g^{-1}) at 10 C.

4.2.1.2. LiCoPO$_4$. As shown in Table 5, LiMPO$_4$ (M = Mn, Ni, and Co) with high operation voltage and high theoretical energy density has been widely reported as cathodes for LIBs. Among them, LiCoPO$_4$ (LCP) has a relatively high operation voltage (4.8 V *vs.* Li/Li$^+$) and theoretical energy density (~801 W h kg^{-1}). Taking the advantage of high energy-density of LCP, Ni et al. [166] designed a LCP/Li$_4$Ti$_5$O$_{12}$ battery. Electrochemical tests demonstrated that the battery afforded an operational voltage of 3.2 V and delivered a reversible capacity of 122 mA h g^{-1}. Based on the mass of LCP, the energy density of such a battery could reach 378 mW h g^{-1}, showing great potentials in energy storage appli-
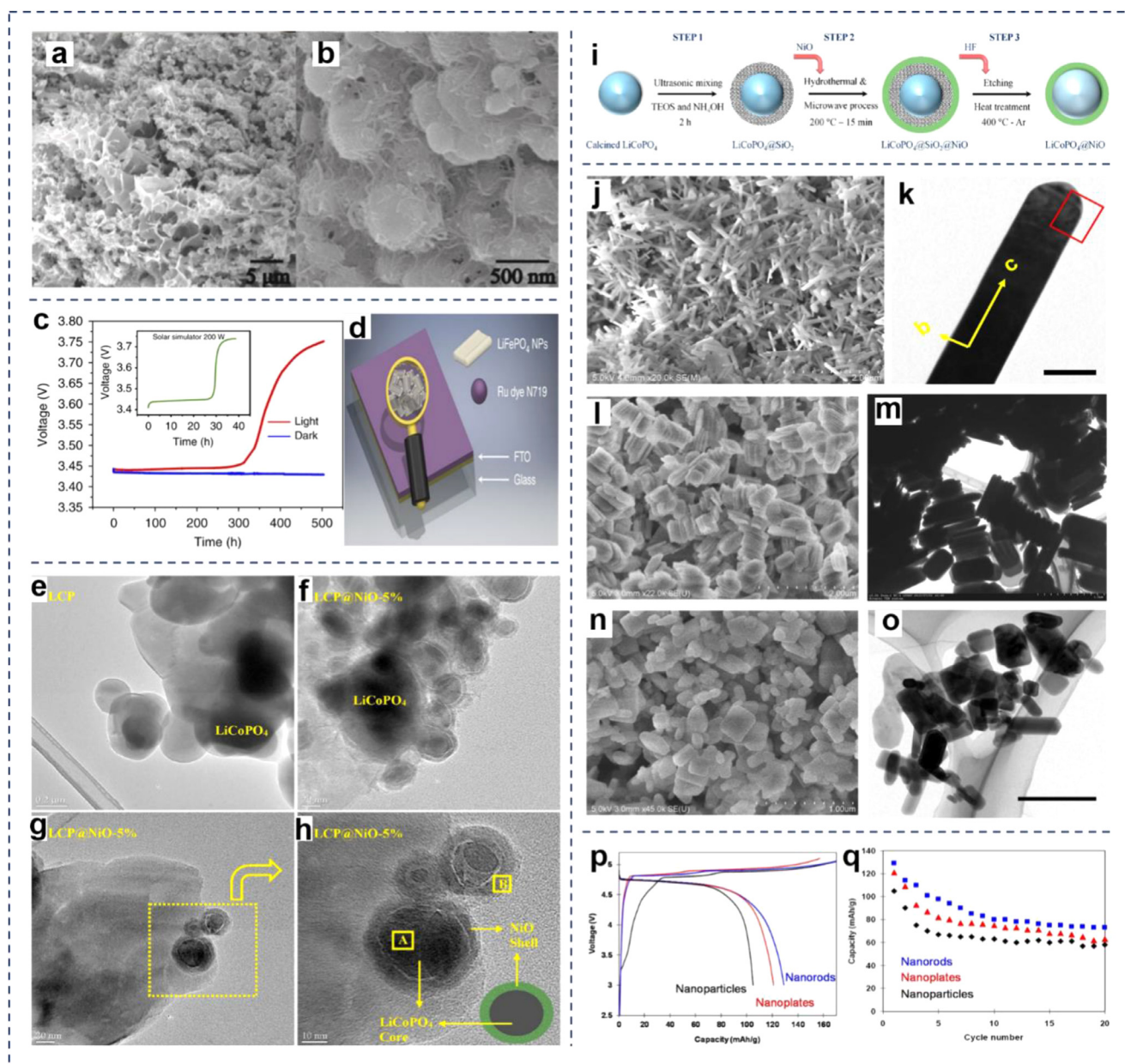
Fig. 10. (a) SEM image of top view of 3D-printed LFP lattice, and (b) magnified morphology of the 3D-printed LFP microlattice. (a, b) Reproduced with permission [155]. Copyright 2019, Wiley-VCH. (c) Open circuit voltage (OCV) under Neon light exposure (red line), the inset showed the change in OCV upon illumination with a solar simulator (green line), and (d) schematic representation of the FTO/LFP NPs/DYE electrode. (c, d) Reproduced with permission [158]. Copyright 2017, Springer Nature. (e-h) HRTEM images of LCP and LCP@NiO-5% samples, and (i) schematic drawing of the NiO-coated LCP NPs using stepwise synthesis methodology. (e-i) Reproduced with permission [169]. Copyright 2017, Elsevier. (J) SEM and (k) TEM image of nanorod particles synthesized with hexamethylenediamine. (l) SEM and (m) TEM image of nanoplate particles synthesized with hexamethylenediamine. (n) SEM and (o) TEM image of NPs synthesized with hexamethylenetetramine. (p) First charge/discharge profiles and (q) cyclic performance of LCP at 0.1 C rate.

cations. Similarly, Du et al. [167] constructed a LCP/Li$_4$Ti$_5$O$_{12}$ battery. But in their test, the full cell displayed two operation voltage plateaus (3.24 V and 3.17 V), which corresponded to the two-step lithium extraction/insertion process occurring in the cell. In the system, increasing the theoretical capacity matching ratio of cathode and anode can contribute to significantly improved discharge capacity and cycling behavior of LCP/Li$_4$Ti$_5$O$_{12}$ system. In order to further improve the performance of LCP, Ni et al. [168] developed LCP/C core/shell structure to address sluggish kinetics and poor cycle stability. The introduction of carbon shell increased the reversible capacity and enhanced the capacity retention during cycling. LCP/C core-shell structure delivered a high specific

capacitance of 131 mA h g^{-1} in a voltage range of 3.0-5.2 V *vs.* Li/Li$^+$ and maintained 78% of initial capacity after 40 cycles at a low specific current of 17 mA g^{-1}. Similarly, in order to enhance the stability of LCP cathode, Ahmet [169] synthesized a nanoscale, NiO-coated LCP cathode (Fig. 10e-h) by three-step synthesis methods (*i.e.*, Stober, hydrothermal, and microwave techniques Fig. 10i). The LCP@NiO displayed a core-shell morphology with a thickness of 7-8 nm. LCP@NiO nanocomposites with different loading amounts of NiO (2.5%, 5.0%) were obtained by mixing LCP@SiO$_2$ powder with nickel oxide in ethanol. The 2.5 wt.% NiO-coated cathode exhibited a high discharge capacity of 159 mA h g^{-1} at 0.l C and excellent cycle performance for first 80 cycles.

Table 5
Performances of recently reported LIBs based on $LiMPO_4$ (M = Co, Ni, Mn) with corresponding morphologies.

Materials	Morphology	Capacitance	Capacitance	Capacity retention [%]	Electrolytes	Voltage, V	Ref.
$LiCoPO_4/C$	Core ($LiCoPO_4$)/shell (carbon)	131 mA h g^{-1} (at 0.1 C)		78@40@0.1 C	1 M $LiPF_6$ in EC-DMC	3.0–5.2 vs. Li/Li$^+$	[168]
$LiCoPO_4$/ NiO	Core ($LiCoPO_4$)/shell (NiO)	159 mA h g^{-1} (at 0.1 C)		85@80@0.1 C	1 M $LiPF_3(CF_2CF_3)_3$ in EC-DMC	3.0–5.2 vs. Li/Li$^+$	[169]
$LiCo_{0.95}Mn_{0.05}PO_4/C$	Carbon coated nanoparticles	140 mA h g^{-1} (at 0.1 C)		91.8@60@0.1 C	1 M $LiPF_6$ in EC-DMC	2.8–5.2 vs. Li/Li$^+$	[170]
$LiCoPO_4$/ $LiFePO_4$	$LiFePO_4$ coated $LiCoPO_4$ particulate	132 mA h g^{-1}		-	1 M $LiPF_6$ in EC-DMC	3.5–5.2 vs. Li/Li$^+$	[171]
$LiCoPO_4$/CNT	CNT-embedded particles	52.5 mA h g^{-1} (at 1 C)		-	$LiPF_6$ in EC-DMC (11.8/ 44.1/44.1 wt.%)	3.0–5.1 vs. Li/Li$^+$	[172]
$LiCoPO_4$	Nanorod	130 mA h g^{-1} (at 0.1 C)		56.6@20@0.1 C	1 M $LiPF_6$ in EC-DMC	3.0–5.1 vs. Li/Li$^+$	[173]
$LiNiPO_4/C$	Core-shell	150.2 mA h g^{-1} (at 0.1 C)		92@100@0.1 C	1 M $LiPF_3(CF_2CF_3)_3$ in EC-DMC	3.2–5.1 vs. Li/Li$^+$	[173]
$LiNiPO_4$/CoO	Core-shell		149 mA h g^{-1} (at 0.1 C)	82@80@0.1 C	1 M LiFAP in EC-DMC	3.1–5.6 vs. Li/Li$^+$	[95]
$LiNiPO_4/Co_3O_4$	Core-shell		139 mA h g^{-1} (at 0.1 C)	72@80@0.1 C	1 M LiFAP in EC-DMC	3.1–5.6 vs. Li/Li$^+$	[95]
$LiMnPO_4/C$	Spindle-like		129 mA h g^{-1} (at 1 C)	96@100@1 C	1 M $LiPF_6$ in EC-DEC	2.5–4.5 vs. Li/Li$^+$	[178]
$LiMnPO_4/C$	Nanofibers		162.4 mA h g^{-1} (at 0.2 C)	92@300@0.2 C	1 M $LiPF_6$ in EC-DMC-DEC	2.0–4.5 vs. Li/Li$^+$	[179]

Notes: Cycling stability is expressed as the capacity retention after charging/discharging cycles at a specific rate.

Örnek et al. [170] produced a nanostructured $LiCo_{1-x}Mn_xPO_4/C$ (x = 0 and 0.05) material via combining sol-gel and carbothermal reduction method with carbon coating on the surface and substitution of Co^{2+} with Mn^{2+} in LCP. Due to the combination of nanostructure, carbon coating and manganese doping, $LiCo_{1-x}Mn_xPO_4/C$ as high-voltage cathodes for LIBs showed superior cycle behavior. Jang et al. [171] developed a LFP coated LCP cathode. The discharge capacity of Li/LFP coated LCP cell delivered an initial discharge capacity of 132 mA h g^{-1}, which was higher than that of bare LCP. Moreover, the cycling performance of LFP coated LCP cell was also improved compared with bare LCP. LCP-CNT composites were reported as well, and they were demonstrated reduced resistance and thus enhanced electrochemical properties [172]. In addition, controlling the shape of LCP was also a feasible choice to enhance energy storage properties. For example, Truong et al. [173] synthesized three types of phosphates with different morphologies (e.g., nanorods, Fig. 10j-k, nanoplates, Fig. 10l-m, and NPs Fig. 10n-o) by a one-pot supercritical fluid (SCF) processing. The effect of amine hexamethylenediamine (HMD)/hexamethylenetetramine (HMT) which acted as OH$^-$ source to tune the pH of the reaction solution as well as the growth rate of LCP nanocrystals were studied. When 10 mmol HMD was added, LCP nanoplates formed. Because of unique crystallographic orientation with exposed [010] facets, LCP nanorods and nanoplates showed better electrochemical performance than that of nanoparticles (Fig. 10p-q).

4.2.1.3. LiNiPO4. Among the lithium transition phosphates ($LiMPO_4$, M = Fe, Co, Mn, and Ni), $LiNiPO_4$ (LNP) cathode exhibits the highest redox potential theoretical value (~5.1 V). However, few studies related to LNP have been reported, because it is electrochemically inactive and only a small number of Li$^+$ inside the crystal system [174,175]. Researchers are working to make the potential of LNP accessible in LIB applications. For example, Örnek et al. [176] developed a novel and effective strategy to produce core-shell LNP/C cathode material via a microwave approach using alginic acid as a carbon precursor. The LNP/C electrode showed a high discharge capacity of 150.2 mA h g^{-1} at the 0.1 C rate with a good retention capacity (92%) after 100 cycles and improved cycle capability, which can be ascribed to the combination of nano-scale structure, conductive carbon coating, and well-crystallized molecules. Additionally, Örnek [95] synthesized LNP core and Co_3O_4/CoO shell nanocomposites via hard-template and solvothermal syntheses (Fig. 11a). CoO and Co_3O_4 surface-modification has improved the ionic diffusibility and electronic conductivity of LNP material. As a result, compared with pure LNP, LNP@CoO and LNP@Co_3O_4 samples delivered much higher initial discharge capacity (Fig. 11b) and better cyclicity with a slight capacity decay at a rate of 0.1 C (Fig. 11c).

4.2.1.4. LiMnPO4. Compared with LCP and LNP, $LiMnPO_4$ (LMP) with a maximum energy density of ~700 W h kg^{-1} possesses a relative low operating voltage ~4.1 V vs. Li/L$^+$, which makes the electrochemical window falls within the electrochemical stability window of conventional electrolyte solutions [177]. Aravindan et al. [177] prepared a carbon-coated LMP by a solid-state approach. The half-cell showed good electrochemical performance under different test model which were in good agreement with the previous reports. Nano-spindle-like LMP/C had been papered by Wu et al. [178] via a microwave-heating method in a chloride/ethylene glycol-based deep eutectic solvent. During the process, the eutectic solvent could adjust the oriented growth and morphology of LMP and serve as a crystal-face inhibitor. Compared with LMP/C (E-LMP/) sample (Fig. 11d) synthesized through a conventional heating method and LMP sample without a carbon coating (B-LMP) (Fig. 11e), the resultant LMP/C (Fig. 11f) sample showed better performance giving a discharge capacity of 129 mA h g^{-1} with a capacity retention of 96% after 100 cycles at 1 C, which could be ascribed to the spindle-like structure and a uniform carbon layer. (Fig. 11i-j). From the XRD patterns (Fig. 11g-h), LMP formed by microwave methode. Yang et al. [179] synthesized a 1D LMP@C nanofiber with a 3D mesoporous architecture
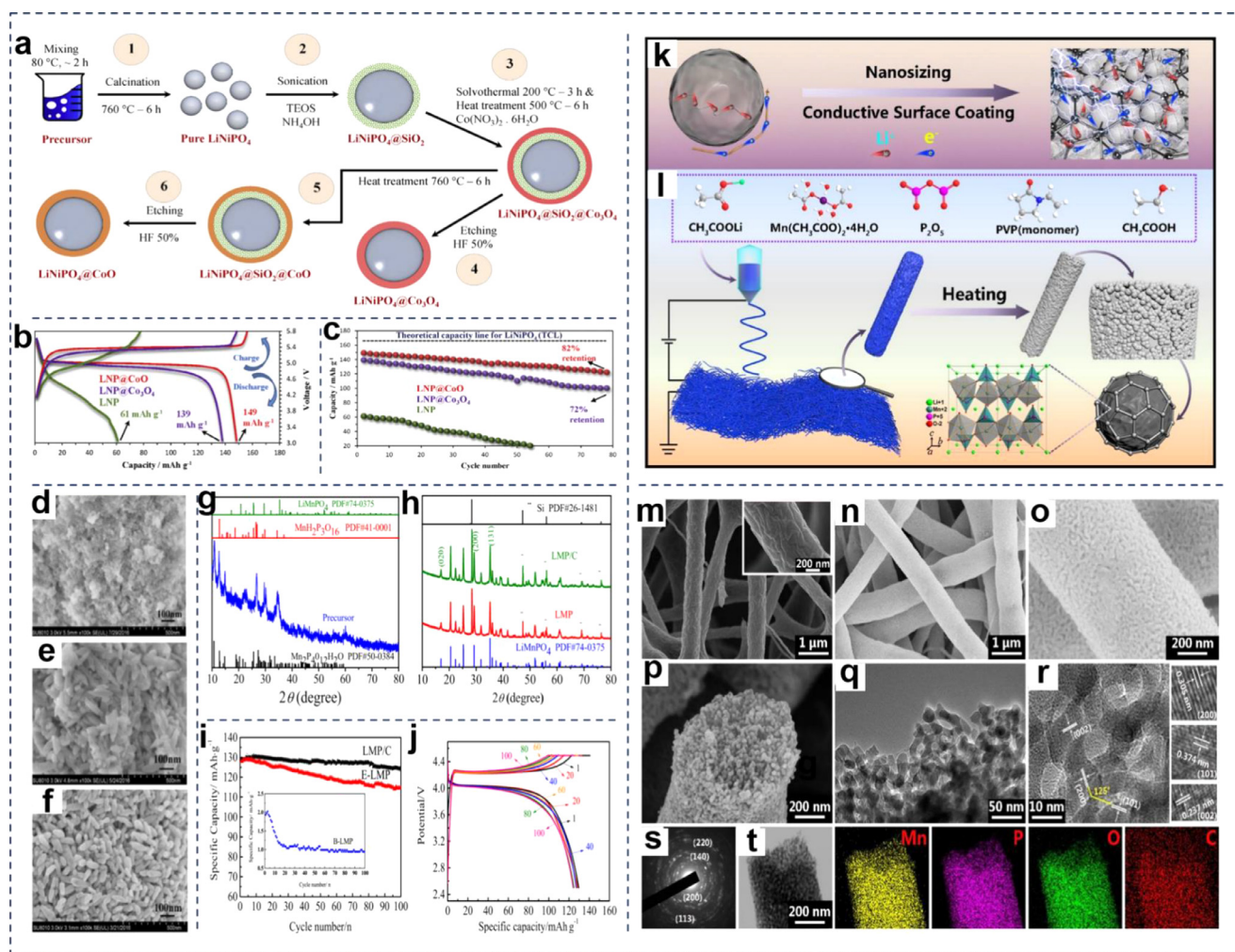
Fig. 11. (a) Schematic drawing of the LNP@CoO and LNP@Co$_3$O$_4$ NPs using stepwise synthesis methodology. (b) Charge-discharge curves of the prepared electrodes at 0.1 C-rate; (c) Cycling stability profiles of the prepared electrodes comparison at 0.1 C-rate. (a-c) Reproduced with permission [95]. Copyright 2017, Elsevier. SEM images of the (d) precursor, (e) LMP, and (f) LMP/C. (g-h) XRD pattern for the precursor, LMP and LMP/C. Electrochemical properties of the prepared samples: (i) Cycle performance at 1 C. (j) Charge-discharge curves of LMP/C at 1 C. (d-j) Reproduced with permission [178]. Copyright 2017, Elsevier. Schematic illustration of structural engineering of LMP: (k) illustration of the improved reaction kinetics of LMP by nanosizing and conductive surface coating, and (l) schematic view of procedure for preparing 1D LMP@C nanofibers with in-situ created 3D mesoporous structure. Micrographs of as-electrospun LMP@C-8 nanofibers before and after heat-treatment at 750 °C: (m) SEM images of precursor fibers with inset of the corresponding partially appearance. (n-p) SEM images of the surface and cross-sectional views of LMP@C-8 nanofibers. (q-r) HR-TEM images, the insets of (r) shows lattice fringes; (s) SAED pattern; (t) TEM-EDS mapping. (k-t) Reproduced with permission [179]. Copyright 2019, Wiley-VCH.

via an electrospinning followed by a simple heat-treatment (Fig. 11k-l). In LMP@C, ultrafine LMP NPs were homogeneously confined in the nanofibers and among the interconnected LMP@C NPs, mesopores were in-situ introduced. Meanwhile, ultrathin carbon layer was coated on the ultrafine LMP NPs. (Fig. 11m-t). This unique structure facilitated the electronic/ionic transportation and alleviaated the pulverization of electrodes. Moreover, hierarchical construction with enlarged surface allowed more active sites to be exposed into the electrolyte and promoted the surface-controlled pseudocapacitive contribution. Hence, LMP@C nanofibers delivered a high reversible capacity (149.8 mA h g^{-1}) with a superior capacity retention (92%) over 300 cycles at 0.2 C. Even at a high rate of 5 C, a capacity of 63.1 mA h g^{-1} retained after 2000 cycles with an exceptional cyclic stability.

From the study of Hautier et al. [7], high voltages are associated with unsafety, compounds (M = Mn, Co and Ni) with high potential having worse thermal stability than that of LFP and showing poor cycling performances at a useful charge/discharge rate. For this range of phosphates, there are limitations that need to be addressed and further studies are worth developing.

4.2.2. NASICON-based phosphates

Among these high-voltage phosphate LMP (~4.1 V *vs.* Li/Li$^+$), LCP (~4.8 V *vs.* Li/Li$^+$), LNP (~5.1 V *vs.* Li/Li$^+$), and LVP (~3.8 V (average) *vs.* Li/Li$^+$), NASICON monoclinic LVP with the highest theoretical capacity (197 mA h g^{-1}) has been identified as electroactive materials for LIB applications due to abundant resources, high safety, and rapid ionic diffusion [35,64]. The explored NASICON nanomaterials and their morphologies and electrochemical performance are summarized in Table 6.

Generally, the bare NASICON LVP still suffers inferior electronic conductivity due to the two separated [VO$_6$] octahedral arrangement, which significantly deteriorates its rate performance [114,180]. To further improve the electrochemical performance of LVP, novel structures with high electronic conductivity with fast lithium diffusion are demanding [181]. Construction of composites which could combine the advantages of various components is a widely used strategy. Among those composites, combination of the LVP particle with carbon typically like carbon coating, is the most common way to enhance its electronic conductivity [182]. For example, Zhang et al. [181] prepared carbon-coated LVP NPs encapsulated in a carbon matrix (Fig. 12a-d) us-
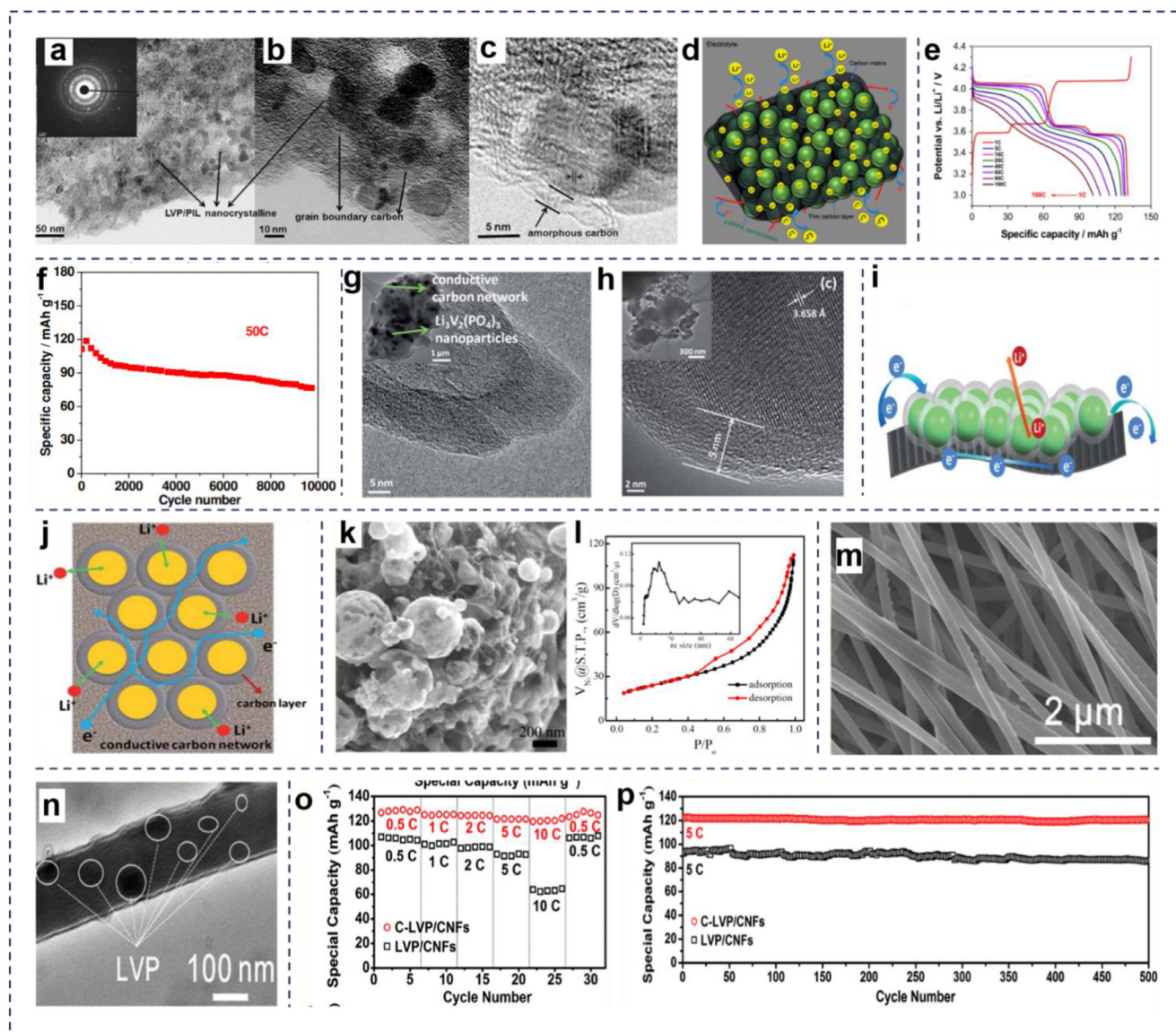
Fig. 12. (a-b) TEM images, and (c) HRTEM image of LVP/PIL; (d) Schematic representation of the structure of LVP/PIL, illustrating the Li⁺ and electron pathways; (e) Specific discharge capacity and typical potential profiles of LVP/PIL electrodes when discharged at various current densities in the range of 1 to 100 C with a constant charging rate of 0.1 C; (f) Specific capacity of LVP/PIL electrodes during long-term cycling at 50 C. (a-f) Reproduced with permission [181]. Copyright 2015, Elsevier. Typical HRTEM images of (g) S0 and (h) S20; (i-j) Schematic illustration of LVP nanospheres with a carbon coating layer and continuous carbon network. (g-j) Reproduced with permission [183]. Copyright 2013, The Royal Society of Chemistry. (k) LVP/CNT composite, showing that CNTs interpenetrated into LVP; (l) Nitrogen-sorption isotherms and pore size distribution (inset) of the LVP/CNT composite particles. (k, l) Reproduced with permission [184]. Copyright 2018, American Chemical Society. (m) SEM images of C-LVP/CNFs, and (n) TEM images of C-LVP/CNFs; (o) Rate performance of C-LVP/CNFs and LVP/CNFs; (p) Long-term cycling performance of LVP/CNFs and C-LVP/CNFs at 5 C. (m-p) Reproduced with permission [108]. Copyright 2016, The Royal Society of Chemistry.

ing a protic ionic liquid (pIL) as soft template and carbon source. Due to the carbon layer coated on the surface, the electronic conductivity of LVP pellets increased from 10^{-6} to 10^{-2} S cm^{-1}. In addition, porous carbon matrix, reduced particle size and relatively high surface area of the material contributed to the intimate contact between electrolyte and LVP particles, consequently leading to high specific capacities (100 mA h g^{-1} at 100 C in the potential range of 3.0 to 4.3 V and 120 mA h g^{-1} at 50 C in the potential range of 3.0 to 4.8 V) and excellent cycling stability (70% retention after 10,000 cycles at 50 C) of cathodes (Fig. 12e-f). Mai et al. [183] also designed a similar LVP structure. As shown in Fig. 12g-i, carbon-coated LVP nanospheres piled together on carbon network. The carbon network derived from acetylene black provided a facile and continuous pathway for electron transport and the carbon layer developed from PEG calcination mitigated the structural

degradation during lithium diffusion. For comparison, different ratios of PEG (labeled as S10, S20, and S30 for 10, 20, and 30 wt.% of total mass, respectively) had been studied and S20 exhibited the best performance that when tested at 30 C, the capacity could reach up to 87 mA h g^{-1}, and after 5000 cycles at 5 C, the capacity could still maintain at 79 mA h g^{-1}. Intertwined with CNTs nest, bulk LVP cathode with improved rate performance had been built by Zhu et al. [184] via aerosol-assisted spray process followed with a high-temperature calcination. As shown in Fig. 12k-l, long-range conductive network for Li⁺ and electron transport pathway with mesopores were generated due to the interlaced CNTs nest. As a result, binder-free, thick electrodes (with thickness of 160 μm) constructed by those microspheres and CNTs showed comparable rate performance to that of 30 μm before the rate of 10 C, reaching 98% and 92% of theoretical capacity of LVP at 10 C,

Table 6
Performances of recently reported LIBs based on NASICON phosphates with corresponding morphologies.

Materials	Morphology	Capacitance	Capacity retention [%]	Electrolytes	Voltage, V	Ref.
$Li_3V_2(PO_4)_3/C$	Carbon-coated nanoparticles embedded in carbon	100 mA h g^{-1} (at 100 C)	70@10000@50 C	1 M LiPF$_6$ in EC-DMC	3.0-4.3 vs. Li/Li$^+$	[181]
$Li_3V_2(PO_4)_3/C$	Carbon-coated nanospheres	87 mA h g^{-1} (at 30 C)	83@1000@5 C	1 M LiPF$_6$ in EC-DEC	3.0-4.5 vs. Li/Li$^+$	[183]
$Li_3V_2(PO_4)_3/CNT$	Nanoparticles intertwined with CNTs	130 mA h g^{-1} (at 10 C)	96@1000@20 C	1 M LiPF$_6$ in EC-DMC	3.0-4.3 vs. Li/Li$^+$	[184]
$Li_3V_2(PO_4)_3/C$	Nanofiber	120 mA h g^{-1} (at 10 C)	98.9@500@5 C	1 M LiPF$_6$ in EC-DMC	3.0-4.3 vs. Li/Li$^+$	[108]
$Li_3V_2(PO_4)_3/C$	Nanofibers	191 mA h g^{-1} (at 0.1 C)	94.5@120@20 C	1 M LiPF$_6$ in EC-DMC	3.0-4.8 vs. Li/Li$^+$	[114]
$Li_3V_2(PO_4)_3/N-C$	Nitrogen-doped carbon-modified nanofibers	135.6 mA h g^{-1} (at 20 C)	95.3@400@20 C	-	3.0-4.8 vs. Li/Li$^+$	[186]
$Li_3V_2(PO_4)_3/C@N-GR$	Nanoparticles anchored on the nitrogen-doped graphene nanosheets	191.5 mA h g^{-1} (at 0.1 C)	87.3@1000@20 C	1 M LiPF$_6$ in EC-DMC-EMC	3.0-4.8 vs. Li/Li$^+$	[85]
$Li_3V_2(PO_4)_3/C$	Carbon-coated 3D ordered macropores	151 mA h g^{-1} (at 0.1 C)	99.92@60@0.1 C	1 M LiPF$_6$ in EC-DMC	3.0-4.4 vs. Li/Li$^+$	[187]
$Li_3V_2(PO_4)_{2.88}F_{0.12}@C$	Carbon-coated nanoparticles	123.16 mA h g^{-1} (at 2 C)	97.1@100@1 C	1 M LiPF$_6$ in EC-DEC-DMC	3.0-4.3 vs. Li/Li$^+$	[188]
$Li_{2.6}Na_{0.4}V_2(PO_4)_3/C$	Nanoparticles	121.6 mA h g^{-1} (at 5 C)	85.9@1000@5 C	1 M LiPF$_6$ in EC-DMC-EMC	3.0-4.3 vs. Li/Li$^+$	[189]
$Li_3V_{1.97}Zn_{0.05}(PO_4)_3/C$	Nanoparticles	109 mA h g^{-1} (at 1 C)	98@1000@1 C	1 M LiPF$_6$ in EC-DMC-DEC	3.0-4.3 vs. Li/Li$^+$	[190]
$Li_3V_{1.95}Fe_{0.05}(PO_4)_3/C-Si$	C+SiO$_2$-coated nanoparticles	170.8 mA h g^{-1} (at 1 C)	82.3@100@5 C	1 M LiPF$_6$ in EC-DMC	3.0-4.8 vs. Li/Li$^+$	[191]
$LiTi_2(PO_4)_3/C$	Carbon-coated nanoparticles	104 mA h g^{-1} (at 0.72 C)	91@50@0.72 C	1 M LiPF$_6$ in EC-DMC	2.0-3.4 vs. Li/Li$^+$	[192]

Notes: Cycling stability is expressed as the capacity retention after charging/discharging cycles at a specific rate.

respectively. A combination of structure modification and carbon compositing is one of the most effective strategies to improve the electrochemical performances of LVP [185]. For example, Sun et al. [108] have prepared carbon fibers with carbon-coated LVP particles (C-LVP/CNFs) imbedded in. As shown in Fig. 12m-n, LVP particles were uniformly distributed among the CNFs. Compared to the samples without carbon outer-layer (LVP/CNFs), C-LVP/CNFs showed much better electrochemical performances with high rate capability (120 mA h g^{-1} at 10 C) and capacity retention over cycling (98.9% capacity retention after 500 cycles at 5 C) (Fig. 12o-p). Another example is the work by Wei et al. [114] who fabricated 1D highly porous LVP/C nanofibers (p-LVP/C) via electrospinning process followed two-step heat treatment (calcined at 350°C for 1 h in air and then treated at 800°C for 10 h in Ar/H$_2$). Heat treatment helped to reduce the diameter of the obtained LVP/C fibers (Fig. 13a-b) and generate porous structure (Fig. 13c-d), and thus, shortened the transport distance for both electron and Li$^+$. Because of the porous structure, the electrochemical performance of LVP material was further enhanced when compared with LVP/C fibers which was also prepared through the same method without calcining at 350°C in air for 1 h (Fig. 13e-f). For further improving electronic conductivity, nitrogen-doped carbon-modified LVP (NC/LVP) fibers with mesoporous nanostructure was reported by Cao et al. [186]. Polyacrylonitrile was used as the carbon and nitrogen sources. Transmission electron microscopy (TEM) image showed that NC/LVP NPs (10-25 nm) piled together forming 1D nanofibers (diameter of 90-180 nm) where mesopores were generated (Fig. 13g-j), which significantly reduced the diffusion length of Li$^+$ and significantly improved the conductivity of LVP. As a result, the composite exhibited a capacity of 129.2 mA h g^{-1} over 400 cycles at 20 C. Graphene, a monolayer of sp^2 bonded carbon atoms arranged in six-membered rings, has become one of the most exciting topics of research. Incorporation of graphene with electrode materials can efficiently improve the performance. For example, Cui et al. [85] reported a nitrogen-doped graphene (N-G) NS-decorated LVP/C (N-G-LVP/C) composite via a microwave-assisted hydrothermal method (Fig. 13k). LVP/C NPs were anchored on the N-G, forming a conductive network structure in the composite. For comparison, the electrochemical properties of LVP/C, G-LVP/C and N-GLVP/C samples were tested (Fig. 13l-o). G-LVP/C and N-G-LVP/C exhibited better cycle stability and higher discharge capacity due to the conducting graphene NSs which could contact tightly with the LVP particles and acted as electronic conducting skeleton for the electrode. By comparison, the electrochemical property of G-LVP/C was improved after N doping in graphene, which could be attributed to the improvement in electronic conductivity arising from conductive N-G to a current collector. As a result, N-G-LVP/C nanocomposites as cathode material exhibited a specific discharge capacity of 191.5, 172.6, and 160.5 mA h g^{-1} at 0.1,5, and 10 C, respectively, within a voltage range of 3.0-4.8 V. Moreover, it showed a stable cycling performance with 87.3% capacity retention after 1000 cycles at 20 C. Due to strong anisotropy of Li$^+$ diffusion in monoclinic LVP crystal, Li$^+$ mobility showed a 1D diffusion path, where the Li$^+$ diffusion was more limited with the presence of immobile or low mobile defects resided in the diffusion path compared to 2D or higher dimensional diffusion. Li et al. [187] developed 3D ordered microporous LVP/C nanocomposite cathode for LIBs. As shown in Fig. 13p, LVP precursor solution was filled in nanoscale voids of ordered polymethylmethacrylate (PMMA) CCA template. After calcination of LVP/C, 3D ordered nanopores with a diameter of no larger than 140 nm and wall thickness of approximately 10-80 nm coated with an amorphous carbon were obtained (Fig. 13q-r). Benefiting from the well-defined active nanocrystals and controlled nanoscale pores, the channels through which the liquid electrolyte diffused into micrometer sized particles were generated, and thus providing direct access and reservoirs for electrolyte impregnating into LVP particles as well as large interface area between the electrode. As a result, the LVP/C nanocomposite delivered a stable and highly reversible discharge capacity (151 mA h g^{-1} at 0.1 C) and high rate capability (132 mA h g^{-1} at 5 C) in a voltage range of 3.0-4.4 V.
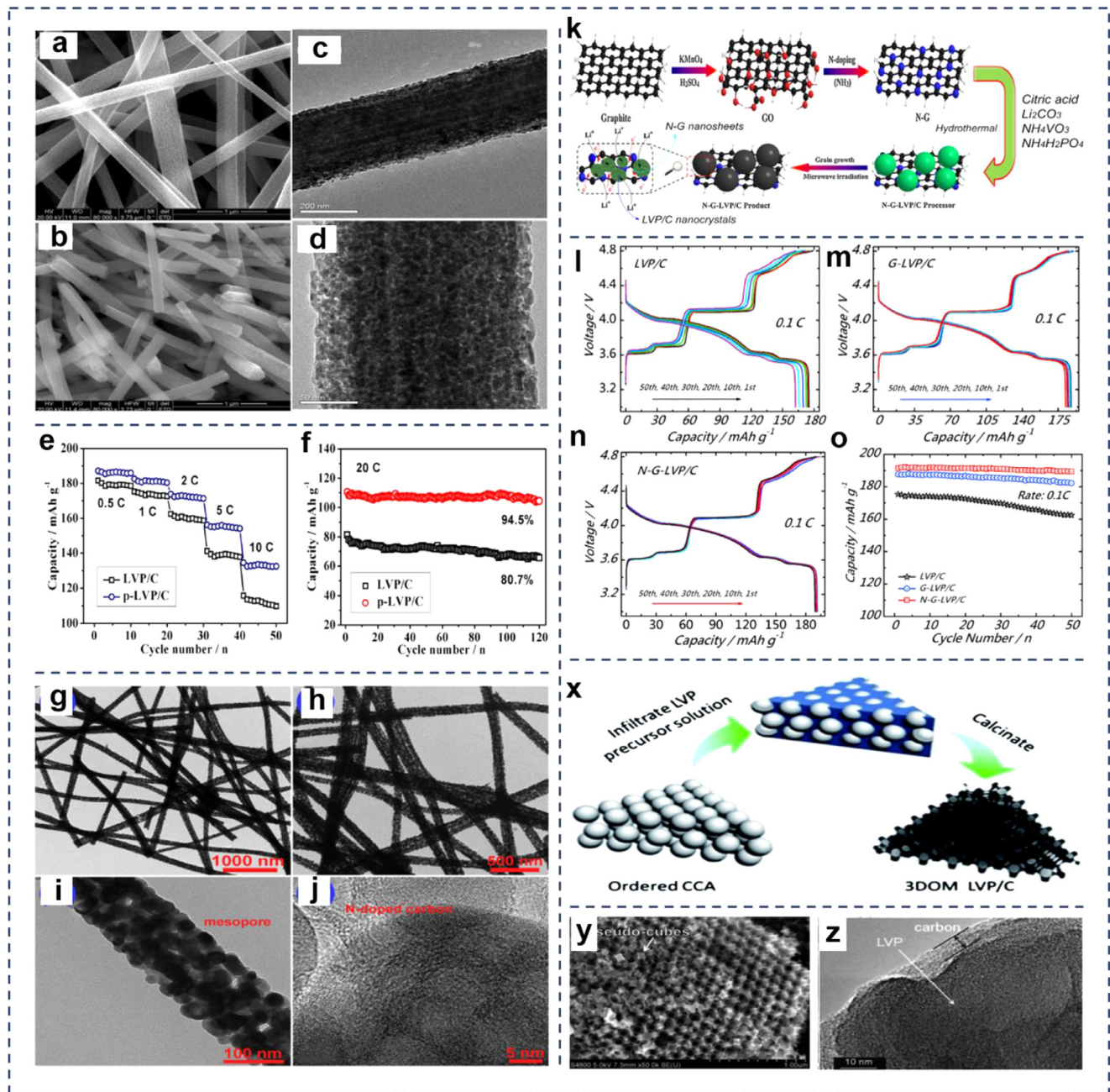
Fig. 13. (a) SEM images of LVP/C, and (b) p-LVP/C powders; (c) TEM images of the obtained LVP/C, and (d) p-LVP/C samples; (e) Capacity retentions of the obtained LVP/C and p-LVP/C at different current rates between 3.0 and 4.8 V (*vs.* Li/Li$^+$); (f) Long cycle-life performance of the electrodes at high rate of 20 C for 120 cycles. (a-f) Reproduced with permission [114]. Copyright 2017, Elsevier. (g-j) Nanostructures for the fabricated NC/LVP fibers. (g-j) Reproduced with permission [186]. Copyright 2019, Elsevier. (k) The detailed fabrication process, and electron conduction and Li-ion transport of N-G-LVP/C electrode; (l) LVP/C, (m) G-LVP/C and (n) N-G-LVP/C electrodes at a low rate of 0.1 C in the voltage range of 3.0-4.8 V (*vs.* Li/Li$^+$); (o) The resulting cycling data versus capacity for the sample. (k-o) Reproduced with permission [85]. Copyright 2016, Elsevier. (p) Schematic diagram illustrating the processing steps to produce 3DOM LVP/C materials; (q) Electron microscopy images, and (r) HRTEM image of macroporous LVP/C samples calcined at 750°C. (p-r) Reproduced with permission [187]. Copyright 2014, The Royal Society of Chemistry.

Doping is always an effective way to improve the rate capability or cycling performance in electrode materials with the phosphate framework. Wu et al. [188] synthesized fluorine-doped LVP@C ($Li_3V_2(PO_4)_{3-x}F_x$@C) via chemical polymerization combined with low-temperature solid-state approach. By combining experiment result and DFT theoretical calculation, the F-doping effect on the electrochemical behaviors of LVP was investigated that F-doping greatly facilitated the charge transfer rate of Li$^+$ inserting/exacting process for better reversibility and enhanced Li$^+$ diffusion rate to access the reaction sites,

thus resulting in high-rate capacity and cycling stability. To study the impact of doping concentration, samples with different fluorine contents were tested. The optimal $Li_3V_2(PO4)_{2.88}F_{0.12}$@C delivered 123.16 mA h g^{-1} at 2 C and showed greatly improved cycling stability. In addition, Zuo et al. [189] developed a Na doping technology for LVP. They synthesized a micro-sized $Li_{3-x}Na_xV_2(PO_4)_3$/C composite by sol-gel method. In this structure, rhombohedral phase which could provide a larger free volume of the interstitial space offered an excellent high-rate capability and Na doping which could stabilize the rhom-

bohedral structure of the LVP framework led to the remarkable cycling stability. As a result, $Li_{2.6}Na_{0.4}V_2(PO_4)_3/C$ showed a high energy density (478.8 W h kg^{-1}), high rate capacity, and excellent cycling performance. Wang et al. [190] designed a Zn-doped LVP composited with carbon ($Li_3V_{1.97}Zn_{0.05}(PO_4)_3/C$). The estimated Ragone plot showed that this composite could meet both requirements of energy density and power density for plug-in hybrid electric vehicles. Moreover, $Li_3V_{1.97}Zn_{0.05}(PO_4)_3/C$ displayed 100% of its initial discharge capacities (109 mA h g^{-1}) among the 1000 cycles when cycled at 20 C charge rates and 1 C discharge rates, showing good cyclability. Fe-doping and C/SiO_2 hybrid layer coating on LVP cathode material have been synthesized via an ultrasonic-assisted solid-state method. This material was also demonstrated with improved electrochemical performance by Sun et al. [191] NASICON-type $LiTi_2(PO_4)_3$ (LTP) was an ideal host matrix for reversible insertion of Li as well. For example, Aravindan et al. [192] developed a carbon-coated LTP as a promising insertion host for LIBs and SIBs. When tested in half-cell Li/C-LTP, C-LTP delivered 104 mA h g^{-1} at 0.72 C, and retained approximately 91% of the initial discharge capacity after 50 galvanostatic charge/discharge cycles.

4.2.3. Tavorite AM(PO$_4$)Y

Up to now, there have been several types of fluoro-phosphates reported for LIBs in the literature. Reported by Masquelier et al. [14], the structural types of fluoro-phosphates could be described as A_2MPO_4F (A^+ = Li$^+$, Na$^+$, and H$^+$; M = Fe, V, Nb, Ti, Co, and Mn), which are considered as promising materials in LIB cathode applications because their theoretical capacity (if two alkali cations can be extracted) is twice as large as that of olivine-type $LiMPO_4$ compounds. Benefiting from the effects of both phosphate group and F anions which lower the energy of a given $M^{(n+1)+}/M^{n+}$ redox couple, tavorite-type fluoro-phosphates are expected to exhibit high rate capability as promising candidates for LIBs [14]. For example, Ellis et al. [49] reported a sodium/lithium iron phosphate, A_2FePO_4F (A = Na and Li), that could serve as a cathode in either LIBs or SIBs. This new iron phosphate exhibited facile 2D ion conduction paths for Li$^+$ transport and its unusual solid-solution-like electrochemical behavior could be correlated with structural properties: isostructural end members/intermediates and a low-strain volume change during reduction-oxidation process. For these reasons, this free-standing sodium iron phosphate cathode in a LIBs offered significant advantages with respect to the cost and lithium availability and showed great potentials for SIB applications as well. Similarly, Nicolas et al. [43] developed a non-aqueous fluorolytic sol-gel chemistry route to synthesize polyanionic fluorine-containing materials at low temperature. The obtained $LiFePO_4F$ material showed an excellent cycling stability (115 mA h g^{-1} after 100 cycles at C/2 rate). Similar with LVP, tavorite-structured compound $LiVPO_4F$ and $LiVPO_4O$ are of great potential as cathodes for LIBs. However, in $LiVPO_4F$, the redox potential of V^{2+}/V^{3+} (~1.8 V vs. Li/Li$^+$) is too low to be exploited as a cathode and $LiVPO_4O$ suffers poor electrochemical activity and poor cycle capacity retention. To solve these issues, Kim et al. [42] synthesized a $LiVPO_4O_{0.75}F_{0.25}$ by single-step solid-state reaction. As-prepared $LiVPO_4O_{0.75}F_{0.25}$ possessed higher average operating voltage and better electrochemical activity than $LiVPO_4O$ and showed higher operating voltage (~2.4 V) than $LiVPO_4F$ (~1.8 V). As a result, $LiVPO_4O_{0.75}F_{0.25}$ achieved high specific capacity (260 mA h g^{-1}) in the voltage range from 2.0-4.8 V and thereby delivered high energy density (820 W h kg^{-1}). In order to optimize the synthesis method, Erwan et al. [47] developed a spark plasma sintering (SPS) way to synthesize Li_2CoPO_4F electrode materials for LIBs. During the whole experiment, the rapid heating rate caused by pulse current and the restriction of particle growth caused by uniaxial pressure greatly shortened the reaction time and reduced the particle size, respectively. And the properties of Li_2CoPO_4F prepared by traditional solid-state routes and obtained by SPS method were tested and compared. The results demonstrated that the material obtained by SPS showed comparable electrochemical properties to the same materials obtained after hours by classical solid-state routes, which demonstrated the SPS approach could replace conventional ceramic routes particularly for small particle size with a drastic decrease of reaction time (from 78 h to 9 min for Li_2CoPO_4F).

4.2.4. Other types bimetallic phosphates

Metallic analogues of $LiMPO_4$ (M = Fe, Ni, and Mn), like $Ag_2VO_2PO_4$ have attracted extensive attention due to the multiple electron transfer and the in-situ formation of Ag NPs based on Li$^+$ insertion accompanied by discrete redox reactions at the two transition metal centers. Patridge et al. [24] demonstrated that $Ag_2VO_2PO_4$ showed an *in situ* conductivity enhancement upon discharge, resulting in inherently high-power capability. The *in-situ* generated Ag NPs served as a conductive matrix which ensured intimate electrical contact for a majority of the electrode material and avoided many processing problems that aroused by using composite/coated materials. In addition, compared with NASICON structure, the inductive effect of PO_4^{n-} polyanion generated in $VOPO_4$ is weaker because of each MO_6 octahedron only connected to four XO_4 tetrahedra (instead of 6 for the NASICON structure). Generally, there are two main types of $VOPO_4$, noted as α and β [14]. When Li$^+$ were inserted into $VOPO_4$ structure, $LiVOPO_4$ will be formed. Compared to LFP, The $VOPO_4$ compound showed a higher discharge potential flat of approximately 4 V (0.5 V higher than LFP) with high electronic conductivity, attaining higher power densities [6]. Zheng et al. [193] reported $LiVOPO_4@V_2O_5$ core-shell nanospheres as cathode materials for LIBs. Combining the advantages of β-$LiVOPO_4$ (higher potential of about 4.0 V) and V_2O_5 (high electrical conductivity), $LiVOPO_4@V_2O_5$ where an orthorhombic $LiVOPO_4$ as a core with an *in situ* formed V_2O_5 shell showed high rate capability and long cycle life. In addition, ε-$VOPO_4$ and α-$LiVOPO_4$ were also demonstrated to be appealing electrode materials by Kerr et al. [82]. Electrochemical tests showed that after the first reduction process, $VOPO_4$ was transformed to the α-$LiVOPO_4$ phase where the Li$^+$ in loosely bound five-coordinate sites allowing for facile ion conduction. Stable capacity behavior was achieved for the chemically lithiated α-$LiVOPO_4$ polymorph after enhancement of the particle/CB contact by mechanical grinding.

4.3. Multi-metal phosphates

Multi-transition-metal phosphate can efficiently increase the electronic and ionic conductivities, and have been studied intensively in recent years for LIBs, as summarized in Table 7.

Zou et al. [194] prepared a $LiFe_{0.2}Mn_{0.8}PO_4$ cathode material by solid-state reaction combined with a ball-milling with CB and sucrose as carbon sources. Under the optimal condition (calcination at 550 °C for 3 h using both CB and sucrose precursor with a ratio of 5:5 and total carbon content of 20 wt.% and ball-milling for 5 h.), the as-prepared $LiFe_{0.2}Mn_{0.8}PO_4$ delivered a capacity of 150 mA h g^{-1} at 1/20 C and 110 mA h g^{-1} at 1 C. Carbon coated $LiFe_{0.2}Mn_{0.8}PO_4$ maintained 91% of its initial capacity after 500 cycles.

Kim et al. [103] successfully fabricated a Mn-rich olivine $LiFe_{0.3}Mn_{0.7}PO_4$ which encapsulated in a conductive glassy lithium fluorophosphate ($LiFe_{0.3}Mn_{0.7}PO_4$-GLFP) through simple non-stoichiometric synthesis. The coating of the glassy lithium fluorophosphate nanolayer could significantly decrease the charge-transfer resistance of $LiFe_{0.3}Mn_{0.7}PO_4$ and improve Li$^+$ diffusion. As a result, $LiFe_{0.3}Mn_{0.7}PO_4$-GLFP achieved much higher power capability (~130 mA h g^{-1} at 10 C) than that of the pristine ($LiFe_{0.3}Mn_{0.7}PO_4$) counterpart and great cyclability (~75% retention of its initial capacity over 500 cycles at 1 C). Srout et al. [195] synthesized a NASICON structured $Li_{1.5}Fe_{0.5}Ti_{1.5}(PO_4)_3$ phosphate material by sol-gel method. These $Li_{1.5}Fe_{0.5}Ti_{1.5}(PO_4)_3$ particles were coated with a conductive carbon layer. Binder CMC delivered better electrochemical performance compared with binder PVDF in electrochemical tests. As-prepared phosphate delivered a specific capacity of 141 mA h g^{-1} and 567 mA h g^{-1}, at the rate of C/10 within the voltage windows 1.5-3.0 V and 0.5-3.0 V vs. Li/Li$^+$, respectively. $LiCo_{0.5}Mn_{0.5}PO_4$/CNT nanocomposites which

Table 7

Performances of recently reported LIBs based on multi-metal phosphates with corresponding morphologies.

Materials	Morphology	Capacitance	Capacity retention [%]	Electrolytes	Voltage, V	Ref.
$LiFe_{0.2}Mn_{0.8}PO_4$	Carbon-coated nanoparticles	110 mA h g^{-1} (at 1C)	91@500@0.2 C	1 M LiPF$_6$ in EC-DMC-EMC	2.0–4.5 vs. Li/Li$^+$	[194]
$LiFe_{0.3}Mn_{0.7}PO_4$-GLFP	$LiFe_{0.3}Mn_{0.7}PO_4$ encapsulated by glassy lithium fluorophosphate	130 mA h g^{-1} (at 10C)	75@500@1 C	1 M LiPF$_6$ in EC-DMC	2.0–4.7 vs. Li/Li$^+$	[103]
$Li_{1.5}Fe_{0.5}Ti_{1.5}(PO_4)_3$/C	Carbon-coated $Li_{1.5}Fe_{0.5}Ti_{1.5}(PO_4)_3$ particles	567 mA h g^{-1} (at C/10)	73@100@C/2	1 M LiPF$_6$ in EC-DMC	0.5–3.0 vs. Li/Li$^+$	[195]
$LiCo_{0.5}Mn_{0.5}PO_4$/CNT	$LiCo_{0.5}Mn_{0.5}PO_4$ nanoparticles interconnected by CNT	151 mA h g^{-1} (at 0.05C)	92@30@01 C	1 M LiPF$_6$ in EC-DMC	2.8–5.0 vs. Li/Li$^+$	[61]
$LiFe_{1/3}Mn_{1/3}Co_{1/3}PO_4$/C	Core-shell	160 mA h g^{-1} (at 0.1 C)	89@30@0.1 C	1 M LiPF$_6$ in EC-DEC (3:7)	2.5–5.0 vs. Li/Li$^+$	[63]
$Li_{2.5}Na_{0.5}V_2(PO_4)_3$	Porous nanoparticle	228.1 mA h g^{-1} (at 0.1 C)	73@500@10 C	1 M LiPF$_6$ in EC-DMC-EMC	1.5–4.3 vs. Li/Li$^+$	[65]
$LiMn_{0.75}Fe_{0.25}PO_4$/rGO	Microspheres	161 mA h g^{-1} (at 0.05 C)	93@1000@10 C	1 M LiPF$_6$ in EC-EMC-DEC	2.0–4.5 vs. Li/Li$^+$	[196]
$LiMn_yFe_{1-y}PO_4$	-	132 mA h g^{-1} (at C/20)	89@450@C/2	1.2 M LiPF$_6$ in EC-EMC-VC (2 wt.%)	2.0–4.25 vs. Li/Li$^+$	[62]
$Na_2Mn_{1.5}Fe_{1.5}(PO_4)_3$	Dandelion	48 mA h g^{-1} (at C/5)	99@50@C/5	1 M LiPF$_6$ in EC-DMC	1.5–4.5 vs. Li/Li$^+$	[86]
$Ca_{0.15}Mg_{0.35}Ti_2(PO_4)_3$	Nanoparticles	138 mA h g^{-1} (at C/20)	83@20@C/20	1 M LiPF$_6$ in EC-DEC	-	[198]

Notes: Cycling stability is expressed as the capacity retention after charging/discharging cycles at a specific rate.

were composed of uniform $LiCo_{0.5}Mn_{0.5}PO_4$ NPs intimately interconnected by CNT networks were reported by Ni et al. [61] Benefiting from CNT conductive networks, $LiCo_{0.5}Mn_{0.5}PO_4$-CNT composite showed enhanced electrochemical performance compared with bared $LiCo_{0.5}Mn_{0.5}PO_4$ and exhibited a high capacity up to 151 mA h g^{-1} and an energy density of 620 mW h g^{-1} with 92% capacity retention after 30 charge/discharge cycles. Core-shell $LiFe_{1/3}Mn_{1/3}Co_{1/3}PO_4$/C nanocomposites obtained from different carbon sources were synthesized by Li et al. [63] via microwave heating route. They prepared three composites (*i.e.*, BP2000 CB coated $LiFe_{1/3}Mn_{1/3}Co_{1/3}PO_4$/BP, acetylene black coated $LiFe_{1/3}Mn_{1/3}Co_{1/3}PO_4$/AB and super P coated $LiFe_{1/3}Mn_{1/3}Co_{1/3}PO_4$/SP), and among them, $LiFe_{1/3}Mn_{1/3}Co_{1/3}PO_4$/BP composite delivered better electrochemical performance showing high discharge capacity (160 mA h g^{-1} at 0.1 C), excellent cyclic stability (143 mA h g^{-1} at 0.1 C after 30 cycles), and rate capability (76 mA h g^{-1} at 20 C). This could be ascribed to lower resistances and faster electronic and ionic diffusion. Isomeric $Li_{2.5}Na_{0.5}V_2(PO_4)_3$ [65], rGO-modifed $LiMn_{0.75}Fe_{0.25}PO_4$ [196], and SiF_4-treated $LiMn_{0.80}Fe_{0.20}PO_4$/C [62] were also demonstrated the high conductivity and stable cyclicity. Some uncommon phosphates (such as lithium difluoro(bisoxalato)phosphate (LiDFBP) [197], sodium manganese-iron phosphate $Na_2Mn_{1.5}Fe_{1.5}(PO_4)_3$ (NMFP) [86], and $Ca_{0.15}Mg_{0.35}Ti_2(PO_4)_3$ [198]) have been reported used for electrode material in LIBs as well.

5. Other metal-ion batteries

Phosphates are not only widely used in LIBs, but also used in other metal-ion batteries such as SIBs [19], CIBs [199], KIBs [36], and mg-ion batteries [200]. The LIBs dominated in the energy-storage systems at present. However, LIBs still face challenges related to the limited resource and high cost of lithium, leading to extensive research on the exploration of novel batteries as alternatives of LIBs.

5.1. Na-ion batteries

Because of the abundant sodium sources, relatively low cost, easily recycling, and the higher potential value of the Na/Na$^+$ than that of Li/Li$^+$ [35], SIBs are considered as the best candidate for power sources with significant benefits to the environment. Especially, SIBs exhibit similar chemistry to that of LIBs and are promising next-generation al-

ternatives. In general, recent studies of phosphates and their composites for SIBs followed similar research strategies used in LIBs as discussed above and are summarized in Table 8.

NASICON-type phosphates which exhibit high Na$^+$ conductivity, stable 3D framework, and long term cycle life as well as high-rate capability were widely explored [12,19]. With increasing attention on phosphates, different phases of phosphates have been developed, including $FePO_4$ [201], $NaTi_2(PO_4)_3$ [202,203], $Na_3V_2(PO_4)_3$ [204], $NaMo_2(PO_4)_3$ [205], $Na_{0.71}Fe_{1.07}PO_4$ [206], $Na_2VTi(PO_4)_3$ [32,38], $Na_3MnZr(PO_4)_3$ [39], $NaNb_{0.05}Ti_{1.95}(PO_4)_3$ [33], Na_2FePO_4F [87,207], and $Na_{1.1}Li_{2.0}V_2(PO_4)_3$ [208]. As presented in Table 8, the capacity and cyclability of Ti and V-based NASICON materials could be considerably improved by carbon coating [192,209], doping [33,210] and morphology modification [211,212]. In addition, for better electrochemical performance, considerable efforts have been made on designing different types of SIBs. Taking advantage of the voltage differences between distinct redox couples in NASICON-structured phosphates, symmetric SIBs had been developed. For example, by exploiting the distinct redox couples between V^{3+}/V^{4+} and Ti^{4+}/Ti^{3+}, Wang et al. [32] assembled symmetric full cell using $Na_2VTi(PO_4)_3$ as both cathode and anode. The $Na_2VTi(PO_4)_3$ was synthesized by a facile sol-gel method, showing a stable specific capacity (147 mA h g^{-1} at 0.1 C). The full cell achieved high capacities at a high rate of 20 C and ultralong lifespan over 10,000 cycles. Similarly, Voronina et al. [33] demonstrated the application of $Na_{2.9}Nb_{0.05}Ti_{1.95}(PO_4)_3$-C in a symmetric cell. This carbon-coated $Na_{2.9}Nb_{0.05}Ti_{1.95}(PO_4)_3$-based symmetric cell exhibited zero-strain characteristics because of the inversed volume changes of the cathode and anode during charge/discharge, resulting in excellent cycling performance (105 mA h g^{-1} after 100 cycles at 0.2 C, 83% capacity retention) and high flexibility in practical application. In such a structure, energy storage was based on the insert/extract from host structure via a biphasic redox mechanism involving the Ti^{4+}/Ti^{3+} redox couple at 2.1 V *vs.* Na/Na$^+$ and a Ti^{3+}/Ti^{2+} redox pair at 0.4 V *vs.* Na/Na$^+$. Compared with bare $NaTi_2(PO_4)_3$, the thin layer of carbon and Nb^{5+} doping in carbon-coated $Na_{2.9}Nb_{0.05}Ti_{1.95}(PO_4)_3$ could efficiently increase the electrical conductivity in both the bulk and surface, leading to excellent structural stability and outstanding rate capability. Specifically, Nb^{5+} doping did not show negative effects on the phase transition in the $NaTi_2(PO_4)_3$ structure but improved the Na$^+$ reaction kinetics compared with that of undoped $NaTi_2(PO_4)_3$. Similarly, Al-doped NASICON-type $Na_3V_{2-x}Al_x(PO_4)_3$/C [213], Mn-doped $Na_3V_{1.7}Mn_{0.3}(PO_4)_3$/C [106],

Table 8

Performances of recently reported SIBs based on phosphates with corresponding morphologies.

Material	Morphology	Capacity [mA h g^{-1}]	Capacity retention[%]	Electrolytes	Voltage, V	Ref.
Amorphous FePO$_4$-C	Nanoparticles wired by single-wall carbon nanotubes	120 (at 0.1 C)	-	1 M NaClO$_4$	2–3.5	[201]
NaTi$_2$(PO$_4$)$_3$/C	NASICON-structured nanoparticles	101 (at 5 C)	94@100	1 M Na$_2$SO$_4$ in EC-DMC	−1.2–0.2 vs. Ag/AgCl	[202]
Na$_2$VTi(PO$_4$)$_3$@C	NASICON-structured	147 (at 0.1 C)	77@500@10 C	1 M NaClO$_4$ in EC-PC	1.5–4.5 vs. Na/Na$^+$	[32]
Na$_3$MnZr(PO$_4$)$_3$	NASICON-structured particles coated with a thin carbon layer	105 (at 0.1C)	91@500@0.5 C	1 M NaClO$_4$ in PC-FEC	2.5–4.3 vs. Na/Na$^+$	[39]
NaNb$_{0.05}$Ti$_{1.95}$(PO$_4$)$_3$-C	Carbon-coated particles	125.3 (at 0.2 C)	91@1000@5 C	0.5 M NaPF$_6$ in PC-FEC	0.01–3.0 vs. Na$^+$/Na	[33]
NaTi(PO$_4$)$_3$-C	Carbon-coated particles	122.6 (at 0.2 C)	88@1000@5 C	0.5 M NaPF$_6$ in PC-FEC	0.01–3.0 vs. Na$^+$/Na	[33]
NaNb$_{0.05}$Ti$_{1.95}$(PO$_4$)$_3$-C	Carbon-coated particles	86 (at 0.2 C)	78@1000@1 C	0.5 M NaPF$_6$ in PC-FEC	0.01–1.5 vs. Na$^+$/Na	[33]
NaTi(PO$_4$)$_3$-C	Carbon-coated particles	82 (at 0.2 C)	72@1000@1 C	0.5 M NaPF$_6$ in PC-FEC	0.01–1.5 vs. Na$^+$/Na	[33]
NaTi$_2$(PO$_4$)$_3$@rGO	NaTi$_2$(PO$_4$)$_3$ thin films decorated with reduced graphene oxide	109.4(at 100 C)	96.5@1000@5 C	1 M NaClO$_4$ in EC-DMC-10% FEC	1.5–3.0 vs. Na/Na$^+$	[203]
Na$_3$V$_{1.98}$Al$_{0.02}$(PO$_4$)$_3$/C	Carbon-coated particles	102.7(at 10 mA g^{-1})	99.2@50@10 mA g^{-1}	1 M NaClO$_4$ in PC-FEC	2.3–3.8 vs. Na/Na$^+$	[213]
Na$_3$V$_{1.7}$Mn$_{0.3}$(PO$_4$)$_3$/C	Carbon-coated particles	104(at C/2)	-	1 M NaPF$_6$ in EC-DEC	2.0–4.3 vs. Na/Na$^+$	[106]
Na$_3$V$_{1.9}$Cr$_{0.1}$(PO$_4$)$_3$/C	Carbon-coated particles	107(at C/2)	-	1 M NaPF$_6$ in EC-DEC	2.0–4.3 vs. Na/Na$^+$	[107]
Off-stoichiometric Na$_3$V$_2$(PO$_4$)$_3$	Carbon-coated particles	102(at C/2)	-	1M NaPF$_6$ in EC-DEC	2.0–4.3 vs. Na/Na$^+$	[109]
Na$_3$V$_2$(PO$_4$)$_3$/C/TiO$_2$	Core (Na3V2(PO4)3/C nanofibers)/shell(TiO2/C nanoparticles) nanostructure	196.1 (at 0.2 C)	64.2@1500@20 C	1 M NaClO$_4$ in EC-PC	0.01–3.0 vs. Na/Na$^+$	[211]
Na$_{1.1}$Li$_{2.0}$V$_2$(PO$_4$)$_3$/C	Carbon-coated particle & nano-rod	115(at 7.14 mA g^{-1})	86@30	1 M NaPF$_6$ in EC-PC-FEC	2.5–4.0 vs. Na/Na$^+$	[208]
Na$_{1.1}$Li$_{2.0}$V$_2$(PO$_4$)$_3$/C	Carbon-coated particle & nano-rod	145(at 7.14 mA g^{-1})	50@50	1 M NaPF$_6$ in EC-PC-FEC	2.0–4.6 vs. Na/Na$^+$	[208]
Na$_3$V$_2$(PO$_4$)$_3$@C	Carbon-coated particle & nano-rod	82(at C/2)	89@5000@10 C	-	2.5–3.8 vs. Na/Na$^+$	[204]
C-LiTi$_2$(PO$_4$)$_3$	Carbon-Coated	109 (at 0.72 C)	85@40	1 M NaClO$_4$ in EC-PC	1.25–3.0 vs. Na/Na$^+$	[192]
NaV$_3$(PO$_4$)$_3$@C	Hierarchical Nanofiber	118(at 1 C)	94.2@200@10 C	1M Na$_2$SO$_4$	−0.9–0.0 vs SCE	[212]
(C@NaV$_3$(PO$_4$)$_3$)@pC	Carbon-coated Na$_3$V$_2$(PO$_4$)$_3$ nanoparticles embedded in porous carbon	103(at 10 C)	80.6@1000@10 C	1 M NaClO$_4$ in PC	2.3–3.9 vs. Na/Na$^+$	[209]
NaMo$_2$(PO$_4$)$_3$	NASICON nanoparticles	130(at C/20)	70@10@C/20	0.6 M NaPF$_6$ in PC-FEC	1.2–4.0 vs. Na/Na$^+$	[205]
NaFePO$_4$	Olivine nanoparticles	142(at 0.1 C)	70@6000@10 C	1 M NaClO$_4$ in PC-EC+5% FEC	2.0–4.0 vs. Na/Na$^+$	[111]
NaFePO$_4$/C	Microsphere	111(at 0.1 C)	90@240@0.1 C	1 M NaPF$_6$ in EC-DEC	2.1–3.8 vs. Na/Na$^+$	[110]
Na$_{0.71}$Fe$_{1.07}$PO$_4$/C	Rod-like	140 (at 0.1 C)	-	1 M NaClO$_4$ in PC+5% FEC	1.5–4.3 vs. Na/Na$^+$	[206]
NaFePO$_4$@C	NaFePO$_4$ nanodots embedded in N-doped carbon nanofibers	145(at 0.2 C)	89@6300@5 C	1 M NaClO$_4$ in PC+5 vol% FEC	1.5–4.5 vs. Na/Na$^+$	[216]
Na$_{1.2}$Ti$_{1.8}$Fe$_{0.2}$(PO$_4$)$_3$	Carbon coated-nanoparticles	130.2(at C/10)	-	1 M NaPF$_6$ in EC-DEC+1% VC	1.7–3.6 vs. Na/Na$^+$	[215]
Na$_3$V$_{1.98}$(PO$_4$)$_{2.9}$F$_{0.3}$/C	Carbon coated-nanoparticles	116.9(at 0.1 C)	89.3@100@1 C	1 M NaClO$_4$ in PC+2 vol% FEC	2.3–4.2 vs. Na/Na$^+$	[214]
Na$_3$V$_2$(PO$_4$)$_{2.93}$F$_{0.07}$/C	Carbon coated-nanoparticles	113(at 10 mA g^{-1})	86@1000@200 mA g^{-1}	1 M NaClO$_4$ in PC+2 vol% FEC	2.3–4.2 vs. Na/Na$^+$	[210]
Na$_2$FePO$_4$F-rGO	Carbon coated-nanoparticles	110(at C/10)	70@5000@10 C	1 M NaClO$_4$ in PC-FEC (95:5)	2.0–4.0 vs. Na/Na$^+$	[207]
Na$_4$Fe$_3$(PO$_4$)$_2$(P$_2$O$_7$)@rGO	Microspheres wrapped by rGO networks	128 (at 0.1 C)	62.3@6000@10 C	1 M NaClO$_4$ in EC-DEC+5% FEC	1.7–4.3 vs. Na/Na$^+$	[218]
Na$_4$MnFe$_2$(PO$_4$)$_2$(P$_2$O$_7$)	Particles	110(at C/20)	83@3000@1 C	1 M NaBF$_4$ in EC-PC	1.7–4.5 vs. Na/Na$^+$	[219]
Na$_4$Fe$_3$(PO$_4$)$_2$(P$_2$O$_7$)/C	Carbon coated	108.3(at 0.1 C)	69.1@4400@20 C	1 M NaClO$_4$ in EC-PC-5 vol% FEC	1.9–4.1 vs. Na/Na$^+$	[217]

Notes: a FEC: fluoroethylene carbonate; PC: propylene carbonate.

b Cycling stability is expressed as the capacity retention after charging/discharging cycles at a specific rate.

F-doping and V-defect $Na_3V_{1.98}(PO_4)_{2.9}F_{0.3}/C$ [214] Fe-substituted $Na_{1.2}Ti_{1.8}Fe_{0.2}(PO_4)_3$ [215], and Cr-substituted $Na_3V_{1.9}Cr_{0.1}(PO_4)_3/C$ [107] also exhibited enhanced electron conductivity and excellent structural stability.

Among the various classes of phosphates used in SIBs, olivine NaFePO$_4$ (NFP) was also one of the most attractive host materials for SIBs owing to its high theoretical capacity [19]. For example, Tang et al. [111] synthesized highly pure olivine NFP through an aqueous-based electrochemical-driven ion-exchange process from olivine LFP precursor. Compared with NFP prepared by conventional organic ion-exchange systems, aqueous ion-exchanged NFP showed improved electrochemical performance (142 mA h g^{-1} at 0.1 C, up to 6000 cycles at 10 C), which could be ascribed to the complete substitution of Li$^+$ by Na$^+$ in NFP, providing unrestricted 1D channels for Na$^+$ insertion/extraction. Following the same method, olivine NFP/C microsphere cathode was prepared as well from LFP/C by Fang et al. [110]. Generally, maricite NFP was rarely applied as electrode materials due to its electrochemical inactivity. Reducing the sizes of NFP and introducing a carbon matrix could effectively overcome this issue. For example, maricite NFP nanodots which were finely embedded in interlinked porous N-doped carbon nanofibers had been used as binder-free cathode for SIBs by Liu et al. [216]. Minimized sizes ($\approx$ 1.6 nm) and high-potential desodiation process could transform the maricite NFP into a highly active amorphous phase, showing high reversible capacity (145 mA h g^{-1} at 0.2 C), high-rate capability (61 mA h g^{-1} at 50 C), and high cyclic stability ($\approx$ 89% capacity retention over 6300 cycles). (Fig. 14a-c). Combining the merits of both high reversible capacity of iron-based phosphates (NFP) and exceptional structural stability of pyrophosphates (Na$_2$FeP$_2$O$_7$) due to the small volume change during charge/discharge, the new mixed-polyanion compound Na$_4$Fe$_3$(PO$_4$)$_2$(P$_2$O$_7$) had been explored as a promising electrode material for the SIBs [217]. For example, Yuan et al. [218] synthesized Na$_4$Fe$_3$(PO$_4$)$_2$(P$_2$O$_7$) microspheres decorated 3D graphene using a spray-drying method. Together with the flexible 3D graphene network, this mixed-polyanion Na$_4$Fe$_3$(PO$_4$)$_2$(P$_2$O$_7$)@rGO composite afforded high reversible capacity (128 mA h g^{-1} at 0.1 C), outstanding rate capability (35.1 mA h g^{-1} at 200 C), and long cycling life (62.3% capacity retention over 6000 cycles at 10 C). For further improving the energy density of the Na$_4$Fe$_3$(PO$_4$)$_2$(P$_2$O$_7$) electrode, Kim et al. [219] introduced a Fe- and Mn-based binary mixed-phosphate phase Na$_4$MnFe$_2$(PO$_4$)$_2$(P$_2$O$_7$). The binary system exhibited a higher practical power/energy density and a smaller volume change ($\sim$2%) upon cycling than those of Na$_4$Fe$_3$(PO$_4$)$_2$(P$_2$O$_7$). And the high energy density was attributed to the combined high potential of the Mn^{2+}/Mn^{3+} redox couples as well as the Fe^{2+}/Fe^{3+} redox potential and enhanced intercalation kinetics.

5.2. K-ion batteries

After the alkali elements of Li and Na, potassium (K) has attracted great attention in MIBs because of its element abundance and similar electrochemical properties to LIBs. Also, small solvated ions of K$^+$, low K$^+$ desolvation energy, and low reduction potential of K$^+$/K^0 (–2.88 V *vs.* SHE) result in high working voltages and high energy densities in KIBs, which makes KIB system show great potential in energy-storage field [37]. On the other side, larger ionic radius of K$^+$ (1.38 Å) than those of Li$^+$ and Na$^+$ (0.76 and 1.02 Å, respectively), is likely to induce large volume expansion leading to low specific capacity and unsatisfactory cycle stability during the insertion reaction, which makes KIBs less attractive in practical applications [36] as shown in Table 9.

Therefore, there are still great challenges faced by the development of KIBs. Chihara et al. [34] studied the electrochemical properties of KVOPO$_4$ and KVPO$_4$F in KIBs. KVOPO$_4$ and KVPO$_4$F showed good electrochemical performances even upon charging to 5.0 V, and both have delivered a discharge capacity of around 80 mA h g^{-1}. Their capacity retention at 5 C was 90.7% (KVPO$_4$F) and 93.9% (KVOPO$_4$), demonstrating the material's excellent rate capability. Phase transitions of KVOPO$_4$

during K$^+$ extraction was also studied using *in situ* XRD. Results revealed that KVOPO$_4$ showed a series of phase transitions with a peculiar single-phase structural evolution, followed by a single-phase reaction and a two-phase transition process. Lian et al. [37] further studied the electrochemical properties of K$_{1-x}$VOPO$_4$ in KIBs including phase transformation, ionic diffusion, and charge transfer mechanisms. They revealed that the material showed two phase transitions during K$^+$ extraction, taking place in the ranges of $0 \leq x \leq 0.5$ and $0.625 < x \leq 0.75$, and small volume change of 6.6% has occurred during these processes, which was beneficial for the cycle stability of KIBs. Meanwhile, both V cations and O anions were involved in the charge transfer process. More importantly, the 1D diffusion pathway for K$^+$ with low energy barriers of 0.214-0.491 eV ensured fast K$^+$ mobility resulting in high rate capability. Wei et al. [36] reported hierarchical spheroid-like KTi$_2$(PO$_4$)$_3$@C nanocomposites used as an anode material for both KIBs and LIBs. Conductive carbon network and porous structure were beneficial for outstanding electrochemical performance with high reversible capacity (283.7 mA h g^{-1} for SIBs; 292.7 mA h g^{-1} for KIBs) and superior rate capability (136.1 mA h g^{-1} at 10 A g^{-1} for SIBs; 133.1 mA h g^{-1} at 1 A g^{-1} for KIBs), demonstrating the material an attractive anode material for KIBs.

5.3. Ca-ion batteries

Due to the abundant resource of calcium in the earth's crust, CIBs have also been regarded as the substitution of LIBs [220]. However, compared with LIBs and SIBs, only a few materials are active for Ca-based battery systems when multivalent metal was utilized as anode. Great efforts have been made by researchers to develop the host structures for calcium ions. For example, Na$_2$FePO$_4$F, stabilized in a layered structure, was a reasonable choice as a host for CIBs due to the similar ionic sizes between Na$^+$ and Ca^{2+} [87]. To better understand the electrochemical behavior of Ca^{2+} intercalation into desodiated Na$_2$FePO$_4$F, Lipson et al. [199] investigated the mechanism of Ca^{2+} intercalation into Na$_2$FePO$_4$F from a nonaqueous electrolyte and explored its cycling performance and voltage behavior. Based on XRD measurements, the intercalation mechanism appeared similar to that of SIBs with the appearance of an intermediate half-filled phase. The voltage of intercalation was at approximately 2.6 V, and the capacity was about 80 mA h g^{-1}, showing a great potential as a CIB cathode.

5.4. Mg-ion batteries

Similar to CIBs, there are limited materials for mg-ion batteries because of sluggish reaction kinetics or even deactivation of the host materials. To improve the activity of electrode materials, Xiao et al. [221] proposed the water-activated layered-structure VOPO$_4$ as cathode material and investigated the impact of water on both VOPO$_4$ lattice and organic electrolyte. Electrochemical measurements demonstrated that water in VOPO$_4$ lattice and organic electrolyte could activate VOPO$_4$ cathode. As shown in Fig. 14d-e, the capacity of VOPO$_4$ was increased by introducing water in electrode or electrolyte. Also, introducing water in both VOPO$_4$ electrode and electrolyte significantly reduced the voltage hysteresis from 1.15 to 0.49 V, indicating the significant promotion of the kinetics. As a result, VOPO$_4$ 2H$_2$O in the water-containing electrolyte showed decent cycle stability and high coulombic efficiency, which showed water-activated VOPO$_4$ could be a potential cathode material for Mg-ion batteries in term of the thermodynamics and kinetics.

6. Advanced characterization technologies and theoretical calculation towards phase transitions

With ever-increasing attention on phosphate materials, advanced characterization techniques and reasonable simulation methods were applied to further explore the internal properties and subtle changes during real-time testing of phosphate materials. Some studies have found
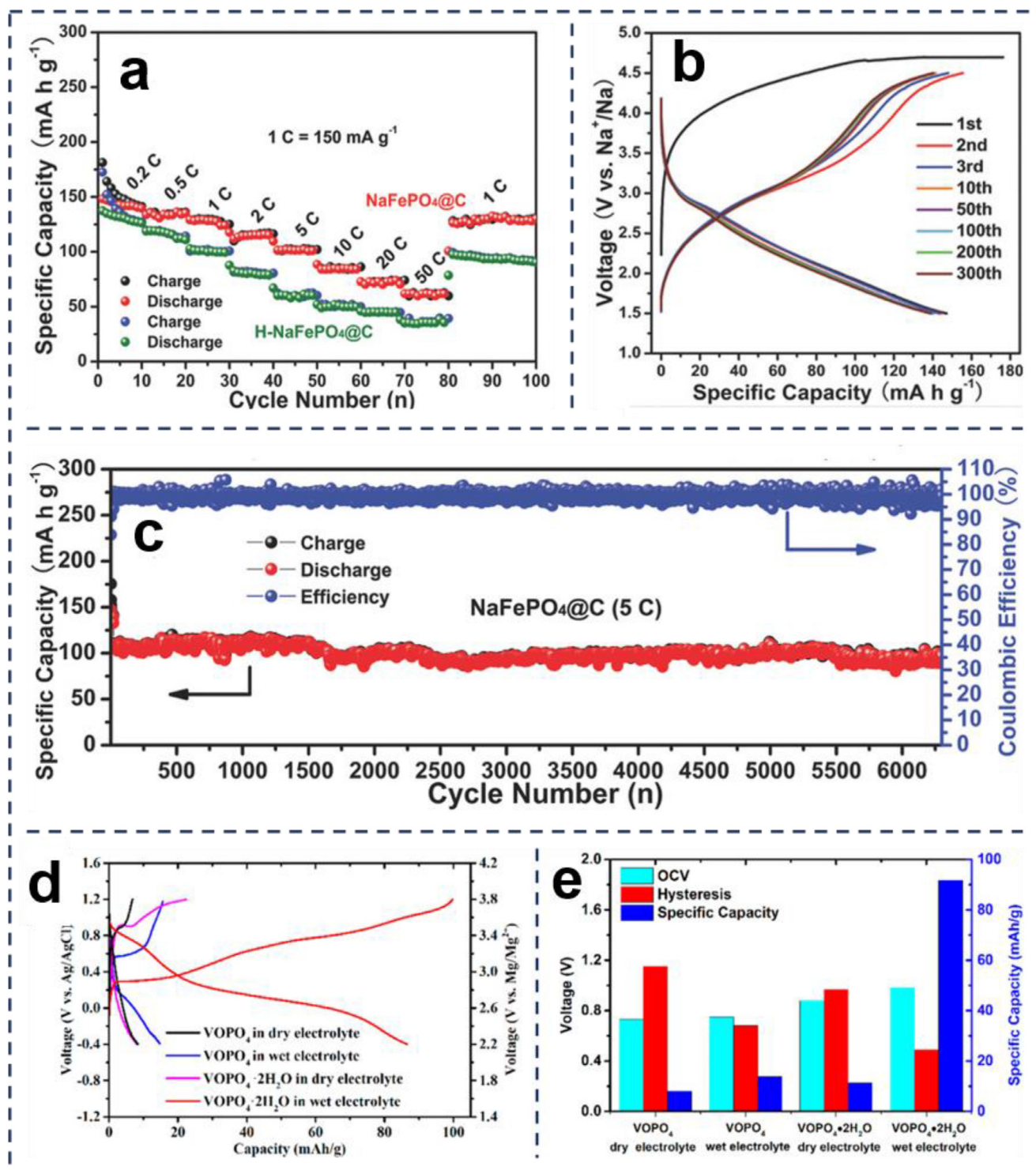
Fig. 14. (a) Rate capability of the NaFePO$_4$@C electrode in comparison with that of the H-NaFePO$_4$@C electrode; (b) Galvanostatic charge/discharge profiles at a current density of 20 mA g^{-1}; (c) Long-term cycling performance of the NaFePO$_4$@C electrode at 5 C rate. (a-c) Reproduced with permission [216]. Copyright 2018, Wiley-VCH. (d) Typical voltage profiles of VOPO$_4$ and VOPO$_4$ 2H$_2$O in dry (0.1 M Mg(ClO$_4$)$_2$-PC) and wet (0.1 M Mg(ClO$_4$)$_2$ 6H$_2$O-PC) electrolyte at a constant current density of 5 mA g^{-1} in a three-electrode cell with Ag/AgCl and active carbon as reference and counter electrode, respectively; (e) OCVs, hysteresis, and specific capacities of the tenth cycle for VOPO$_4$ and VOPO$_4$ 2H$_2$O in dry and wet electrolytes, the hysteresis was calculated by subtracting the mid voltage of charge by that of discharge. (d, e) Reproduced with permission [221]. Copyright 2018, American Chemical Society.

Table 9
Performances of recently reported KIBs, CIBs and magnesium-ion batteries based on phosphates with corresponding morphologies.

| Materials	Morphology	Capacitance	Capacity retention [%]	Electrolytes	Voltage, V	Ref.
$KTi_2(PO_4)_3@C$	Porous spheroids	292.7 mA h g^{-1} (at 20 mA g^{-1})	75.7@50@20 mA g^{-1}	0.8 M KPF$_6$ in EC-DEC	0.01–3.0 vs. K/K$^+$	[36]
$KVPO_4F$	Micron particles	92 mA h g^{-1} (at C/20)	97@30	1 M KPF$_6$ in EC-PC	2.0–5.0 vs. K/K$^+$	[34]
$KVOPO_4$	Micron particles	84 mA h g^{-1} (at C/20)	97@30	1 M KPF$_6$ in EC-PC	2.0–5.0 vs. K/K$^+$	[34]
Na_2FePO_4F	Micron particles	80 mA h g^{-1} (at 10 mA g^{-1})	-	0.2 M Ca(PF$_6$)$_2$ in EC-PC(3:7)	0.0–3.0 vs. Ca/Ca$^+$	[199]
$VOPO_4$	Layered-structure	8 mA h g^{-1} (at 5 mA g^{-1})	-	0.1 M Mg(ClO$_4$)$_2$ in PC	−0.4–1.2 vs. Ag/AgCl	[211]
$VOPO_4$ 2H$_2$O	Layered-structure	11.2 mA h g^{-1} (at 5 mA g^{-1})	-	0.1 M Mg(ClO$_4$)$_2$ in PC	−0.4–1.2 vs. Ag/AgCl	[211]
$VOPO_4$ 2H$_2$O	Layered-structure	91.7 mA h g^{-1} (at 5 mA g^{-1})	100@30@5 mA g^{-1}	0.1 M Mg(ClO$_4$)$_2$ 6H$_2$O in PC	−0.4–1.2 vs. Ag/AgCl	[211]
$VOPO_4$	Layered-structure	13.8 mA h g^{-1} (at 5 mA g^{-1})	-	0.1 M Mg(ClO$_4$)$_2$ 6H$_2$O in PC	−0.4–1.2 vs. Ag/AgCl	[211]

Note: Cycling stability is expressed as the capacity retention after charging/discharging cycles at a specific rate.

that phosphate electrodes were accompanied by phase transition during ion absorption and desorption, which may lead to poor cycle performance [31]. In fact, the real phase transition behavior can be precisely characterized by *in situ* XRD together with phase-field model and high-throughput ab initio analysis. Moreover, *in situ* characterizations and computational principles based on density functional theory (DFT) are nowadays accurate to provide insights into the fundamental properties of electrode materials.

6.1. Advanced characterization technologies

For *in situ* XRD technology, a synchrotron radiation source that radiates hard X rays with high photo energy and short wavelength and owns powerful penetration is required [222]. For phosphates, *in situ* XRD is primarily used for the observation of phase transitions occurring upon ion insertion/extraction process. Bramnik et al. [223] revealed a stepwise appearance of two new phases (*e.g.*, Li$_{0.7}$CoPO$_4$ and CoPO$_4$) which have the same olivine-like structure as the pristine compound upon electrochemical lithium extraction from LiCoPO$_4$ by *in situ* XRD. As shown in Fig. 15a, the potentiodynamic cycling showing two pronounced oxidation (4.8 and 4.9 V vs Li/Li$^+$) and two reduction peaks (4.7 and 4.8 V vs Li/Li$^+$) after the first cycle occurred as two successive Li$^+$ extraction plateaus in charge curve. *In situ* XRD characteration in Fig. 15c further proved the stepwise phase separation upon lithium extraction from this compound, revealing the existence of an intermediate phase Li$_{0.7}$CoPO$_4$ (Fig. 15b). In the initial stage of charge, the formation of a second olivine-like phase (Li$_{0.7}$CoPO$_4$) was indicated by the appearance of a second set of reflections, *e.g.*, 200, 020, and 301. This new phase with a lattice parameter ($a = 10.070(3)$Å, $b = 5.851(2)$ Å, $c = 4.717(2)$ Å) corresponded to the extraction of 0.3 Li per formula unit of LiCoPO$_4$. After approximately 0.3 Li per formula unit of LiCoPO$_4$ was extracted, the reflections of a phase 3 (CoPO$_4$) appeared. With increasing intensity of reflections (phase 3), the reflection intensity of phase 2 decreased. However, this transformation was not complete at the end of charge, and the reflections from phase 2 were still present after the extraction of one lithium from LiCoPO$_4$, which may result from some parasitic reactions that contributed slightly to the charge passed through the cell and resulted in the discrepancy between calculated and real lithium content in the cathode. Overcharging experiment upon phase 3 *in situ* cell proved its olivine-like structure which was unstable in air but can be recovered under *in situ* conditions. During discharge, reflections of phase 3 disappeared completely at the end of discharge, showing a opposite directions against charging in a reversible manner. Similarly, phase transitions and volume variations occurring during lithium extraction from LVP were studied by *in situ* XRD [224]. Results showed that rhombohedral LVP showed single a two-phase transition between Li$_3$V$_2$(PO$_4$)$_3$ and Li$_1$V$_2$(PO$_4$)$_3$ (Fig. 15c) and monoclinic LVP showed a much more complicated process of four successive two-phase transitions on Li$^+$ extraction to Li$_{0.1}$V$_2$(PO$_4$)$_3$ between 3.4 and 4.6 V *vs.* Li (Fig. 15d), which is consistent with mentioned above in electrochemical reaction part. *In situ* XRD (Fig. 15c) during Li extraction from rhombohedral Li$_3$V$_2$(PO$_4$)$_3$ showed that intensities were altered at small an-

gles by stronger absorption and the space group changes from $R\overline{3}$ to $R\overline{3}$ into which all the diffraction peaks were indexed. For lithium extraction from monoclinic Li$_3$V$_2$(PO$_4$)$_3$, four new phases were involved, *e.g.*, Li$_{2.5}$V$_2$(PO$_4$)$_3$, Li$_2$V$_2$(PO$_4$)$_3$, LiV$_2$(PO$_4$)$_3$, and V$_2$(PO$_4$)$_3$. As showed in Fig. 15d, the first two-phase transition occurred between Li$_3$V$_2$(PO$_4$)$_3$ and Li$_{2.5}$V$_2$(PO$_4$)$_3$. The positions and intensities of the diffraction peaks of this first intermediate phase were different from those of the pristine material with a relatively big shift of the (201) reflection at $2\theta \sim 23.2°$ and an important change in intensity ratios in the region $2\theta \sim 24.2°$ to 24.7°. The second two-phase process occurred between Li$_{2.5}$V$_2$(PO$_4$)$_3$ and Li$_2$V$_2$(PO$_4$)$_3$ at ca.3.7 V *vs.* Li. On further Li extraction, a third two-phase process was encountered at 4.06 V *vs.* Li between Li$_2$V$_2$(PO$_4$)$_3$ and LiV$_2$(PO$_4$)$_3$. The diffractograms displayed the peaks of both Li$_2$V$_2$(PO$_4$)$_3$ and LiV$_2$(PO$_4$)$_3$. In the end of this stage, two lithium ions were extracted from Li$_2$V$_2$(PO$_4$)$_3$ to LiV$_2$(PO$_4$)$_3$, resulting in the full oxidation of V^{3+} to V^{4+}. At higher voltage (Ca. 4.35 V) where polarization was much more obvious, the fourth two-phase reaction was indeed observed between LiV$_2$(PO$_4$)$_3$ and Li$_{0.1}$V$_2$(PO$_4$)$_3$ with part of V^{4+} being oxidized into V^{5+}. Moreover, at this stage, partial vanadium may dissolve into the electrolyte when deep oxidation to 4.6 V *vs.* Li [225]. LiMn$_{0.6}$Fe$_{0.4}$PO$_4$ was characterized to experience two two-phase regions during charging by *in situ* XRD. Fig. 15e-f showed the changes of diffraction patterns of Li$_x$Mn$_{0.6}$Fe$_{0.4}$PO$_4$ during charging of the cell to the composition x = 0. Phase 1 was the pristine compound LiMn$_{0.6}$Fe$_{0.4}$PO$_4$ for the range including the [020], [211], and [301] reflections. In the first step, when x = 0.67, phase 2 arisen, corresponding to charging up to the composition Li$_{0.67}$Mn$_{0.6}$Fe$_{0.4}$PO$_4$. The reflections from both phases (phases 1 and 2) were very close to each other, which indicated a very similar lattice parameter between these two phases. In the second step, in the range $0.1 \leq x \leq 0.55$, two olivine-like phases (phases 2 and 3) coexisted and counteracted and reflections were much more clearly separated. During the whole charging process, the reflections of the new phase were growing at slightly higher 2θ values in comparison with prior one [222]. Li$^+$ insertion mechanism in monoclinic LFP and LVP was also investigated by Patoux et al. [225] using *in situ* XRD technology. Recorded in Fig. 15g-h, LVP showed four reversible redox processes upon insertion of two Li$^+$ (V^{3+}/V^{2+} couple) at 1.98, 1.88, 1.73 and 1.70 V *vs.* Li. and LFP showed two reversible redox processes upon insertion of two Li$^+$ (Fe^{3+}/Fe^{2+} couple) at 2.88 and 2.73 V *vs.* Li. *In situ* X-ray diffraction of both compositions showed a very similar behavior. Because of the diffraction peaks of the monoclinic $P2_1$/n unit cell overlap, satisfactory refinement of the lattice parameters of the intermediate composition Li$_4$M$_2$(PO$_4$)$_3$ and of the final composition Li$_5$M$_2$(PO$_4$)$_3$ were difficult. For both compounds, transformations between the two definite compositions Li$_3$M$_2$(PO$_4$)$_3$ and Li$_4$M$_2$(PO$_4$)$_3$ had similar trends: contraction along (100) (−1.5%), elongation along (010) and (001) (+1.6 and +1.5%, respectively) and increase of the monoclinic distortion to 91.1°. Also, for both Na$_{2+x}$TiM(PO$_4$)$_3$ and Li$_{1.6+x}$Na$_{0.4}$TiM(PO$_4$)$_3$ ($0 \leq x \leq 1$ for M = Cr, $0 \leq x \leq 2$ for M = Fe), the insertion proceeded a single-phase mechanism evidenced by slow intermittent titration techniques (GITT, PITT) and *in situ* XRD [226]. Fig. 16a showed the electrochemical data recorded during lithium insertion into Li$_{1.6}$Na$_{0.4}$TiFe(PO$_4$)$_3$
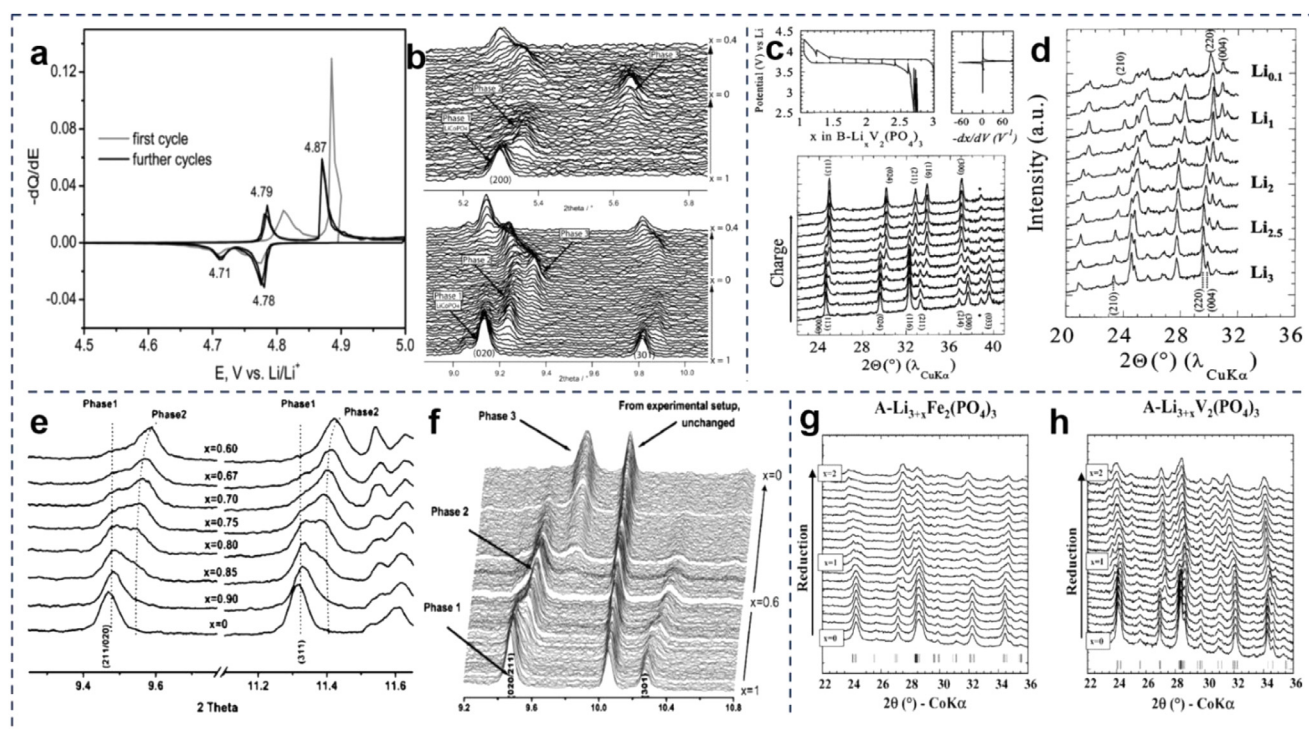
Fig. 15. (a) Incremental capacity plot obtained by potentiodynamic cycling with Ilim close to C/12 (ΔE = 5 mV); (b) Selected regions in the diffraction patterns taken *in situ* during the first charge-discharge cycle. 200, 020, and 301 reflections are shown (λ = 0.47189 Å). (a, b) Reproduced with permission [223]. Copyright 2007, American Chemical Society. (c) *In situ* XRD data of the electrochemical extraction of lithium from rhombohedral B-$Li_3V_2(PO_4)_3$; (d) Selected XRD patterns at intermediate A-$Li_{3-x}V_2(PO_4)_3$ compositions (x=0.5, 1, 2, and 2.9). In-between patterns are shown to illustrate the two-phase reactions. (c, d) Reproduced with permission [224]. Copyright 2003, The Electrochemical Society. (e) Selected diffraction patterns collected upon charging to the composition $Li_{0.6}Mn_{0.6}Fe_{0.4}PO_4$; (f) Evolution of the diffraction patterns upon charging the cell. (e, f) Reproduced with permission [222]. Copyright 2005, The Electrochemical Society. (g) *In situ* X-ray diffraction recorded during Li insertion in GITT mode into (g) $Li_3Fe_2(PO_4)_3$ and (h) $Li_3V_2(PO_4)_3$. Diffractometer D8 Bruker, Co Kα, θ–θ geometry, PSD counter. (g, h) Reproduced with permission [225]. Copyright 2003, Elsevier.

and $Li_{1.6}Na_{0.4}TiCr(PO_4)_3$. For $Li_{1.6}Na_{0.4}TiCr(PO_4)_3$, only one electron per formula unit could be exchanged for this materials as a direct consequence of the electrochemical inactivity of chromium in the range of potentials (3.4-2.0 V *vs.* Li$^+$/Li, 3.1-1.7 V *vs.* Na$^+$/Na). On the contrary, for $Li_{1.6}Na_{0.4}TiFe(PO_4)_3$, two electrons were exchanged per formula unit thanks to the Ti^{4+} and Fe^{3+}, which could be reduced into Ti^{3+} and Fe^{2+}. As we can see, average potential of the Ti$^{4+/3+}$ redox couple was located at 2.55 V *vs.* Li$^+$/Li. Current decays recorded in PITT mode (Fig. 16b) suggested a solid solution process for the whole intercalation range noting a kinetic limitation of the electron transport inside the material rather than a lithium diffusion limitation (front-phase migration). *In situ* XRD (Fig. 16c) further confirmed the solid-solution process evocated from the PITT data by the continuous shift of all the diffraction peaks (no change of space group) on lithium insertion. For sodium inserted into both $Na_2TiFe(PO_4)_3$ and $Na_2TiCr(PO_4)_3$, the potentials of the Fe^{3+}/Fe^{2+} and Ti^{4+}/Ti^{3+} redox couples as well as the property of single-phase reactions were the same to lithium inserted into $Li_{1.6}Na_{0.4}TiM(PO_4)_3$, which was also evidenced by the current decay in PITT mode and *in situ* XRD patterns (Fig. 16d). Lithium-insertion mechanism in $FePO_4 \cdot nH_2O$ was also investigated in detail by Delacourt et al. [227] using *in situ* XRD combined Mössbauer and X-ray absorption spectroscopies (XAS). Fig. 16e is the *in situ* XRD patterns of crystalline phosphosiderite (P-$FePO_4 \cdot 2H_2O$) upon lithium insertion into P-$FePO_4 \cdot 2H_2O$. Bragg reflections of P-$FePO_4 \cdot 2H_2O$ progressively disappeared together with the appearance of the diffraction lines of a new phase at d = 2.55, 1.88, 1.50, and 1.48 Å. This lithiated phase was indexed in the same space group as P-$FePO_4 \cdot 2H_2O$ (*i.e.*, P2$_1$/n) with the lattice parameters a = 5.31(1) Å, b = 10.0(2) Å, c = 8.72(3) Å, and β = 90.3(4)° revealing a complete two-phase lithium-insertion mechanism. For crystalline strengite (S-$FePO_4 \cdot 2H_2O$) (Fig. 16f), the diffraction lines of a new

phase appeared (most intense lines at d = 2.55, 1.88, and 1.49 Å). Upon further lithium insertion, a progressive shift of the diffraction lines of this new phase occurred, which suggested that it accommodated more lithium, through a single-phase process. All the diffraction features of S-$FePO_4 \cdot 2H_2O$ revealed a two-phase region followed by a single-phase one.

Besides *in situ* XRD, *in situ* X-ray absorption near edge structure (XANES) which usually was used to characterize the valence states of elements, etc. and *in situ* Raman microscopy that was used to explore the staged evolution of phases and internal properties were also used. For example, Tang et al. [111] used Operando Fe K-edge XANES and XRD to study the state of the phase during the sodiation/desodiation of $NaFePO_4$. Operando Fe K-edge XANES characterization of the $NaFePO_4$ was carried out during the initial galvanostatic cycling. As shown in Fig. 17a, voltage prole of the initial cycle was indicated alongside stacked plots (Fig. 17b) and two-dimensional (2D) contour plots (Fig. 17c) of operando XANES spectra for $NaFePO_4$. Upon charging (desodiation), the Fe K-edge was rigidly shifted toward the higher binding energy, corresponding to increased Fe oxidation state during the charging process. In a similar way, the insertion of sodium ions was combined with the reduction of Fe to its original state. Fig. 17d showed the evolution of the edge energy (half weight) of the XANES spectra by taking $LiFePO_4$ as ref. The energy evolution consisting of five regions with different linear slopes associated with the bonding strength of 1s electrons of iron in different structures correlated well with asymmetry of charge-discharge profile. Two-stage charge mechanism in Fig. 17a was also reflected in regions (i) and (ii) of Fig. 17d corresponding to the transformation of $NaFePO_4$ to the $Na_{2/3}FePO_4$ intermediate phase through a solid solution process and the transformation of intermediate phase to further desodiated $FePO_4$ phase. Phase transition behavior in
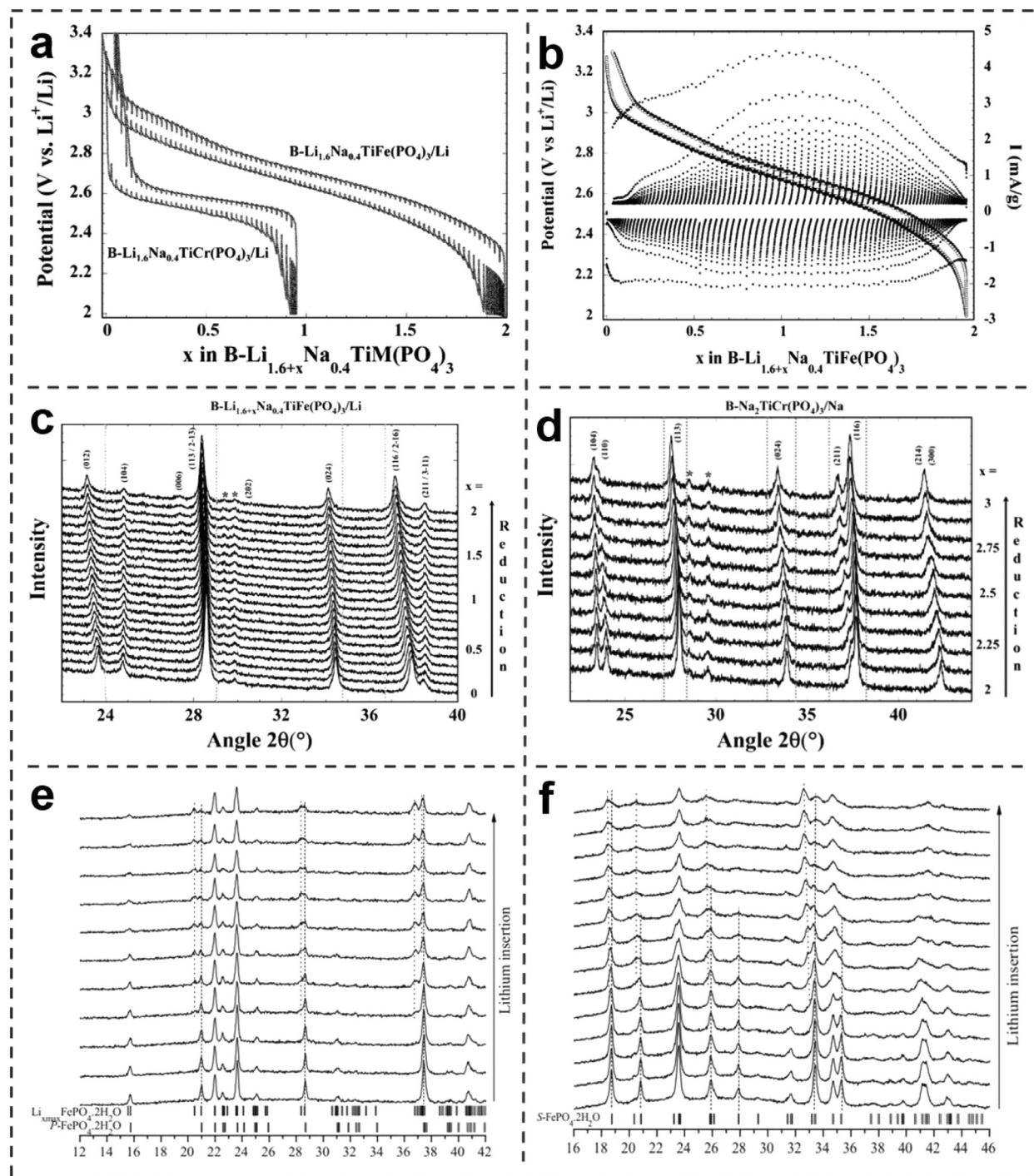
Fig. 16. (a) Potential-composition curves vs Li$^+$/Li of B-Li$_{1.6}$-Na$_{0.4}$TiFe(PO$_4$)$_3$ and B-Li$_{1.6}$Na$_{0.4}$TiCr(PO$_4$)$_3$, performed in a galvanostatic intermittent mode (GITT): regime of C/20 for 30 min and relax periods of 30 min; (b) Potentiometric titration curve (PITT) of B-Li$_{1.6}$-Na$_{0.4}$TiFe(PO$_4$)$_3$ in the 3.4-2.0 V range vs Li$^+$/Li (imin) 3.5 μA, equivalent to a C/300 regime); (c) Evolution of the *in situ* X-ray diffraction patterns of an electrode of B-Li$_{1.6}$Na$_{0.4}$TiFe(PO$_4$)$_3$ during the insertion of lithium, under a GITT mode in the 3.4-2.0 V range vs Li$^+$/ Li. Acquisition time of 1 h in the 15.00-45.00 2θ (°) angular range from Co KR radiation on a D8-Bruker diffractometer equipped with a PSD counter; (d) Evolution of the *in situ* X-ray diffraction patterns of an electrode of B-Na$_2$TiCr(PO$_4$)$_3$ during the insertion of sodium, under a GITT mode in the 3.1-1.7 V range vs Na$^+$/ Na. Acquisition time of 1 h in the 15.00-45.00 2θ(°) angular range from a Co KR radiation on a D8 Bruker diffractometer equipped with a PSD counter. Asterisks denote contributions from the cell hardware. (a-d) Reproduced with permission [226]. Copyright 2013, American Chemical Society. (e) *In situ* XRD patterns upon lithium insertion into *P*-FePO$_4$ 2H$_2$O galvanostatic discharge at C/20 with relax periods of 50 min. Dashed lines are for the diffraction lines of *P*-FePO$_4$ 2H$_2$O and dotted lines are for the diffraction lines of the lithiated phase and (f) *In situ* XRD patterns upon lithium insertion into *S*-FePO$_4$ 2H$_2$O galvanostatic discharge at C/20 with relax periods of 1 h. Dashed lines are for the diffraction lines of *S*-FePO$_4$ 2H$_2$O and dotted lines are for the diffraction lines of the lithiated phase. (e-f) Reproduced with permission [227]. Copyright 2009, The Electrochemical Society.
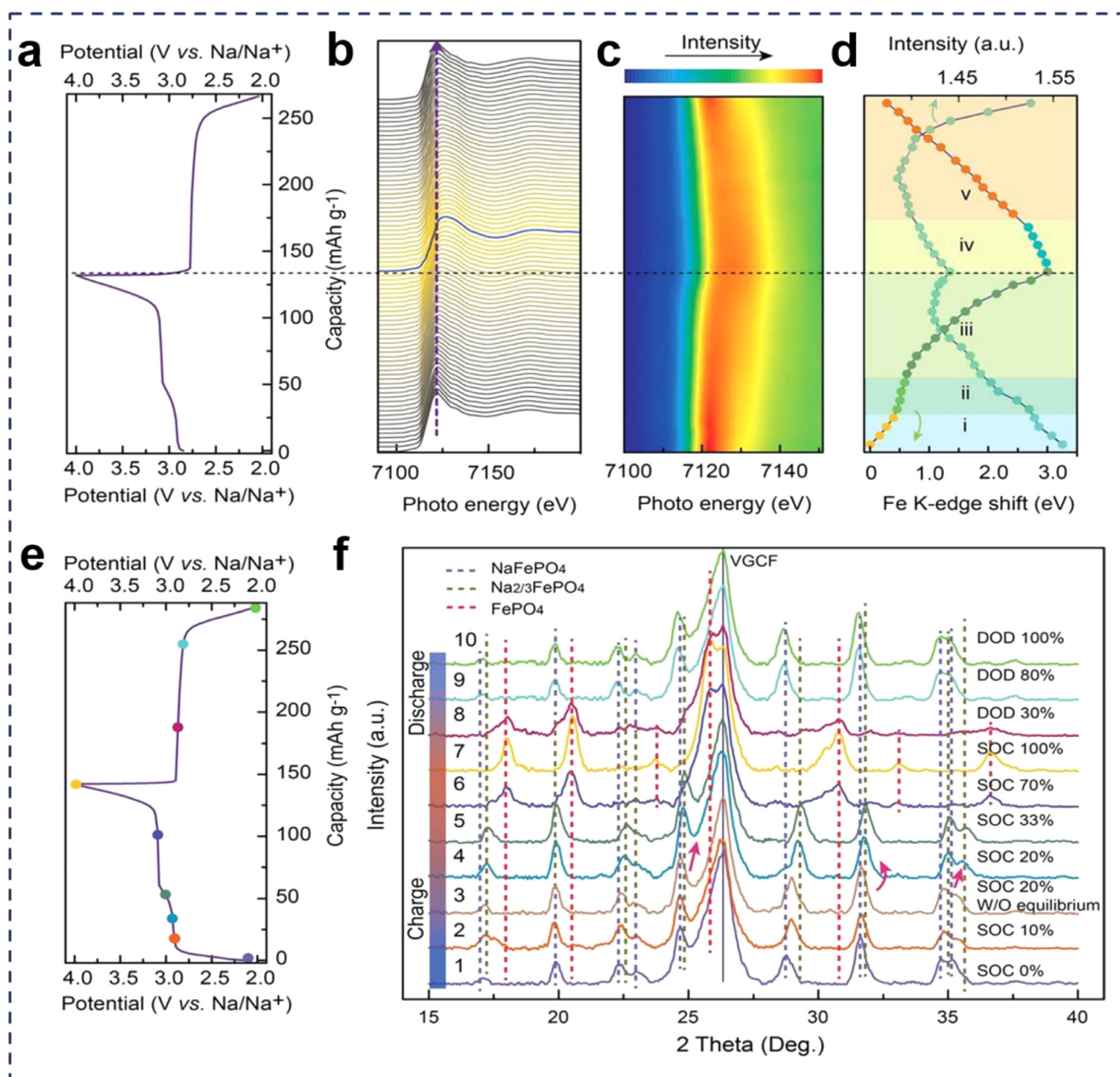
Fig. 17. In situ synchrotron Fe K-edge XANES and ex situ XRD studies of the aqueous ion-exchanged NaFePO$_4$ during initial cycles. (a) Voltage profile of the NaFePO$_4$ at the first cycle; (b) stacking plots; (c) two-dimensional (2D) contour plots and (d) the evolution of the Fe-edge energy (half weight) of operando XANES spectra of the NaFePO$_4$ at the first cycle; (e) Voltage profile of the NaFePO$_4$ at the second cycle; (f) XRD patterns of NaFePO$_4$ electrodes at different stages (equilibrium and non-equilibrium) (a-f) Reproduced with permission [111]. Copyright 2016, The Royal Society of Chemistry.

XRD spectra collected at different equilibrium stages at 0.1C (Fig. 17e-f) agreed well with the XANES spectra.

In the study of Membreño et al. [180], *in situ* Raman microscopy was used to probe the phase stability of microcrystalline α-LVP upon thermal and laser heating. Fig. 18a-c, *in situ* Raman spectra of α-LVP at different heating temperatures under air, showed the spectral changes from room temperature to 600°C. There were no obvious changes from 23.5 to 116.7°C (Fig. 18a), indicating that the monoclinic phase was stable within this temperature range. At 125°C, the 1030 cm^{-1} peak and shoulder at 1079 cm^{-1} disappeared until 202.0°C at which more dramatic changes (such as broadening of the 1009 cm^{-1} peak, merging of the 435 and 455 cm^{-1} peaks into a single peak, transformation of the 979 cm^{-1} peak into a shoulder, and a significant diminishing of the lattice modes.) took place (Fig. 18b). With increasing heating temperature

(Fig. 18c), additional spectral changes occurred, such as peak at 1140 cm^{-1} at 333.7°C that gradually grew in intensity with higher heating temperatures and experienced a slight blue shift once reaching 595.8°C. Moreover, at 595.8°C, a new peak at 876 cm^{-1} became the dominant mode of the spectrum. It was expected that monoclinic α-LVP experienced two structural phase transitions, β and γ, occurring at elevated temperatures before degradation to α-LiVOPO$_4$ under an oxygen-rich atmosphere

6.2. Theoretical calculation methodology

Phase transformation of phosphate during ion intercalation/de-intercalation has been described above. More complicated processes such as the mechanisms of phase transitions, charge transfer in redox reactions, and ionic diffusion kinetics required deep understanding. The-
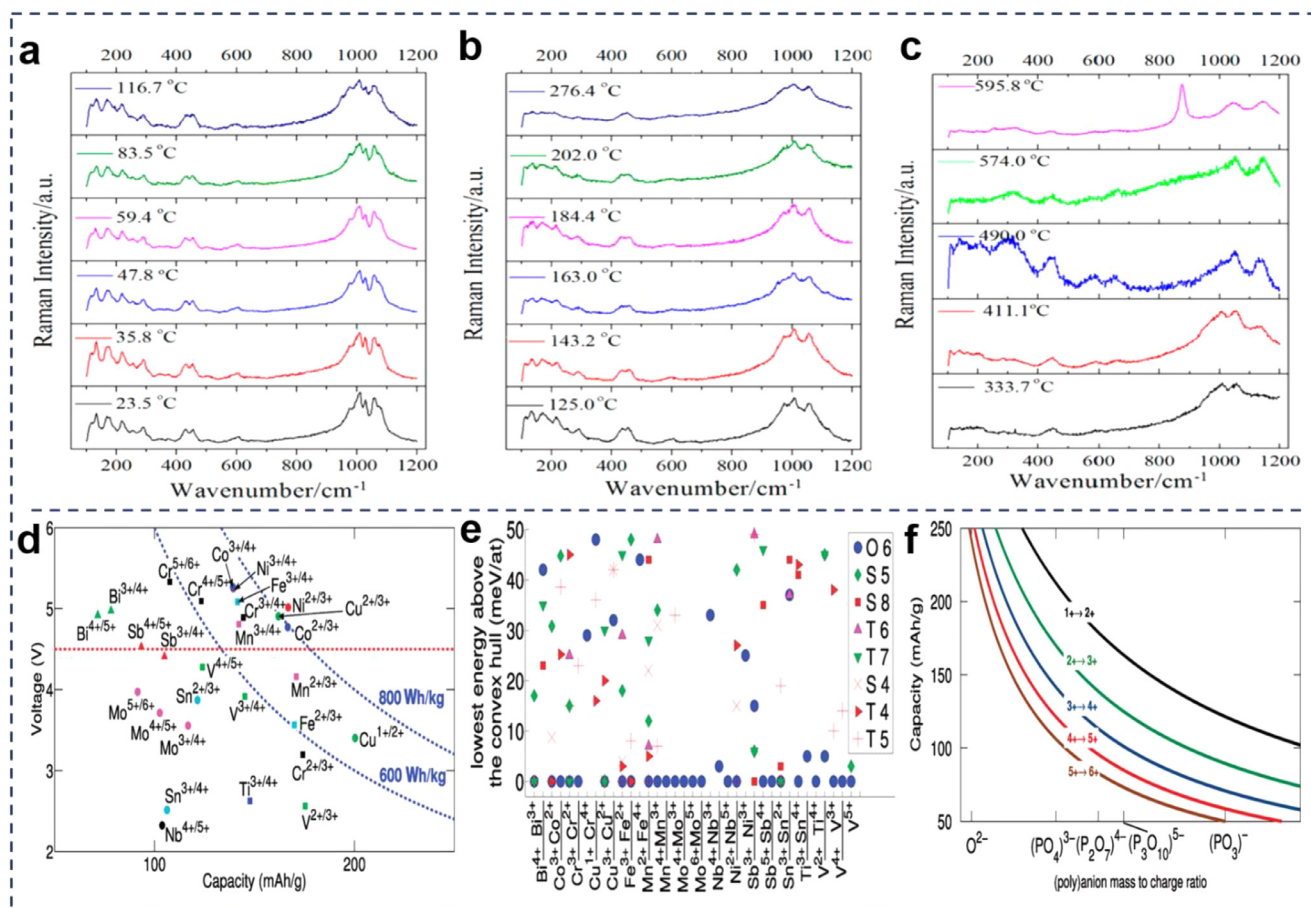
Fig. 18. (a-c) *In situ* Raman spectra of α-Li$_3$V$_2$(PO$_4$)$_3$ at different heating temperatures under air: (a) from 23.5 to 116.7°C, (b) 125.0 to 276.4°C, and (c) 333.7 to 595.8°C taken with a 50 $\times$ objective and a laser power of 0.855 mW for 300 s. (a-c) Reproduced with permission [180]. Copyright 2013, American Chemical Society. (d) Mean voltage in phosphates versus maximum gravimetric capacity achievable. Specific energy curves at 600 and 800 Wh kg^{-1} are drawn on the figure (blue dashed lines). The red dashed line indicates the upper voltage which we consider safe against decomposition of the electrolyte. Different colors and markers have been used for different elements; (e) Lowest distance to the convex hull for different coordination environments of each ionic species in our phosphate data set. Each symbol refers to a different local environment: O6, octahedral; S4, square planar; T4, tetrahedral; S5, square pyramidal; T5, trigonal bipyramidal; T7, trigonal prismatic square face monocapped; T6, trigonal; and S8, square antiprismatic. An energy above the hull of 0 meV/at indicates that the environment is found in a compound thermodynamically stable at 0 K; (f) Best achievable gravimetric capacity for different M$^{(n-1)+}$/M^{n+} couples as a function of the mass-to-charge ratio of the (poly)anion. Oxides and different phosphate polyanions are indicated on the mass-tocharge ratio axis. For the sake of comparison, this plot assumes the mass of iron for the M element. (d-f) Reproduced with permission [7]. Copyright 2011, American Chemical Society.

oretical calculation method like, first-principles calculations [37], high-throughput ab initio calculations [7], and phase-field model [31] are developed to understand and even predict many important battery properties. For example, based on density functional theory (DFT), Hautier et al. [7] computed the voltage, capacity (gravimetric and volumetric), specific energy, energy density, stability, and safety of thousands of phosphate compounds by means of high-throughput ab initio methodology. Taking the voltage as an example, as shown in Fig. 18d, the average voltage for each couple with respect to the best achievable capacity in a phosphate was computed. These important parameters provided guidance for the design of new phosphate electrode materials. Thermodynamic stability of series of phosphates under hypothesis condition of zero K and zero pressure was computed above the hull. Moreover, the lowest energy above the hull of each ion in different coordination environments were plotted. As shown in Fig. 18e, each symbol indicated a different local environment. Overlap between symbols could happen when two local environments were present in the same compounds or in compounds with similar stability. Zero energy above the hull indicated that at least one stable compound existed with this coordination environment. The maximum achievable capacity for a one-electron delithiation process depends on the one-electron couple used

(M^{1+}/M^{2+}, M^{2+}/M^{3+},...), the mass of the element M, and the charge to mass ratio for X. Fig. 18f plotted the maximum capacity for different one-electron redox couples (the different colored lines) as function of the charge-to-mass ratio of the (poly)anion X. The importance of the cation charge and the charge-to-mass ratio on the anion was highlighted, which revealed that for a high valent cation redox couple (*e.g.*, M^{5+}/M^{6+}), a large amount of anion mass I was required in the compound to compensate, thereby decreasing the specific capacity. Hence, from a specific energy perspective, low valent redox couples, with reasonably high voltage and combined with (poly)anions with high negative charge-to-mass ratio, are optimal.

Ab initio methodology was also used to study the mechanism of aqueous-based (H$_2$O) and organic-based (EC) electrochemical-driven ion-exchange process for the transformation of olivine LFP into highly pure olivine NFP [111]. Intercalation kinetics in organic and aqueous electrolytes, an atomic level calculation and comparison of Na$^+$/Li$^+$ energies involved in the migration process in the electrolytes and the electrolyte/cathode interface was investigated. M (M = Li and Na) ion in aqueous solution and EC-based electrolyte formed M$^+$(H$_2$O)$_4$ and M$^+$(EC)$_4$ molecules. Fig. 19a-b showed the possible behavior for Na/Li ion diffusion in close proximity to the solid/liquid (organic) interface.

Fig. 19. The reaction profiles for Li/Na ion transport across the (a) $FePO_4/H_2O$ and (b) $FePO_4/EC$ interfaces. The energies for each step during the desolvation process and adsorption process are plotted as bars accordingly (blue bars for sodium-based, orange bars for Li-based). The desolvation process is endothermic, while the adsorption process is exothermic. (a-b) Reproduced with permission [111]. Copyright 2016, The Royal Society of Chemistry.
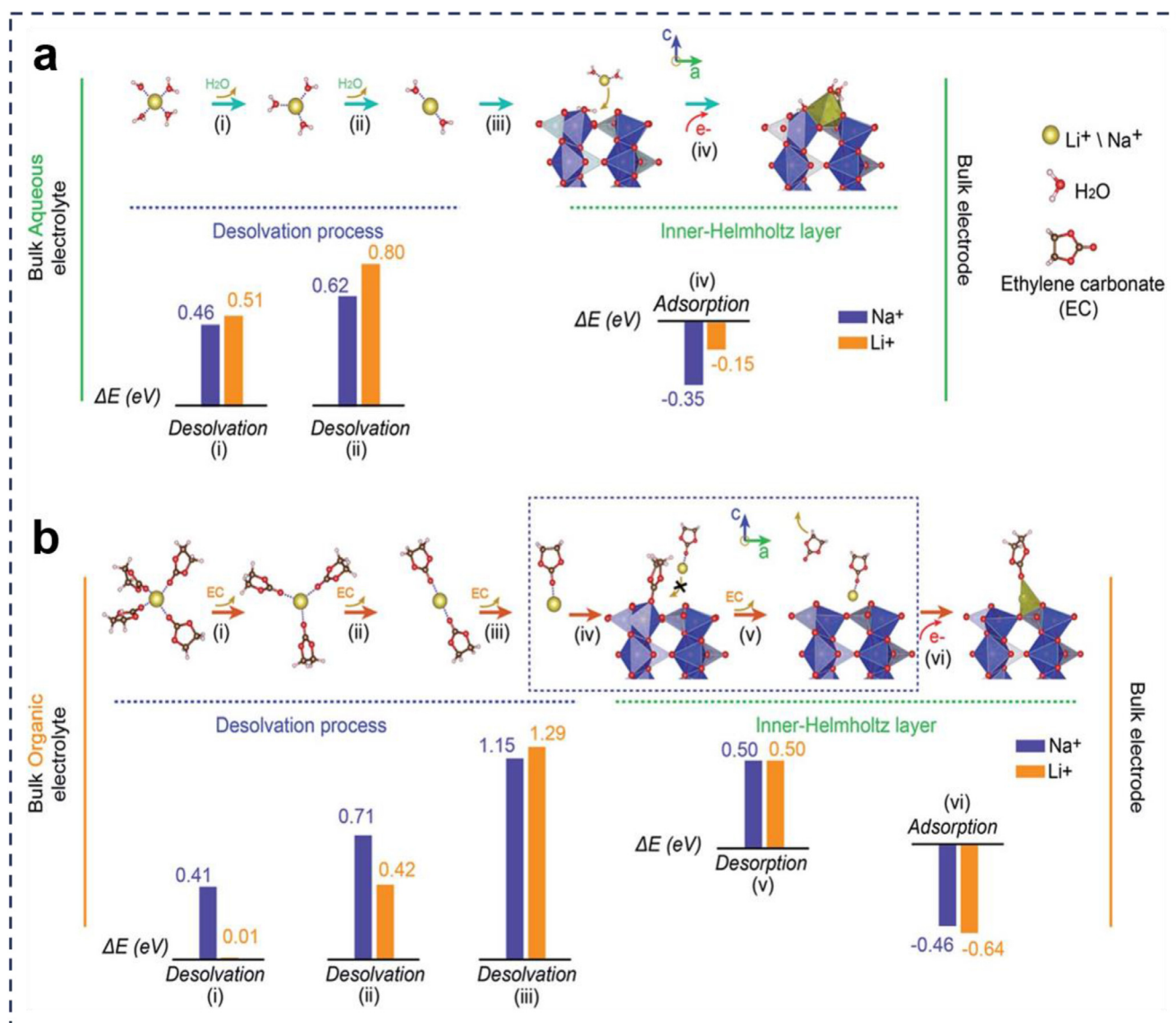
DFT study demonstrates that only one EC molecule can be adsorbed on a surface Na-site for NFP and a surface Fe-site on the [010] surface of $FePO_4$ (Fig. 19b(iv) and (vi)), while three H_2O and one H_2O molecules can be adsorbed on the surfaces of NFP and $FePO_4$ (Fig. 19a(iii) and (iv)). Calculations results (Bottom of Fig. 19b) of desolvation and adsorption energies for both Na^+ and Li^+ showed that Na^+ intercalation in an aqueous system was more competitive compared with an organic-exchanged system and co-intercalation of Li^+ was more significant in an organic system than in an aqueous system, which indicated that electrochemical-driven ion-exchange process showed superior for the transformation of NFP from LFP than organic-based electrochemical ion-exchange process. First-principles calculations was performed to investigate phase transformation, ionic diffusion, and charge transfer mechanisms of $KVOPO_4$ in KIBs. Based on the calculation results, three key messages were summed up: (i) in $KVOPO_4$, V was the redox center, while the O anion acted as a charge compensation medium between K and V, which suggested that when potassium ions were extracted, electrons firstly left O, and then compensated to O from V through the V-O bond (Fig. 20a); (ii) $KVOPO_4$ showed two phase transitions during K

ion extraction, taking place in the $0 \leq x \leq 0.5$ and $0.625 < x \leq 0.75$ ranges (Fig. 20b); (iii) 3D structure and 1D ion diffusion pathway endowed $KVOPO_4$ with a long cycle stability and superior rate capability (Fig. 20c-e) [37].

Excepting *in situ* XRD which can directly observe phase transition, the phase field model that replace the boundary conditions with partial differential equations at the interface to obtain the ordered evolution parameter of phase field, is mainly used to predict useful parameter. Tang et al. [228] applied the phase-field model to examine the effect of overpotential and crystallite size on the growth kinetics of competing phase transitions in LFP. Results suggested that low/high overpotentials were more conducive to crystalline-to-crystalline phase transition during the lithiated and delithiated process and at intermediate overpotentials, crystalline-to-amorphous transition was preferential. As particle size decreased, the overpotential range where amorphization dominates was broadened. Using a novel electrochemical phase-field model, Bai et al. [31] developed a novel theory that phase separation was dynamically suppressed during normal battery operation and decreasing the interfacial resistance at the active surface tended to further suppress
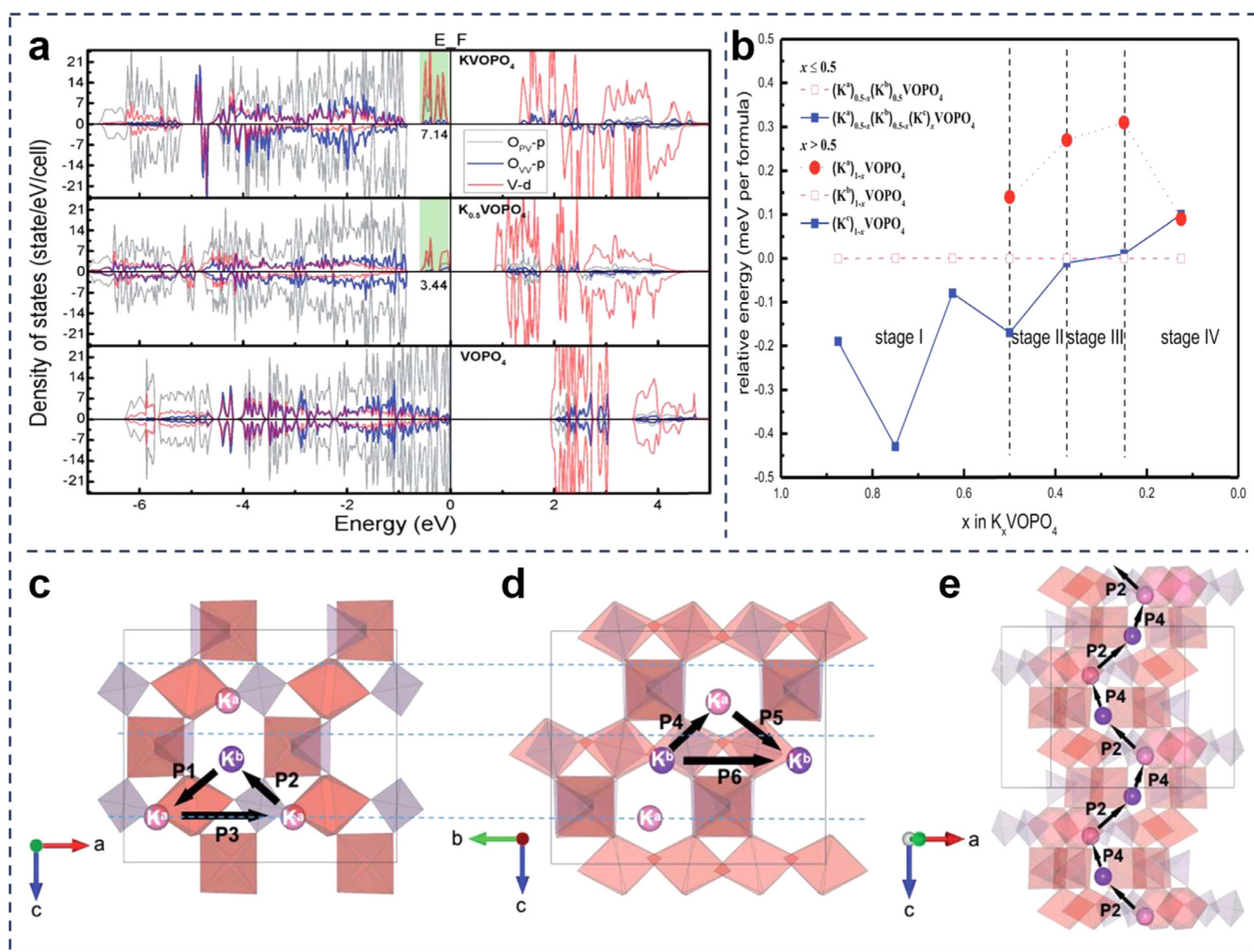
Fig. 20. (a) Partial density of states of V-3d and O-2p states in the KVOPO$_4$, K$_{0.5}$VOPO$_4$, and VOPO$_4$ phases. Inserted numbers, integrated occupancy between –0.6 and 0 eV; (b) Relative energies of different K$_{1-x}$VOPO$_4$ (0 < x < 1) configurations depending on different K positions. Red solid sphere, K preferred to locate at site-a; purple open squares, K preferred to locateat site-b; and blue solid squares, K preferred to locate at site-c. The site-b preferred phase is chosen as the reference state for all compositions; (c-e) Schematic representation of possible K migration pathways in the VOPO$_4$ framework from the view of (c) [010] and (d) [100] planes. (e) Spiral 1D diffusion pathway along the c-axis. (a-e) Reproduced with permission [37]. Copyright 2018, The Royal Society of Chemistry.

phase transformation, thus increasing the available active site for intercalation.

In summary, both advanced characterization technologies and theoretical calculation methods can provide deep insights for battery design and energy storage mechanism.

7. Conclusion and perspectives

Recent research findings summarized in this review suggest that phosphates and their composites have been widely investigated and are considered as promising electrodes for MIBs. In terms of structure, phosphate materials possess an open framework structure with large channels and cavities which endow them with good ionic conductivity and charge storage capacity, chemically stable structure arising from the relatively strong P-O covalent bonds in phosphates and low thermal expansion indicating high structural stability at high temperature.

There are still several problems faced by phosphates. For example, pure phosphates suffer low capacity and low electron conductivity arising from the PO$_4$$^{3-}$ groups. To compensate the disadvantages of phosphates and further improve electrochemical performance of phosphate-based electrode, strategies have been developed such as carbon decoration, ion doping, nanocrystallization, morphology modulation, and combination with other active materials, which can not only increase the active sites and provide additional pseudocapacitance, but achieve

high conductivity and shorten the diffusion distances. Nevertheless, side effects of these modification are also inevitable: The introduction of CNTs and graphene not only increases the cost and inactive quality, but decreases the bulk density which makes the specific volume capacity of phosphate much lower than that of lithium cobalt oxide, so the volume of resulting battery could be bulky making phosphate difficult to be applied in practice. Nano-sized active materials show lower tap density than micron-sized counterparts, which indicates the nano-sized electrodes suffer low volumetric energy density. Therefore, to develop suitable methods for current rechargeable batteries without compromising their inherent advantages is highly demanding [25].

Currently, phosphate synthesis process is limited to the experimental level, and large-scale fabrication methods are required for commercial applications. Generally, hydrothermal/solvothermal, chemical precipitation method, and ball milling method are common synthesis methods. In addition, electrospinning for 1D nanofibers, ALD for film deposition, and ultrasonic exfoliated bulk crystal into ultrathin NSs are employed. Although these approaches provided the possibility of synthesizing materials with improved performance, the majority of the approaches are too exotic for application in state-of-the-art batteries, and thus more feasible and simple synthesis is needed for large-scale production.

An incorporation of diverse nanostructures into phosphate-based materials will definitely benefit both structural superiority and intrinsic merits of the materials, for which an in-depth understanding of the

energy storage mechanism of the electrode and the internal structure characteristics of the electrode materials that can prompt reasonably design and synthesize high-performance electrode devices is inevitably needed [229].

Meanwhile, structural changes during the charge and discharge process needs to be controlled effectively. Repeated charge/discharge cycling may result in rapid structural degradation. Understanding the overpotential- and size-dependence of phase transformation behavior is important to design high stability crystal material for long term charge/discharge process. And study of lithium intercalation dynamics in NPs to phase separation could be helpful to design experiment for accurately controlling the nucleation and growth of material so as to suppress phase separation which can effectively improve rate capability and cycle life of electrodes [31,228].

In situ characterizations (such as *in situ* XRD, *in situ* scanning transmission X-ray microscopy, *in situ* TEM, and *in situ* nuclear magnetic resonance) as well as some advanced simulation technology (such as atomistic simulation methods and electrochemical phase-field model) have been applied to analyze electrochemical reaction mechanism and internal structure of these materials. However, there are few studies of phosphate based on theoretical calculations and *in-situ* characterization with high precision, and attentions is mainly focused on the exploration of LFP, much efforts should be made to a more widely and elaborate investigation, such as these isostructural compounds ($LiMPO_4$, M = Mn, Co and Ni).

A lot of research activities have been focused on improving the inherent properties of electrode materials to meet the demand for high-performance energy storage devices. However, to further establish the full cell of the metal phosphates-based composites for practical production, a better and deeper understanding is required in the surface and interface between the electrodes, electrolyte, and current collectors. Due to inductive effect in M-O-P, phosphate-based materials possess relatively high voltage where electrolyte is easy to decompose. Thus, the development of compatible, low-cost, and easy handling electrolyte is very important for the practical application of phosphates. Up to now, there have been several types of electrolyte (such as solid electrolytes, liquid electrolytes, and polymer electrolytes). Suitable electrolyte can not only improve the electrochemical performance of the battery, but also improve its safety and practicability.

Rational design of the architecture of electrode can effectively improve both the electron transfer rate and ionic conduction within the entire electrode, and ensure the uniform dispersion of active particles, thus achieving the best performance of batteries. Constantly renewing of electrode components to accommodate the evolving active materials is an efficient way to promote utility and scale production. To assemble electrodes, binder and conductive additives are necessary. Traditional binder PVDF is commonly used, but it shows a limited adhesion to the current collector, suffering binder aggregation during slurry preparation as well as in the final electrode film. Thus, binders with enhanced cohesion among electrode components and improved adhesion between electrode film and current collector are needed. Up to now, compared with PVDF, different types of binders have been studied with their own corresponding advantages such as low molecular weight spandex binder with superior adhesion of electrode to an Al current collector, uniformness of electrode morphology, and conservation of solvent during slurry preparation [25], environmentally benign binder, Carboxymethyl Cellulose (CMC) binder with better adhesion between the electrode particles, lower charge transfer resistance and activation energy as well as lower apparent diffusion activation energy [140,195,230,231], N-cyanoethyl polyethylenimine (CN-PEI) with excellent adhesion strength, outstanding dispersion capability, and higher ionic conductivity [232], sodium alginate (SA)-3,4-propylenedioxythiophene-2,5-dicarboxylic acid (ProDOT) binder with improved adhesion among the laminate, current collector, and LFP particles as well as mechanical stability [233], gelatin binder with enhanced adhesion between electrode material and Al current collector [234],

and Polyacrylate Latex with stronger adhesion strength, lower electrical resistances, and better charge transfer characteristics [235]. Other binder such as polystyrenesulfonate (PEDOT:PSS)/carboxymethyl cellulose (CMC) [236–238], perylene diimide polymer (PPDI) [239], polytetrafluoroethylene (PTFE) [240], and poly(N-vinylcarbazole) (PVK) [241], which were used for electrode preparation, lithium iron phosphate ($LiFePO4$) as cathodic active material, were reported to show superior performance to that of the PVDF binder. Besides, eco-friendly binders like poly vinyl acetate (PVAc) [242], Natural cellulose [243], Amphiphilic latex [244] are also investigated.

Another consideration factor for future development is the cost-effectiveness and easy degradability of metal phosphates. To meet the requirement of practical energy storage devices, besides considering the performance of the equipment itself, its cost and environmental compatibility should also be considered, especially in the new era of advocating green chemistry and green energy, indicating the benefits brought by the energy equipment itself should be far greater than its energy consumption which mainly comes from its production and spent treatment.

Declaration of Competing Interest

The authors declare that they have no known competing financial interests or personal relationships that could have appeared to influence the work reported in this paper.

Acknowledgments

References

[1] M. Armand, J.M. Tarascon, Building better batteries, Nature 451 (2008) 652–657.

[2] N. Choi, Z. Chen, S. Freunberger, X. Ji, Y. Sun, K. Amine, G. Yushin, L. Nazar, J. Cho, P. Bruce, Challenges facing lithium batteries and electrical double-layer capacitors, Angew. Chem. Int. Ed. 51 (2012) 9994–10024.

[3] M. Winter, R. Brodd, What are batteries, fuel cells, and supercapacitors? Cheminform 35 (2004) 4245.

[4] R. Hamidi, S. Ghasemi, S. Hosseini, Ultrasonic assisted synthesis of $Ni_3(VO_4)_2$-reduced graphene oxide nanocomposite for potential use in electrochemical energy storage, Ultrason. Sonochem. 62 (2020) 104869.

[5] G. Gourdin, A. Meehan, T. Jiang, P. Smith, D. Qu, Investigation of the impact of stacking pressure on a double-layer supercapacitor, J. Power Sources 196 (2011) 523–529.

[6] M. Whittingham, Lithium batteries and cathode materials, Chem. Rev. 35 (2004) 4271–4301.

[7] G. Hautier, A. Jain, S. Ong, B. Kang, C. Moore, R. Doe, G. Ceder, Phosphates as lithium-ion battery cathodes: an evaluation based on high-throughput ab initio calculations, Chem. Mater. 23 (2011) 3495–3508.

[8] W. Liu, H. Zhi, X. Yu, Recent progress in phosphorus based anode materials for lithium/sodium ion batteries, Energy Storage Mater. 16 (2019) 290–322.

[9] Y. Tian, G. Zeng, A. Rutt, T. Shi, H. Kim, J. Wang, J. Koettgen, Y. Sun, B. Ouyang, T. Chen, Z. Lun, Z. Rong, K. Persson, G. Ceder, Promises and challenges of next–generation "Beyond Li-ion" batteries for electric vehicles and grid decarbonization, Chem. Rev. 121 (2021) 1623–1669.

[10] Y. Meng, M. Arroyo-de Dompablo, Recent advances in first principles computational research of cathode materials for lithium-ion batteries, Acc. Chem. Res. 46 (2013) 1171–1180.

[11] J. Chen, L. Wei, A. Mahmood, Z. Pei, Z. Zhou, X. Chen, Y. Chen, Prussian blue, its analogues and their derived materials for electrochemical energy storage and conversion, Energy Storage Mater. 25 (2020) 585–612.

[12] S. Ong, V. Chevrier, G. Hautier, A. Jain, C. Moore, S. Kim, X. Ma, G. Ceder, Voltage, stability and diffusion barrier differences between sodium-ion and lithium-ion intercalation materials, Energ. Environ. Sci. 4 (2011) 3680–3688.

[13] John Longo, M. Kierkegaard, Peder Ballhausen, C., J. Ragnarsson, Ulf, a refinement of the structure of VO_2, Acta Chem. Scand. 24 (1970) 420–426.

[14] C. Masquelier, L. Croguennec, Polyanionic (phosphates, silicates, sulfates) frameworks as electrode materials for rechargeable Li (or Na) teries, Chem. Rev. 113 (2013) 6552–6591.

[15] Y. Wang, G. Cao, Developments in nanostructured cathode materials for high-performance lithium-ion batteries, Adv. Mater. 20 (2008) 2251–2269.

[16] P. Herle, B. Ellis, N. Coombs, L. Nazar, Nano-network electronic conduction in iron and nickel olivine phosphates, Nat. Mater. 3 (2004) 147–152.

[17] N. Septiani, Y. Kaneti, K. Fathoni, K. Kani, A. Allah, B. Yuliarto, H.Dipojono Nugraha, Z. Alothman, D. Golberg, Y. Yamauchi, Self-assembly of two-dimensional bimetallic nickel–cobalt phosphate nanoplates into one-dimensional porous chain-like architecture for efficient oxygen evolution reaction, Chem. Mater. 32 (2020) 7005–7018.

[18] Y. Wang, W. Zhang, L. Chen, S. Shi, J. Liu, Quantitative description on structure–property relationships of Li-ion battery materials for high-throughput computations, Sci. Technol. Adv. Mat. 18 (2017) 134–146.

[19] Y. Fang, J. Zhang, L. Xiao, X. Ai, Y. Cao, H. Yang, Phosphate framework electrode materials for sodium ion batteries, Adv. Sci. 4 (2017) 1600392.

[20] N. Wulan Septiani, Y. Kaneti, K. Fathoni, J. Wang, Y. Ide, B. Yuliarto, H.Dipojono Nugraha, A. Nanjundan, D. Golberg, Y. Bando, Y. Yamauchi, Self-assembly of nickel phosphate-based nanotubes into two-dimensional crumpled sheet-like architectures for high-performance asymmetric supercapacitors, Nano Energy 67 (2020) 104270.

[21] P. Mei, Y. Kaneti, M. Pramanik, T. Takei, Ö. Dag, Y. Sugahara, Y. Yamauchi, Two-dimensional mesoporous vanadium phosphate nanosheets through liquid crystal templating method toward supercapacitor application, Nano Energy 52 (2018) 336–344.

[22] R. Murugavel, A. Choudhury, M. Walawalkar, R. Pothiraja, C. Rao, Metal complexes of organophosphate esters and open-framework metal phosphates: synthesis, structure, transformations, and applications, Chem. Rev. 108 (2008) 3549–3655.

[23] D. Zhang, L. Hu, Y. Sun, J. Piao, X. Tao, Y. Xu, A. Cao, L. Wan, Construction of uniform transition-metal phosphate nanoshells and their potential for improving Li-ion battery performance, J. Mater. Chem. A 6 (2018) 8992–8999.

[24] C. Patridge, C. Jaye, T. Abtew, B. Ravel, D. Fischer, A. Marschilok, P. Zhang, K. Takeuchi, E. Takeuchi, S. Banerjee, An X-ray absorption spectroscopy study of the cathodic discharge of Ag₂VO₂PO₄: geometric and electronic structure characterization of intermediate phases and mechanistic insights, J. Phys. Chem. C 115 (2011) 14437–14447.

[25] Y. Lee, J. Min, K. Lee, S. Kim, S. Park, J. Choi, Low molecular weight spandex as a promising polymeric binder for LiFePO₄ electrodes, Adv. Energy Mater. 7 (2017) 1602147.

[26] C. Fasciani, S. Panero, J. Hassoun, B. Scrosati, Novel configuration of poly(vinylidenedifluoride)-based gel polymer electrolyte for application in lithium-ion batteries, J. Power Sources 294 (2015) 180–186.

[27] I. Osada, S. Hosseini, S. Jeong, S. Passerini, Novel ternary polymer electrolytes based on poly(lactic acid) from sustainable sources, ChemElectroChem 4 (2017) 463–467.

[28] J. Ni, L. Zhang, S. Fu, S. Savilov, S. Aldoshin, L. Lu, A review on integrating nano-carbons into polyanion phosphates and silicates for rechargeable lithium batteries, Carbon 92 (2015) 15–25.

[29] W. Yang, J. Liu, X. Zhang, L. Chen, Y. Zhou, Z. Zou, Ultrathin LiFePO₄ nanosheets self-assembled with reduced graphene oxide applied in high rate lithium ion batteries for energy storage, Appl. Energ. 195 (2017) 1079–1085.

[30] S. Adams, Ultrafast lithium migration in surface modified LiFePO₄ by heterogeneous doping, Appl. Energ. 90 (2012) 323–328.

[31] P. Bai, D. Cogswell, M. Bazant, Suppression of phase separation in LiFePO₄ nanoparticles during battery discharge, Nano Lett. 11 (2011) 4890–4896.

[32] D. Wang, X. Bie, Q. Fu, D. Dixon, N. Bramnik, Y. Hu, F. Fauth, Y. Wei, H. Ehrenberg, G. Chen, F. Du, Sodium vanadium titanium phosphate electrode for symmetric sodium-ion batteries with high power and long lifespan, Nat. Commun. 8 (2017) 15888.

[33] N. Voronina, J. Jo, J. Choi, C. Jo, J. Kim, S. Myung, Nb-Doped titanium phosphate for sodium storage: electrochemical performance and structural insights, J. Mater. Chem. A 7 (2019) 5748–5759.

[34] K. Chihara, A. Katogi, K. Kubota, S. Komaba, KVPO₄F and KVOPO₄ toward 4 volt-class potassium-ion batteries, Chem. Commun. 53 (2017) 5208–5211.

[35] L. Zhang, S. Dou, H. Liu, Y. Huang, X. Hu, Symmetric Electrodes for Electrochemical Energy-Storage Devices, Adv. Sci. 3 (2016) 1600115.

[36] Z. Wei, D. Wang, M. Li, Y. Gao, C. Wang, G. Chen, F. Du, Fabrication of hierarchical potassium titanium phosphate spheroids: a host material for sodium-ion and potassium-ion storage, Adv. Energy Mater. 8 (2018) 1801102.

[37] R. Lian, D. Wang, X. Ming, R. Zhang, Y. Wei, J. Feng, X. Meng, G. Chen, Phase transformation, ionic diffusion, and charge transfer mechanisms of KVOPO₄ in potassium ion batteries: first-principles calculations, J. Mater. Chem. A 6 (2018) 16228–16234.

[38] A. Varzi, C. Ramirez-Castro, A. Balducci, S. Passerini, Performance and kinetics of LiFePO₄–carbon bi-material electrodes for hybrid devices: A comparative study between activated carbon and multi-walled carbon nanotubes, J. Power Sources 273 (2015) 1016–1022.

[39] H. Gao, I.D. Seymour, S. Xin, L. Xue, G. Henkelman, J. Goodenough, Na₃MnZr(PO₄)₃: a high-voltage cathode for sodium batteries, J. Am. Chem. Soc. 140 (2018) 18192–18199.

[40] A. Padhi, K. Nanjundaswamy, J. Goodenough, Phospho-olivines as positive-electrode materials for rechargeable lithium batteries, J. Electrochem. Soc. 144 (1997) 1188–1194.

[41] D. Morgan, A. Ven, G. Ceder, Li conductivity in LiₓMPO₄ (M = Mn, Fe, Co, Ni) olivine materials, Electrochem. Solid-State Lett. 7 (2004) A30.

[42] M. Kim, S. Lee, B. Kang, High energy density polyanion electrode material: LiVPO₄O₁₋ₓFₓ (x ≈ 0.25) with tavorite structure, Chem. Mater. 29 (2017) 4690–4699.

[43] N. Goubard-Bretesché, E. Kemnitz, N. Pinna, Fluorolytic sol–gel route and electrochemical properties of polyanionic transition-metal phosphate fluorides, Chem. Eur. J. 25 (2019) 6189–6195.

[44] R. Tripathi, G. Popov, B. Ellis, A. Huq, L. Nazar, Lithium metal fluorosulfate polymorphs as positive electrodes for Li-ion batteries: synthetic strategies and effect of cation ordering, Energ. Environ. Sci. 5 (2012) 6238–6246.

[45] O. Yakubovich, O. Karimova, O. Mel'nikov, The mixed anionic framework in the structure of Na₂{MnF[PO₄]}, Acta Crystallogr. Sect. C 53 (1997) 395–397.

[46] M. Dutreilh, C. Chevalier, M. El-Ghozzi, D. Avignant, J. Montel, Synthesis and crystal structure of a new lithium nickel fluorophosphate Li₂[NiF(PO₄)] with an ordered mixed anionic framework, J. Solid State Chem. 142 (1999) 1–5.

[47] E. Dumont-Botto, C. Bourbon, S. Patoux, P. Rozier, M. Dolle, Synthesis by Spark plasma sintering: a new way to obtain electrode materials for lithium ion batteries, J. Power Sources 196 (2011) 2274–2278.

[48] S. Fedotov, D. Aksyonov, A. Samarin, O. Karakulina, J. Hadermann, N.Khasanova K.JStevenson, A. Abakumov, E. Antipov, Tuning the crystal structure of A₂CoPO₄F (A = Li, Na) fluoride-phosphates: a new layered polymorph of LiNaCoPO₄F, Eur. J. Inorg. Chem. 2019 (2019) 4365–4372.

[49] B. Ellis, W. Makahnouk, Y. Makimura, K. Toghill, L. Nazar, A multifunctional 3.5V iron-based phosphate cathode for rechargeablebatteries, Nat. Mater. 6 (2007) 749–753.

[50] F. Sanz, C. Parada, C. Ruíz-Valero, Crystal growth, crystal structure and magnetic properties of disodium cobalt fluorophosphate, J. Mater. Chem. 11 (2001) 208–211.

[51] R. Gover, A. Bryan, P. Burns, J. Barker, The electrochemical insertion properties of sodium vanadium fluorophosphate, Na₃V₂(PO₄)₂F₃, Solid State Ionics 177 (2006) 1495–1500.

[52] G. Mattei, J. Dagdelen, M. Bianchini, A. Ganose, A. Jain, E. Suard, F. Fauth, C. Masquelier, L. Croguennec, G. Ceder, K. Persson, P. Khalifah, Enumeration as a tool for structure solution: a materials genomic approach to solving the cation-ordered structure of Na₃V₂(PO₄)₂F₃, Chem. Mater. 32 (2020) 8981–8992.

[53] D. Semykina, I. Yakovlev, O. Lapina, A. Kabanov, N. Kosova, Crystal structure and migration paths of alkaline ions in NaVPO₄F, Phys. Chem. Chem. Phys. 22 (2020) 15876–15884.

[54] T. Amos, A. Yokochi, A. Sleight, Phase transition and negative thermal expansion in tetragonal NbOPO₄, J. Solid State Chem. 141 (1998) 303–307.

[55] J. Lee, D. Son, C. Kim, B. Park, Electrochemical properties of tin phosphates with various mesopore ratios, J. Power Sources 172 (2007) 908–912.

[56] W. Lu, L. Cong, Y. Liu, J. Liu, A. Mauger, C. Julien, L. Sun, H. Xie, Pseudocapacitance controlled fast-charging and long-life lithium ion battery achieved via a 3D mutually embedded VPO₄/rGO electrode, J. Alloys Compd. 812 (2020) 152135.

[57] C. Sun, J. Hu, P. Wang, X. Cheng, S. Lee, Y. Wang, Li₃PO₄ matrix enables a long cycle life and high energy efficiency bismuth-based battery, Nano Lett. 16 (2016) 5875–5882.

[58] O. Toprakci, H. Toprakci, L. Ji, X. Zhang, Fabrication and electrochemical characteristics of LiFePO₄ powders for lithium-ion batteries, KONA Powder Part. J. 28 (2010) 50–73.

[59] B. Ellis, L. Perry, D. Ryan, L. Nazar, Small polaron hopping in LiₓFePO₄ solid solutions: coupled lithium-ion and electron mobility, J. Am. Chem. Soc. 128 (2006) 11416–11422.

[60] R. Satish, V. Aravindan, W. Ling, S. Madhavi, Carbon-coated Li₃V₂(PO₄)₃ as insertion type electrode for lithium-ion hybrid electrochemical capacitors: an evaluation of anode and cathodic performance, J. Power Sources 281 (2015) 310–317.

[61] J. Ni, Y. Han, L. Gao, L. Lu, One-pot synthesis of CNT-wired LiCo₀.₅Mn₀.₅PO₄ nanocomposites, Electrochem. Commun. 31 (2013) 84–87.

[62] M. Theivanayagam, T. Hu, R. Ziebarth, S. Santhany, J. Goss, H. Maeda, A. Patel, M. Behr, M. Lowe, A. Leugers, Improvement in hydrophobicity of olivine lithium manganese iron phosphate cathodes by SiF₄ treatment for lithium-ion batteries, Solid State Ionics 281 (2015) 82–88.

[63] H. Li, Y. Chen, L. Chen, H. Jiang, Y. Wang, H. Wang, G. Li, Y. Li, Y. Yuan, Improved cycling and high rate performance of core-shell LiFe₁/₃Mn₁/₃Co₁/₃PO₄/carbon nanocomposites for lithium-ion batteries: effect of the carbon source, Electrochim. Acta 143 (2014) 407–414.

[64] X. Rui, Q. Yan, M. Skyllas-Kazacos, T. Lim, Li₃V₂(PO₄)₃ cathode materials for lithium-ion batteries: a review, J. Power Sources 258 (2014) 19–38.

[65] Y. Wang, X. Zhang, W. He, W. Yang, C. Wei, Porous isomeric Li₂.₅Na₀.₅V₂(PO₄)₃ wide voltage cathode for high-performance lithium-ion batteries synthesized through a colloid chemical method, ChemElectroChem 6 (2019) 2638–2647.

[66] X. Li, A. Elshahawy, C. Guan, J. Wang, Metal phosphides and phosphates-based electrodes for electrochemical supercapacitors, Small 13 (2017) 1701530.

[67] J. Patete, M. Scofield, V. Volkov, C. Koenigsmann, Y. Zhang, A. Marschilok, X. Wang, J. Bai, J. Han, L. Wang, F. Wang, Y. Zhu, J. Graetz, S. Wong, Ambient synthesis, characterization, and electrochemical activity of LiFePO₄ nanomaterials derived from iron phosphate intermediates, Nano Res. 8 (2015) 2573–2594.

[68] T. Zhang, X. Cheng, Q. Zhang, Y. Lu, G. Luo, Construction of a cathode using amorphous FePO₄ nanoparticles for a high-power/energy-density lithium-ion battery with long-term stability, J. Power Sources 324 (2016) 52–60.

[69] W. Lai, Y. Wang, Y. Wang, M. Wu, J. Wang, H. Liu, S. Chou, J. Chen, S. Dou, Morphology tuning of inorganic nanomaterials grown by precipitation through control of electrolytic dissociation and supersaturation, Nat. Chem. 11 (2019) 695–701.

[70] Y. Ma, X. Li, S. Sun, X. Hao, Y. Wu, Synthesize of graphene-LiFePO₄ composite porous microsphere with the enhanced rate performance, Int. J. Electrochem. Sc. 8 (2013) 2842–2848.

[71] F. Omar, A. Numan, N. Duraisamy, S. Bashir, K. Ramesh, S. Ramesh, Ultrahigh capacitance of amorphous nickel phosphate for asymmetric supercapacitor applications, RSC Adv. 6 (2016) 76298–76306.

[72] J. Theerthagiri, K. Thiagarajan, B. Senthilkumar, Z. Khan, R. Senthil, P. Arunachalam, J. Madhavan, M. Ashokkumar, Synthesis of hierarchical cobalt phosphate nanoflakes and their enhanced electrochemical performances for supercapacitor applications, ChemistrySelect 2 (2017) 201–210.

[73] H. Li, H. Yu, J. Zhai, L. Sun, H. Yang, S. Xie, Self-assembled 3D cobalt phosphate octahydrate architecture for supercapacitor electrodes, Mater. Lett. 152 (2015) 25–28.

[74] H. Pang, Z. Yan, W. Wang, J. Chen, J. Zhang, H. Zheng, Facile fabrication of $NH_4CoPO_4 \cdot H_2O$ nano/microstructures and their primarily application as electrochemical supercapacitor, Nanoscale 4 (2012) 5946.

[75] V. Nithya, B. Hanitha, S. Surendran, D. Kalpana, R.Kalai Selvan, Effect of pH on the sonochemical synthesis of $BiPO_4$ nanostructures and its electrochemical properties for pseudocapacitors, Ultrason. Sonochem. 22 (2015) 300–310.

[76] C. Yang, L. Dong, Z. Chen, H. Lu, High-performance all-solid-state supercapacitor based on the assembly of graphene and manganese(II) phosphate nanosheets, J. Phys. Chem. C 118 (2014) 18884–18891.

[77] B. Li, H. Pang, H. Xue, Fe-based phosphate nanostructures for supercapacitors, Chin. Chem. Lett. (2020).

[78] J. Liu, M. Banis, Q. Sun, A. Lushington, R. Li, T. Sham, X. Sun, Rational design of atomic-layer-deposited $LiFePO_4$ as a high-performance cathode for lithium-ion batteries, Adv. Mater. 26 (2014) 6472–6477.

[79] S. Han, J. Wang, S. Li, D. Wu, X. Feng, Graphene aerogel supported $Fe_5(PO_4)_4(OH)_3 \cdot 2H_2O$ microspheres as high performance cathode for lithium ion batteries, J. Mater. Chem. A 2 (2014) 6174–6179.

[80] M. Chen, C. Du, B. Song, K. Xiong, G. Yin, P. Zuo, X. Cheng, High-performance $LiFePO_4$ cathode material from $FePO_4$ microspheres with carbon nanotube networks embedded for lithium ion batteries, J. Power Sources 223 (2013) 100–106.

[81] M. Mouyane, J. Ruiz, M. Artus, S. Cassaignon, J. Jolivet, G. Caillon, C. Jordy, K. Driesen, J. Scoyer, L. Stievano, J. Olivier-Fourcade, J. Jumas, Carbothermal synthesis of Sn-based composites as negative electrode for lithium-ion batteries, J. Power Sources 196 (2011) 6863–6869.

[82] T. Kerr, Highly reversible Li insertion at 4 V in ε-$VOPO_4$/α-$LiVOPO_4$ cathodes, Electrochem. Solid-State Lett. 3 (1999) 460.

[83] Y. Zhao, L. Peng, B. Liu, G. Yu, Single-crystalline $LiFePO_4$ nanosheets for high-rate Li-ion batteries, Nano Lett. 14 (2014) 2849–2853.

[84] A. Murugan, T. Muraliganth, P. Ferreira, A. Manthiram, Dimensionally modulated, single-crystalline $LiMPO_4$ (M= Mn, Fe, Co, and Ni) with nano-thumblike shapes for high-power energy storage, Inorg. Chem. 48 (2009) 946–952.

[85] K. Cui, S. Hu, Y. Li, Nitrogen-doped graphene nanosheets decorated $Li_3V_2(PO_4)_3$/C nanocrystals as high-rate and ultralong cycle-life cathode for lithium-ion batteries, Electrochim. Acta 210 (2016) 45–52.

[86] C. Karegeya, A. Mahmoud, B. Vertruyen, F. Hatert, R. Hermann, R. Cloots, F. Boschini, One-step hydrothermal synthesis and electrochemical performance of sodium-manganese-iron phosphate as cathode material for Li-ion batteries, J. Solid State Chem. 253 (2017) 389–397.

[87] B. Ellis, W. Makahnouk, W. Rowan-Weetaluktuk, D. Ryan, L. Nazar, Crystal structure and electrochemical properties of A_2MPO_4F fluorophosphates (A = Na, Li; M = Fe, Mn, Co, Ni), Chem. Mater. 22 (2010) 1059–1070.

[88] P. Simon, Y. Gogotsi, B. Dunn, Where do batteries end and supercapacitors begin? Science 343 (2014) 1210.

[89] X. Sun, Y. Xu, Fe excess in hydrothermally synthesized $LiFePO_4$, Mater. Lett. 84 (2012) 139–142.

[90] V. Sumanov, D. Aksyonov, O. Drozhzhin, I. Presniakov, A. Sobolev, I. Glazkova, A. Tsirlin, D. Rupasov, A. Senyshyn, I. Kolesnik, K. Stevenson, E. Antipov, A. Abakumov, Hydrotriphylites" $Li_{1-x}Fe_{1+x}(PO_4)_{1-y}(OH)_{4y}$ as cathode materials for Li-ion batteries, Chem. Mater. 31 (2019) 5035–5046.

[91] A. Örnek, Positive effects of a particular type of microwave-assisted methodology on the electrochemical properties of olivine $LiMPO_4$ (M=Fe, Co and Ni) cathode materials, Chem. Eng. J. 331 (2018) 501–509.

[92] Y. Xie, F. Song, C. Xia, H. Du, Preparation of carbon-coated lithium iron phosphate/titanium nitride for a lithium-ion supercapacitor, New J. Chem. 39 (2014) 604–613.

[93] S. Yang, M. Hu, L. Xi, R. Ma, Y. Dong, C. Chung, Solvothermal synthesis of monodisperse $LiFePO_4$ micro hollow spheres as high performance cathode material for lithium ion batteries, ACS Appl. Mater. Inter. 5 (2013) 8961–8967.

[94] N. Zhou, Y. Liu, J. Li, E. Uchaker, S. Liu, K. Huang, G. Cao, Synthesis and characterization of high power $LiFePO_4$/C nano-plate thin films, J. Power Sources 213 (2012) 100–105.

[95] A. Örnek, The synthesis of novel $LiNiPO_4$ core and Co_3O_4/CoO shell materials by combining them with hard-template and solvothermal routes, J. Colloid Interface Sci. 504 (2017) 468–478.

[96] B. Ellis, W. Kan, W. Makahnouk, L. Nazar, Synthesis of nanocrystals and morphology control of hydrothermally prepared $LiFePO_4$, J. Mater. Chem. 17 (2007) 3248–3254.

[97] X. Liu, J. Huang, Q. Zhang, X. Liu, H. Peng, W. Zhu, F. Wei, N-methyl-2-pyrrolidone-assisted solvothermal synthesis of nanosize orthorhombic lithium iron phosphate with improved Li-storage performance, J. Mater. Chem. 22 (2012) 18908–18914.

[98] C. Karegeya, A. Mahmoud, R. Cloots, B. Vertruyen, F. Boschini, Hydrothermal synthesis in presence of carbon black: particle-size reduction of iron hydroxyl phosphate hydrate for Li-ion battery, Electrochim. Acta 250 (2017) 49–58.

[99] Y. Lu, T. Wang, X. Li, G. Zhang, H. Xue, H. Pang, Synthetic methods and electrochemical applications for transition metal phosphide nanomaterials, RSC Adv. 6 (2016) 87188–87212.

[100] Q. Wang, N. Evans, S. Zakeeruddin, I. Exnar, M. Graetzel, Molecular wiring of insulators: charging and discharging electrode materials for high-energy lithium-ion batteries by molecular charge transport layers, J. Am. Chem. Soc. 129 (2007) 3163–3167.

[101] K. Kim, Y. Cho, D. Kam, H. Kim, J. Lee, Effects of organic acids as reducing agents in the synthesis of $LiFePO_4$, J. Alloys Compd. 504 (2010) 166–170.

[102] K. Wu, J. Yang, Synthesis of carbon coated $Li_3V_2(PO_4)_3$/reduced graphene oxide composite for high-performance lithium ion batteries, Mater. Res. Bull. 48 (2013) 435–439.

[103] J. Kim, H. Kim, S. Myung, J. Yoo, S. Lee, Exceptional effect of glassy lithium fluorophosphate on Mn-rich olivine cathode material for high-performance Li ion batteries, J. Power Sources 374 (2018) 55–60.

[104] K. Wu, G. Hu, K. Du, Z. Peng, Y. Cao, Synthesis and characterization of high-rate $LiMn_{1/3}Fe_{2/3}PO_4$/C composite using nano-$MnFe_2O_4$ as precursor, Mater. Lett. 152 (2015) 217–219.

[105] G. Pagot, F. Bertasi, G. Nawn, E. Negro, G. Carraro, D. Barreca, C. Maccato, S. Polizzi, V. Di Noto, High-performance olivine for lithium batteries: effects of Ni/Co doping on the properties of $LiFe_{\alpha}Ni_{\beta}Co_{\gamma}PO_4$ cathodes, Adv. Funct. Mater. 25 (2015) 4032–4037.

[106] R. Klee, P. Lavela, M. Aragón, R. Alcántara, J. Tirado, Enhanced high-rate performance of manganese substituted $Na_3V_2(PO_4)_3$/C as cathode for sodium-ion batteries, J. Power Sources 313 (2016) 73–80.

[107] M. Aragón, P. Lavela, G. Ortiz, J. Tirado, Benefits of chromium substitution in $Na_3V_2(PO_4)_3$ as a potential candidate for sodium-ion batteries, ChemElectroChem 2 (2015) 995–1002.

[108] P. Sun, X. Zhao, R. Chen, T. Chen, L. Ma, Q. Fan, H. Lu, Y. Hu, Z. Tie, Z. Jin, Q. Xu, J. Liu, $Li_3V_2(PO_4)_3$ encapsulated flexible free-standing nanofabric cathodes for fast charging and long life-cycle lithium-ion batteries, Nanoscale 8 (2016) 7408–7415.

[109] M. Aragón, P. Lavela, G. Ortiz, R. Alcántara, J. Tirado, Induced rate performance enhancement in off-stoichiometric $Na_{3+3x}V_{2-x}(PO_4)_3$ with potential applicability as the cathode for sodium-ion batteries, Chem. Eur. J. 23 (2017) 7345–7352.

[110] Y. Fang, Q. Liu, L. Xiao, X. Ai, H. Yang, Y. Cao, High-performance olivine $NaFePO_4$ microsphere cathode synthesized by aqueous electrochemical displacement method for sodium ion batteries, ACS Appl. Mater. Inter. 7 (2015) 17977–17984.

[111] W. Tang, X. Song, Y. Du, C. Peng, M. Lin, S. Xi, B. Tian, J. Zheng, Y. Wu, F. Pan, K. Loh, High-performance $NaFePO_4$ formed by aqueous ion-exchange and its mechanism for advanced sodium ion batteries, J. Mater. Chem. A 4 (2016) 4882–4892.

[112] X. Wu, Y. Guo, J. Su, J. Xiong, Y. Zhang, L. Wan, Carbon-nanotube-decorated nano-$LiFePO_4@C$ cathode material with superior high-rate and low-temperature performances for lithium-ion batteries, Adv. Energy Mater. 3 (2013) 1155–1160.

[113] L.Xiangwu Zhang, Ozan Toprakci, Yinzheng Liang, M. Alcoutlabi, Electrospun nanofiber-based anodes, cathodes, and separators for advanced lithium-ion batteries, Polym. Rev. 51 (2011) 239–264.

[114] S. Wei, J. Yao, B. Shi, 1D highly porous $Li_3V_2(PO_4)_3$/C nanofibers as superior high-rate and ultralong cycle-life cathode material for electrochemical energy storage, Solid State Ionics 305 (2017) 36–42.

[115] J. Shao, X. Li, J. Wei, H. Pang, C. Chen, Synthesis of iron phosphate and their composites for lithium/sodium ion batteries, Adv. Sustain. Syst. 2 (2018) 1700154.

[116] T. Ma, Z. Yuan, Metal phosphonate hybrid mesostructures: environmentally friendly multifunctional materials for clean energy and other applications, Chemsuschem 4 (2011) 1407–1419.

[117] L. Wang, Q. Wang, W. Jia, S. Chen, P. Gao, J. Li, Li metal coated with amorphous Li_3PO_4 via magnetron sputtering for stable and long-cycle life lithium metal batteries, J. Power Sources 342 (2017) 175–182.

[118] M. Cabello, G. Ortiz, M. López, P. Lavela, R. Alcántara, J. Tirado, Self-assembled $Li_4Ti_5O_{12}$/TiO_2/Li_3PO_4 for integrated Li–ion microbatteries, Electrochem. Commun. 56 (2015) 61–64.

[119] S. Chung, J. Bloking, Y. Chiang, Electronically conductive phospho-olivines as lithium storage electrodes, Nat. Mater. 1 (2002) 123–128.

[120] K.A. Padhi, Phospho-olivines as positive-electrode materials for rechargeable lithium batteries, J. Electrochem. Soc. 144 (1997) 1188–1194.

[121] A. Padhi, K. Nanjundaswamy, C. Masquelier, S. Okada, J. Goodenough, Effect of structure on Fe^{3+}/Fe^{2+} redox couple in iron phosphates, J. Electrochem. Soc. 144 (1997) 1609–1613.

[122] M. Lee, D. Chang, Allocative efficiency of high-power Li-ion batteries from automotive mode (AM) to storage mode (SM), Renew. Sust. Energ. Rev. 64 (2016) 60–67.

[123] S. Nishimura, G. Kobayashi, K. Ohoyama, R. Kanno, M. Yashima, A. Yamada, Experimental visualization of lithium diffusion in Li_xFePO_4, Nat. Mater. 7 (2008) 707–711.

[124] Tsuda Takashi, Ando Nobuo, Nakamura Susumu, Ishihara Yuuta, Hayashi Narumi, Improvement of high-rate discharging performance of $LiFePO_4$ cathodes by forming micrometer-sized through-holed electrode structures with a pico-second pulsed laser, Electrochim. Acta 296 (2019) 27–38.

[125] A. Vu, A. Stein, Lithium iron phosphate spheres as cathode materials for high power lithium ion batteries, J. Power Sources 245 (2014) 48–58.

[126] H. Zhang, Y. Xu, C. Zhao, X. Yang, Q. Jiang, Effects of carbon coating and metal ions doping on low temperature electrochemical properties of $LiFePO_4$ cathode material, Electrochim. Acta 83 (2012) 341–347.

[127] R. Ruffo, C. Mari, F. Morazzoni, F. Rosciano, R. Scotti, Electrical and electrochemical behaviour of several $LiFexCo_{1-x}PO_4$ solid solutions as cathode materials for lithium ion batteries, Ionics 13 (2007) 287–291.

[128] J. Hwang, K. Kong, W. Chang, E. Jo, K. Nam, J. Kim, New liquid carbon dioxide based strategy for high energy/power density $LiFePO_4$, Nano Energy 36 (2017) 398–410.

[129] W. Liu, J. Tu, Y. Qiao, J. Zhou, C. Gu, Optimized performances of core–shell structured LiFePO$_4$/C nanocomposite, J. Power Sources 196 (2011) 7728–7735.

[130] X. Zhang, Z. Bi, W. He, G. Yang, H. Liu, Y. Yue, Fabricating high-energy quantum dots in ultra-thin LiFePO$_4$ nanosheets using a multifunctional high-energy biomolecule—ATP, Energ. Environ. Sci. 7 (2014) 2285–2294.

[131] A. Yasmin, M. Shehzad, X. Ding, M. Deng, J. Liao, Q. Hu, X. He, S. Wang, C. Chen, Biomimetic mitochondrial nanostructures boost the battery performance, Sustain. Energ. Fuels 3 (2019) 2015–2023.

[132] Y. Liu, D. Liu, Q. Zhang, D. Yu, J. Liu, G. Cao, Lithium iron phosphate/carbon nanocomposite film cathodes for high energy lithium ion batteries, Electrochim. Acta 56 (2011) 2559–2565.

[133] D. Xu, X. Chu, Y. He, Z. Ding, B. Li, W. Han, H. Du, F. Kang, Enhanced performance of interconnected LiFePO$_4$/C microspheres with excellent multiple conductive network and subtle mesoporous structure, Electrochim. Acta 152 (2015) 398–407.

[134] A. Varzi, D. Bresser, J. von Zamory, F. Müller, S. Passerini, ZnFe$_2$O$_4$-C/LiFePO$_4$-CNT: a novel high-power lithium-ion battery with excellent cycling performance, Adv. Energy Mater. 4 (2014) 1400054.

[135] S. Brutti, J. Hassoun, B. Scrosati, C. Lin, H. Hsieh, A high power Sn–C/C–LiFePO$_4$ lithium ion battery, J. Power Sources 217 (2012) 72–76.

[136] Y. Wu, Z. Wen, J. Li, Hierarchical carbon-coated LiFePO$_4$ nanoplate microspheres with high electrochemical performance for Li-ion batteries, Adv. Mater. 23 (2011) 1126–1129.

[137] D. Saikia, J. Deka, C. Chou, C. Lin, Y. Yang, H. Kao, Encapsulation of LiFePO$_4$ nanoparticles into 3D interpenetrating ordered mesoporous carbon as a high-performance cathode for lithium-ion batteries exceeding theoretical capacity, ACS Appl. Energy Mater. 2 (2019) 1121–1133.

[138] J. Zhang, N. Nie, Y. Liu, J. Wang, W. Li, Boron and nitrogen codoped carbon layers of LiFePO$_4$ improve the high-rate electrochemical performance for lithium ion batteries, ACS Appl. Mater. Inter. 7 (2015) 20134.

[139] L. Borchardt, M. Oschatz, S. Kaskel, Tailoring porosity in carbon materials for supercapacitor applications, Mater. Horiz. 1 (2014) 157–168.

[140] L. Qiu, Z. Shao, D. Wang, W. Wang, F. Wang, J. Wang, Enhanced electrochemical properties of LiFePO$_4$ (LFP) cathode using the carboxymethyl cellulose lithium (CMC-Li) as novel binder in lithium-ion battery, Carbohydr. Polym. 111 (2014) 588–591.

[141] X. Wei, X. Jiang, J. Wei, S. Gao, Functional groups and pore size distribution do matter to hierarchically porous carbons as high-rate-performance supercapacitors, Chem. Mater. 28 (2016) 445–458.

[142] S. Kondrat, C. Pérez, V. Presser, Y. Gogotsi, A. Kornyshev, Effect of pore size and its dispersity on the energy storage in nanoporous supercapacitors, Energ. Environ. Sci. 5 (2012) 6474–6479.

[143] X. Wu, L. Jiang, F. Cao, Y. Guo, L. Wan, LiFePO$_4$ nanoparticles embedded in a nanoporous carbon matrix: superior cathode material for electrochemical energy-storage devices, Adv. Mater. 21 (2009) 2710–2714.

[144] Y. Huang, F. Zheng, X. Zhang, Q. Li, H. Wang, Effect of carbon coating on cycle performance of LiFePO$_4$/C composite cathodes using Tween80 as carbon source, Electrochim. Acta 130 (2014) 740–747.

[145] J. Hagberg, H. Maples, K. Alvim, J. Xu, W. Johannisson, A. Bismarck, D. Zenkert, G. Lindbergh, Lithium iron phosphate coated carbon fiber electrodes for structural lithium ion batteries, Compos. Sci. Technol. 162 (2018) 235–243.

[146] Wang Guoxiu, Liu Hao, Liu Jian, Qiao Shizhang, Max Gaoqing, Mesoporous LiFePO$_4$/C nanocomposite cathode materials for high power lithium ion batteries with superior performance, Adv. Mater. 22 (2010) 4944–4948.

[147] F. Yu, L. Zhang, L. Lai, M. Zhu, Y. Guo, L. Xia, P. Qi, G. Wang, B. Dai, High electrochemical performance of LiFePO$_4$ cathode material via in-situ microwave exfoliated graphene oxide, Electrochim. Acta 151 (2015) 240–248.

[148] B. Kang, G. Ceder, Battery materials for ultrafast charging and discharging, Nature 458 (2009) 190–193.

[149] S. Kandhasamy, K. Nallathamby, M. Minakshi, Role of structural defects in olivine cathodes, Prog. Solid State Chem. 40 (2012) 1–5.

[150] N. Bramnik, K. Bramnik, T. Buhrmester, C. Baehtz, H. Ehrenberg, H. Fuess, Electrochemical and structural study of LiCoPO$_4$-based electrodes, J. Solid State Electrochem. 8 (2004) 558–564.

[151] S., K. Xiong, R. Longo, K. Cho, Interface phenomena between Li anode and lithium phosphate electrolyte for Li-ion battery, J. Power Sources 244 (2013) 136–142.

[152] Y. Shi, X. Zhou, J. Zhang, A. Bruck, A. Bond, A. Marschilok, K. Takeuchi, E. Takeuchi, G. Yu, Nanostructured conductive polymer gels as a general framework material to improve electrochemical performance of cathode materials in Li-ion batteries, Nano Lett. 17 (2017) 1906–1914.

[153] N. Vicente, M. Haro, D. Cíntora-Juárez, C. Pérez-Vicente, J. Tirado, S. Ahmad, G. Garcia-Belmonte, LiFePO$_4$ particle conductive composite strategies for improving cathode rate capability, Electrochim. Acta 163 (2015) 323–329.

[154] R. Kohlmeyer, A. Blake, J. Hardin, E. Carmona, M. Durstock, Composite batteries: a simple yet universal approach to 3D printable lithium-ion battery electrodes, J. Mater. Chem. A 4 (2016) 16856.

[155] L. Zhou, W. Ning, C. Wu, D. Zhang, W. Wei, J. Ma, C. Li, L. Chen, 3D-printed microelectrodes with a developed conductive network and hierarchical pores toward high areal capacity for microbatteries, Adv. Mater. Technol. 4 (2019) 1800402.

[156] S. Ha, K. Shin, H. Park, Y. Lee, Flexible lithium-ion batteries with high areal capacity enabled by smart conductive textiles, Small 14 (2018) 1703418.

[157] J. Kim, J. Scheers, H. Ryu, J. Ahn, T. Nam, K. Kim, H. Ahn, G. Cho, P. Jacobsson, A layer-built rechargeable lithium ribbon-type battery for high energy density textile battery applications, J. Mater. Chem. A 2 (2014) 1774–1780.

[158] A. Paolella, C. Faure, G. Bertoni, S. Marras, A. Guerfi, A. Darwiche, P. Hovington, B. Commarieu, Z. Wang, M. Prato, M. Colombo, S. Monaco, W. Zhu, Z. Feng, A. Vijh, C. George, G. Demopoulos, M. Armand, K. Zaghib, Light-assisted delithiation of lithium iron phosphate nanocrystals towards photo-rechargeable lithium ion batteries, Nat. Commun. 8 (2017) 14643.

[159] S. Zheng, Z. Wu, F. Zhou, X. Wang, J. Ma, C. Liu, Y. He, X. Bao, All-solid-state planar integrated lithium ion micro-batteries with extraordinary flexibility and high-temperature performance, Nano Energy 51 (2018) 613–620.

[160] J. Hassoun, M. Pfanzelt, P. Kubiak, M. Wohlfahrt-Mehrens, B. Scrosati, An advanced configuration TiO$_2$/LiFePO$_4$ polymer lithium ion battery, J. Power Sources 217 (2012) 459–463.

[161] M. Ganter, B. Landi, C. Babbitt, A. Anctil, G. Gaustad, Cathode refunctionalization as a lithium ion battery recycling alternative, J. Power Sources 256 (2014) 274–280.

[162] J. Li, Y. Cheng, M. Jia, Y. Tang, Y. Lin, Z. Zhang, Y. Liu, An electrochemical–thermal model based on dynamic responses forlithium iron phosphate battery, J. Power Sources 255 (2014) 130–143.

[163] J. Nanda, S. Martha, W. Porter, H. Wang, N. Dudney, M. Radin, D. Siegel, Thermophysical properties of LiFePO$_4$ cathodes with carbonized pitch coatings and organic binders: experiments and first-principles modeling, J. Power Sources 251 (2014) 8–13.

[164] H. Li, L. Peng, D. Wu, J. Wu, Y. Zhu, X. Hu, Ultrahigh-capacity and fire-resistant LiFePO$_4$-based composite cathodes for advanced lithium-ion batteries, Adv. Energy Mater. 9 (2019) 1802930.

[165] Y. Zhou, D. Yang, Y. Zeng, Y. Zhou, W. Ng, Q. Yan, E. Fong, Recycling bacteria for the synthesis of LiMPO$_4$ (M = Fe, Mn) nanostructures for high-power lithium batteries, Small 10 (2015) 3997–4002.

[166] J. Ni, W. Liu, J. Liu, L. Gao, J. Chen, Investigation on a 3.2V LiCoPO$_4$/Li$_4$Ti$_5$O$_{12}$ full battery, Electrochem. Commun. 35 (2013) 1–4.

[167] C. Du, Z. Tang, J. Wu, H. Tang, X. Zhang, A three volt lithium ion battery with LiCoPO$_4$ and zero-strain Li$_4$Ti$_5$O$_{12}$ as insertion material, Electrochim. Acta 125 (2014) 58–64.

[168] J. Ni, H. Wang, L. Gao, L. Lu, A high-performance LiCoPO$_4$/C core/shell composite for Li-ion batteries, Electrochim. Acta 70 (2012) 349–354.

[169] A. Örnek, An impressive approach to solving the ongoing stability problems of LiCoPO$_4$ cathode: nickel oxide surface modification with excellent core–shell principle, J. Power Sources 356 (2017) 1–11.

[170] A. Örnek, M. Can, A. Yeşildağ, Improving the cycle stability of LiCoPO$_4$ nanocomposites as 4.8V cathode: stepwise or synchronous surface coating and Mn substitution, Mater. Charact. 116 (2016) 76–83.

[171] I. Jang, H. Lim, S. Lee, K. Karthikeyan, V. Aravindan, K. Kang, W. Yoon, W. Cho, Y. Lee, Preparation of LiCoPO$_4$ and LiFePO$_4$ coated LiCoPO$_4$ materials with improved battery performance, J. Alloys Compd. 497 (2010) 321–324.

[172] Multi-wall carbon nanotube-embedded lithium cobalt phosphate composites with reduced resistance for high-voltage lithium-ion batteries, Electron. Mater. Lett. 12 (2016) 147–155.

[173] Q. Truong, M. Devaraju, Y. Ganbe, T. Tomai, I. Honma, Controlling the shape of LiCoPO$_4$ nanocrystals by supercritical fluid process for enhanced energy storage properties, Sci. Rep. 4 (2014) 3975.

[174] M. Devaraju, Q. Truong, H. Hyodo, Y. Sasaki, I. Honma, nanomaterials, Sci. Rep. 5 (2015) 11041.

[175] L. Dimesso, D. Becker, C. Spanheimer, W. Jaegermann, Investigation of graphitic carbon foams/LiNiPO$_4$ composites, J. Solid State Electrochem. 16 (2012) 3791–3798.

[176] A. Örnek, M. Kazancioglu, A novel and effective strategy for producing core-shell LiNiPO$_4$/C cathode material for excellent electrochemical stability using a long-time and low-level microwave approach, Scripta Mater. 122 (2016) 45–49.

[177] V. Aravindan, J. Gnanaraj, Y. Lee, S. Madhavi, LiMnPO$_4$ – a next generation cathode material for lithium-ion batteries, J. Mater. Chem. A 1 (2013) 3518–3539.

[178] Z. Wu, Y. Long, X. Lv, J. Su, Y. Wen, Microwave heating synthesis of spindle-like LiMnPO$_4$/C in a deep eutectic solvent, Ceram. Int. 43 (2017) 6089–6095.

[179] H. Yang, J. Liu, X. Wang, C. Zhao, L. Wang, Y. Wang, Y. Xia, T. Liu, Positive surface pseudocapacitive behavior-induced fast and large Li-ion storage in mesoporous LiMnPO$_4$@C nanofibers, ChemSusChem 12 (2019) 3817–3826.

[180] N. Membreño, P. Xiao, K. Park, J. Goodenough, G. Henkelman, K. Stevenson, Situ Raman study of phase stability of α-Li$_3$V$_2$(PO$_4$)$_3$ upon thermal and laser heating, J. Phys. Chem. C 117 (2013) 11994–12002.

[181] X. Zhang, R. Kühnel, H. Hu, D. Eder, A. Balducci, Going nano with protic ionic liquids—the synthesis of carbon coated Li$_3$V$_2$(PO$_4$)$_3$ nanoparticles encapsulated in a carbon matrix for high power lithium-ion batteries, Nano Energy 12 (2015) 207–214.

[182] C. Liu, R. Massé, X. Nan, G. Cao, A promising cathode for Li-ion batteries: Li$_3$V$_2$(PO$_4$)$_3$, Energy Storage Mater. 4 (2016) 15–58.

[183] L. Mai, S. Li, Y. Dong, Y. Zhao, Y. Luo, H. Xu, Long-life and high-rate Li$_3$V$_2$(PO$_4$)$_3$/C nanosphere cathode materials with three-dimensional continuous electron pathways, Nanoscale 5 (2013) 4864–4869.

[184] X. Zhu, Z. Li, X. Jia, W. Dong, G. Wang, F. Wei, Y. Lu, Approaching theoretical capacities in thick lithium vanadium phosphate electrodes at high charge/discharge rates, ACS Sustain. Chem. Eng. 6 (2018) 15608–15617.

[185] C. Wei, W. He, X. Zhang, F. Xu, Q. Liu, C. Sun, X. Song, Effects of morphology on the electrochemical performances of Li$_3$V$_2$(PO$_4$)$_3$ cathode material for lithium ion batteries, RSC Adv. 5 (2015) 54225–54245.

[186] Z. Cao, T. Fang, X. Hou, J. Niu, In-situ preparation of nitrogen-doped carbon-modified lithium vanadium phosphate fibers with mesoporous nanostructure for lithium energy storage, Ceram. Int. 45 (2019) 14474–14478.

[187] D. Li, M. Tian, R. Xie, Q. Li, X. Fan, L. Gou, P. Zhao, S. Ma, Y. Shi, H. Yong, Three-dimensionally ordered macroporous Li$_3$V$_2$(PO$_4$)$_3$/C nanocomposite cathode material for high-capacity and high-rate Li-ion batteries, Nanoscale 6 (2014) 3302–3308.

[188] J. Wu, M. Xu, C. Tang, G. Li, H. He, C. Li, F-Doping effects on carbon-coated Li$_3$V$_2$(PO$_4$)$_3$ as a cathode for high performance lithium rechargeable batteries: combined experimental and DFT studies, Phys. Chem. Chem. Phys. 20 (2018) 15192–15202.

[189] Z. Zuo, J. Deng, J. Pan, W. Luo, Q. Yao, Z. Wang, H. Zhou, H. Liu, High energy density of Li$_{3-x}$Na$_x$V$_2$(PO$_4$)$_3$/C cathode material with high rate cycling performance for lithium-ion batteries, J. Power Sources 357 (2017) 117–125.

[190] A new carbon additive compounded Li$_3$V$_{1.97}$Zn$_{0.05}$(PO$_4$)$_3$/C cathode for plug-in hybrid electric vehicles, Electrochim. Acta 170 (2015) 269–275.

[191] H. Sun, L. Zhang, X. Yang, Y. Huang, G. Liang, Effect of Fe-doping followed by C+SiO$_2$ hybrid layer coating on Li$_3$V$_2$(PO$_4$)$_3$ cathode material for lithium-ion batteries, Ceram. Int. 42 (2016) 16557–16562.

[192] V. Aravindan, W. Ling, S. Hartung, N. Bucher, S. Madhavi, Carbon-coated LiTi$_2$(PO$_4$)$_3$: an ideal insertion host for lithium-ion and sodium-ion batteries, Chem. Asian J. 9 (2014) 878–882.

[193] J. Zheng, Y. Han, D. Sun, B. Zhang, E. Cairns, In situ-formed LiVOPO$_4$@V$_2$O$_5$ core-shell nanospheres as a cathode material for lithium-ion cells, Energy Storage Mater 7 (2017) 48–55.

[194] Q. Zou, G. Zhu, Y. Xia, Preparation of carbon-coated LiFe$_{0.2}$Mn$_{0.8}$PO$_4$ cathode material and its application in a novel battery with Li$_4$Ti$_5$O$_{12}$ anode, J. Power Sources 206 (2012) 222–229.

[195] M. Srout, K. Lasri, M. Dahbi, A. Kara, L. Tetard, I. Saadoune, Understanding of the Li-insertion process in a phosphate based electrode material for lithium ion batteries, J. Power Sources 435 (2019) 226803.

[196] M. Kim, H. Kim, S. Lee, D. Kim, D. Ruan, K. Chung, S. Lee, K. Roh, K. Kim, Correction: corrigendum: synthesis of reduced graphene oxide-modified LiMn$_{0.75}$Fe$_{0.25}$PO$_4$ microspheres by salt-assisted spray drying for high-performance lithium-ion batteries, Sci. Rep. 6 (2016) 29147.

[197] J. Han, I. Park, J. Cha, S. Park, S. Park, S. Myeong, W. Cho, S. Kim, S. Hong, J. Cho, N. Choi, Interfacial architectures derived by lithium difluoro(bisoxalato) Phosphate for lithium-rich cathodes with superior cycling stability and rate capability, ChemElectroChem 4 (2017) 56–65.

[198] C. Vidal-Abarca, M. Aragon, P. Lavela, J. Tirado, Influence of composition modification on Ca$_{0.5x}$Mg$_x$Ti$_2$(PO$_4$)$_3$ (0.0≤x≤0.5) nanoparticles as electrodes for lithium batteries, Mater. Res. Bull. 49 (2014) 566–571.

[199] A. Lipson, S. Kim, B. Pan, C. Liao, T. Fister, B. Ingram, Calcium intercalation into layered fluorinated sodium iron phosphate, J. Power Sources 369 (2017) 133–137.

[200] Z. Huang, T. Masese, Y. Orikasa, T. Mori, K. Yamamoto, Vanadium phosphate as a promising high-voltage magnesium ion (de)-intercalation cathode host, RSC Adv. 5 (2015) 8598–8603.

[201] Y. Liu, Y. Xu, X. Han, C. Pellegrinelli, Y. Zhu, H. Zhu, J. Wan, A. Chung, O. Vaaland, C. Wang, L. Hu, Porous amorphous FePO$_4$ nanoparticles connected by single-wall carbon nanotubes for sodium ion battery cathodes, Nano Lett. 12 (2012) 5664–5668.

[202] X. Wu, Y. Cao, X. Ai, J. Qian, H. Yang, A low-cost and environmentally benign aqueous rechargeable sodium-ion battery based on NaTi$_2$(PO$_4$)$_3$–Na$_2$NiFe(CN)$_6$ intercalation chemistry, Electrochem. Commun. 31 (2013) 145–148.

[203] Q. Hu, J. Liao, R. Xu, X. He, J. Wang, X. Ding, C. Chen, 3D porous NaTi$_2$(PO$_4$)$_3$ with long life, superior rate, and low-temperature properties, Energy Technol. 7 (2019) 1900386.

[204] C. Manohar, T. Mendes, M. Kar, D. wang, C. Xiao, M. Forsyth, S. Mitra, D. MacFarlane, Ionic liquid electrolytes supporting high energy density in sodium-ion batteries based on sodium vanadium phosphate composites, Chem. Commun. 54 (2018) 3500–3503.

[205] R. Panin, O. Drozhzhin, S. Fedotov, N. Khasanova, E. Antipov, NASICON-type NaMo$_2$(PO$_4$)$_3$: electrochemical activity of the Mo^{+4} polyanion compound in Na–cell, Electrochim. Acta 289 (2018) 168–174.

[206] X. Zhu, T. Mochiku, H. Fujii, K. Tang, Y. Hu, Z. Huang, B. Luo, K. Ozawa, L. Wang, A new sodium iron phosphate as a stable high-rate cathode material for sodium ion batteries, Nano Res. 11 (2018) 6197–6205.

[207] J. Ko, Vicky, V. Doan-Nguyen, H. Kim, X. Petrissans, R. DeBlock, C. Choi, J. Long, B. Dunn, High-rate capability of Na$_2$FePO$_4$F nanoparticles by enhancing surface carbon functionality for Na-ion batteries, J. Mater. Chem. A 5 (2017) 18707–18715.

[208] J. Baboo, J. Song, S. Kim, J. Jo, S. Baek, V. Mathew, D. Pham, M. Alfaruqi, Z. Xiu, Y. Sun, J. Kim, Monoclinic-orthorhombic Na$_{1.1}$Li$_{2.0}$V$_2$(PO$_4$)$_3$/C composite cathode for Na$^+$/Li$^+$ hybrid-ion batteries, Chem. Mater. 29 (2017) 6642–6652.

[209] C. Zhu, K. Song, P. van Aken, J. Maier, Y. Yu, Carbon-coated Na$_3$V$_2$(PO$_4$)$_3$ embedded in porous carbon matrix: an ultrafast na-storage cathode with the potential of outperforming Li cathodes, Nano Lett. 14 (2014) 2175–2180.

[210] Y. Chen, Y. Xu, X. Sun, B. Zhang, S. He, L. Li, C. Wang, Preventing structural degradation from Na$_3$V$_2$(PO$_4$)$_3$ to V$_2$(PO$_4$)$_3$: F-doped Na$_3$V$_2$(PO$_4$)$_3$/C cathode composite with stable lifetime for sodium ion batteries, J. Power Sources 378 (2018) 423–432.

[211] Q. Zhu, M. Wang, B. Nan, H. Shi, X. Zhang, Y. Deng, L. Wang, Q. Chen, Z. Lu, Core/shell nanostructured Na$_3$V$_2$(PO$_4$)$_3$/C/TiO$_2$ composite nanofibers as a stable anode for sodium-ion batteries, J. Power Sources 362 (2017) 147–159.

[212] L. Ke, J. Dong, B. Lin, T. Yu, H. Wang, S. Zhang, C. Deng, A NaV$_3$(PO$_4$)$_3$@C hierarchical nanofiber in high alignment: exploring a novel high-performance anode for aqueous rechargeable sodium batteries, Nanoscale 9 (2017) 4183–4190.

[213] Y. Chen, Y. Xu, X. Sun, C. Wang, Effect of Al substitution on the enhanced electrochemical performance and strong structure stability of Na$_3$V$_2$(PO$_4$)(3)/C composite cathode for sodium-ion batteries, J. Power Sources 375 (2018) 82–92.

[214] Y. Chen, Y. Xu, X. Sun, B. Zhang, S. He, C. Wang, F-doping and V-defect synergetic effects on Na$_3$V$_2$(PO$_4$)$_3$/C composite: a promising cathode with high ionic conductivity for sodium ion batteries, J. Power Sources 397 (2018) 307–317.

[215] M. Aragón, C. Vidal-Abarca, P. Lavela, J. Tirado, High reversible sodium insertion into iron substituted Na$_{1+x}$Ti$_{2-x}$Fe$_x$(PO$_4$)$_3$, J. Power Sources 252 (2014) 208–213.

[216] Y. Liu, N. Zhang, F. Wang, X. Liu, L. Jiao, L. Fan, Approaching the downsizing limit of maricite NaFePO$_4$ toward high-performance cathode for sodium-ion batteries, Adv. Funct. Mater. 28 (2018) 1801917.

[217] M. Chen, W. Hua, J. Xiao, D. Cortie, W. Chen, E. Wang, Z. Hu, Q. Gu, X. Wang, S. Indris, S. Chou, S. Dou, NASICON-type air-stable and all-climate cathode for sodium-ion batteries with low cost and high-power density, Nat. Commun. 10 (2019) 1480.

[218] T. Yuan, Y. Wang, J. Zhang, X. Pu, X. Ai, Z. Chen, H. Yang, Y. Cao, 3D graphene decorated Na$_4$Fe$_3$(PO$_4$)$_2$(P$_2$O$_7$) microspheres as low-cost and high-performance cathode materials for sodium-ion batteries, Nano Energy 56 (2019) 160–168.

[219] H. Kim, G. Yoon, I. Park, J. Hong, K. Park, J. Kim, K. Lee, N. Sung, S. Lee, K. Kang, Highly stable iron- and manganese-based cathodes for long-lasting sodium rechargeable batteries, Chem. Mater. 28 (2016) 7241–7249.

[220] K. Wedepohl, The composition of the continental crust, Geochim. Cosmochim. Acta 59 (1995) 1217–1232.

[221] X. Ji, J. Chen, F. Wang, W. Sun, Y. Ruan, L. Miao, J. Jiang, C. Wang, Water-activated VOPO$_4$ for magnesium ion batteries, Nano Lett. 18 (2018) 6441–6448.

[222] N. Bramnik, K. Bramnik, K. Nikolowski, M. Hinterstein, C. Baehtz, H. Ehrenberg, Synchrotron diffraction study of lithium extraction from LiMn$_{0.6}$Fe$_{0.4}$PO$_4$, Electrochem. Solid-State Lett. 8 (2005) A379.

[223] N. Bramnik, K. Nikolowski, C. Baehtz, K. Bramnik, H. Ehrenberg, Phase transitions occurring upon lithium insertion−extraction of LiCoPO$_4$, Chem. Mater. 19 (2007) 908–915.

[224] M. Morcrette, J. Leriche, S. Patoux, C. Wurm, C. Masquelier, In situ X-ray diffraction during lithium extraction from rhombohedral and monoclinic Li$_3$V$_2$(PO$_4$)$_3$, Electrochem. Solid-State Lett. 6 (2003) A80.

[225] S. Patoux, C. Wurm, M. Morcrette, G. Rousse, C. Masquelier, A comparative structural and electrochemical study of monoclinic Li$_3$Fe$_2$(PO$_4$)$_3$ and Li$_3$V$_2$(PO$_4$)$_3$, J. Power Sources 119-121 (2003) 278–284.

[226] S. Patoux, G. Rousse, J. Leriche, C. Masquelier, Structural and electrochemical studies of rhombohedral Na$_2$TiM(PO$_4$)$_3$ and Li$_{1.6}$Na$_{0.4}$TiM(PO$_4$)$_3$ (M = Fe, Cr) phosphates, Chem. Mater. 15 (2003) 2084–2093.

[227] C. Delacourt, P. Poizot, D. Bonnin, C. Masquelier, Lithium-insertion mechanism in crystalline and amorphous FePO$_4$.nH$_2$O, J. Electrochem. Soc. 156 (2009) A595.

[228] M. Tang, W. Carter, J. Belak, Y. Chiang, Modeling the competing phase transition pathways in nanoscale olivine electrodes, Electrochim. Acta 56 (2011) 969–976.

[229] C. Tealdi, J. Heath, M. Islam, Feeling the strain: enhancing ionic transport in olivine phosphate cathodes for Li- and Na-ion batteries through strain effects, J. Mater. Chem. A 4 (2016) 6998–7004.

[230] L. Qiu, Z. Shao, D. Wang, F. Wang, W. Wang, J. Wang, Novel polymer Li-ion binder carboxymethyl cellulose derivative enhanced electrochemical performance for Li-ion batteries, Carbohydr. Polym. 112 (2014) 532–538.

[231] G. Kim, S. Jeong, M. Joost, E. Rocca, M. Winter, S. Passerini, A. Balducci, Use of natural binders and ionic liquid electrolytes for greener and safer lithium-ion batteries, J. Power Sources 196 (2011) 2187–2194.

[232] J. Huang, J. Wang, H. Zhong, L. Zhang, N-cyanoethyl polyethylenimine as a water-soluble binder for LiFePO$_4$ cathode in lithium-ion batteries, J. Mater. Sci. 53 (2018) 9690–9700.

[233] M. Ling, J. Qiu, S. Li, C. Yan, M. Kiefel, G. Liu, S. Zhang, Multifunctional SA-P-ProDOT binder for lithium ion batteries, Nano Lett. 15 (2015) 4440–4447.

[234] L. Zhao, Z. Sun, H. Zhang, Y. Li, Y. Mo, F. Yu, Y. Chen, An environment-friendly crosslinked binder endowing LiFePO$_4$ electrode with structural integrity and long cycle life performance, RSC Adv. 10 (2020) 29362–29372.

[235] M. Tian, Y. Qi, E. Oh, Application of a polyacrylate latex to a lithium iron phosphate cathode as a binder material, Energies 14 (2021).

[236] R. Apraksin, S. Eliseeva, M. Kamenskii, E. Tolstopyatova, G. Lang, V. Kondrat'ev, Impedance of LiFe$_{0.4}$Mn$_{0.6}$PO$_4$ electrodes with combined conducting polymer binder of PEDOT:PSS and carboxymethyl cellulose, Russ. J. Electrochem. 55 (2019) 1047–1057.

[237] S. Eliseeva, R. Apraksin, E. Tolstopjatova, V. Kondratiev, Electrochemical impedance spectroscopy characterization of LiFePO$_4$ cathode material with carboxymethylcellulose and poly-3,4-ethylendioxythiophene/polystyrene sulfonate, Electrochim. Acta 227 (2017) 357–366.

[238] H. Raj, A. Sil, Energy and power densities of novel composite electrode driven by synergy of poly(3,4-ethylene dioxythiophene):poly(styrene sulfonate) and single walled carbon nanotubes for lithium-ion battery, J. Power Sources 458 (2020) 228052.

[239] P. Ranque, C. George, R. Dubey, R. van der Jagt, D. Flahaut, R. Dedryvère, M. Fehse, P. Kassanos, W. Jager, E. Sudhölter, E. Kelder, Scalable route to electroactive and light active perylene diimide dye polymer binder for lithium-ion batteries, ACS Appl. Energy Mater. 3 (2020) 2271–2277.

[240] M. Manickam, M. Takata, Effect of cathode binder on capacity retention and cycle life in transition metal phosphate of a rechargeable lithium battery, Electrochim. Acta 48 (2003) 957–963.

[241] M. Yao, H. Senoh, T. Sakai, T. Kiyobayashi, Redox active poly(N-vinylcarbazole) for use in rechargeable lithium batteries, J. Power Sources 202 (2012) 364–368.

[242] P. Prosini, M. Carewska, C. Cento, A. Masci, Poly vinyl acetate used as a binder for the fabrication of a LiFePO$_4$-based composite cathode for lithium-ion batteries, Electrochim. Acta 150 (2014) 129–135.

[243] S. Jeong, N. Böckenfeld, A. Balducci, M. Winter, S. Passerini, Natural cellulose as binder for lithium battery electrodes, J. Power Sources 199 (2012) 331–335.

[244] J. Daigle, F. Barray, C. Gagnon, D. Clément, P. Hovington, H. Demers, A. Guerfi, K. Zaghib, Amphiphilic latex as a water-based binder for LiFePO$_4$ cathode, J. Power Sources 415 (2019) 172–178.